Author:
Best, Jacob T

Title:
A numerical study of a nacre-inspired ballistic armour system

A NUMERICAL STUDY OF A NACRE-INSPIRED BALLISTIC ARMOUR SYSTEM

Jacob Thomas Best

Department of Aerospace Engineering
UNIVERSITY OF BRISTOL

A dissertation submitted to the University of Bristol in accordance with the requirements of the degree of DOCTOR OF PHILOSOPHY in the Faculty of Engineering

February 2019

Word Count: 42,000

Abstract

There is growing interest in the application of biological systems to solve engineering problems. Of particular interest in this research is the biological material nacre, found in the inner layer of *Haliotis rufescens* (red abalone). This material exhibits a fracture toughness three orders of magnitude greater than its constituent components. Designing a tiled armour system predicated on the functional architecture of nacre could enhance multi-hit performance without compromising ballistic performance or momentum dissipation of the armour against a single impact. The specific features of interest are topological interlocking between tiled platelets and the inclusion of a ductile interlayer cohesive matrix. These features may allow for ceramics such as alumina (Al_2O_3) to retain the high hardness and yield stress that make them suitable as ballistic protection while adding the potential for multi-hit capability and increased durability. This research focuses on the development of a tiled alumina ceramic armour system to protect against a 7.62 mm AP M2 round impacting at 875 m s^{-1} with the potential for multi-hit capability.

Using the explicit dynamic solver, LS-DYNA, the geometric design space of a tiled ceramic armour system is explored to determine optimal thickness, edge length and spatial arrangement of tiled systems as well as investigating the change in damage mechanisms that occur when transitioning from a monolithic design. This showed that, for a single shot, a monolithic plate is the optimal armour system for ballistic performance and the introduction of any through-thickness interfaces greatly inhibits ballistic properties. Therefore, any tiled armour design must focus on mitigating this reduction in performance while optimising secondary performance criteria such as multi-hit capability.

A novel tile geometry is proposed featuring nacre-inspired topologically interlocking surfaces. A parametric study is conducted for each characteristic surface profile for a range of tile sizes in order to optimise ballistic performance against a single impact and to minimise the armour sensitivity to impact location. Further, a cohesive matrix is introduced in the inter-layers of the tiled system to mirror the ductile organic polymers of nacre. Finally, the proposed armour designs are tested against multiple impacts.

Dedication and Acknowledgements

I would first like to express my gratitude to my supervisor, Professor Stephen Hallett, for his insight, guidance and patience. There have been many times when he has gone beyond the call of duty on my behalf. Through times when it seemed that this thesis might never be finished, he continued to support and motivate me. Another honourable mention goes to Dr Luiz Kawashita.

Secondly, I would like to strongly thank Dr David Hallam for his work as my technical supervisor overseeing the project from DSTL. Despite moving away from the project officially, he continued to freely offer his time and considerable knowledge of ceramics. I hope life treats him well because he truly deserves it.

Thirdly, I would like to thank my peers within ACCIS (now the Bristol Composites Institute) for welcoming me so warmly from day one. In particular, I would like to thank the unofficial social secretary of the department, Dr Daniel Everitt, as well as Dr Callum Heath for their friendship and support throughout my doctorate.

I would like to extend special thanks to Dr Robin Neville for his boundless scientific curiosity, his uniquely creative perspectives and his enthusiasm for life. He has an uncanny ability to have developed the skills I desperately need to learn just moments before I happen to ask. Thank you for sharing so freely, you have saved me hundreds of hours over the last few years and wasted at least half as many over coffee.

Finally, I would like to acknowledge and thank my family, especially my mother for her patience and support, and my father for his wisdom and counsel. Listing all of the ways in which I am grateful to them and to the rest of my family would take too long here and repaying them may take a lifetime.

This thesis is dedicated to my grandmother, "Nans", who has been my most ardent cheerleader throughout and whom I hope I have made proud.

Author's Declaration

I declare that the work in this dissertation was carried out in accordance with the requirements of the University's Regulations and Code of Practice for Research Degree Programmes and that it has not been submitted for any other academic award. Except where indicated by specific reference in the text, the work is the candidate's own work. Work done in collaboration with, or with the assistance of others, is indicated as such. Any views expressed in the dissertation are those of the author.

SIGNED:……DATE:…… ……

Contents

LIST OF TABLES

LIST OF FIGURES

CHAPTER 1 - INTRODUCTION

1.1 CONTEXT OF RESEARCH

Ceramic armours provide excellent ballistic protection at relatively low density, making ceramics ideal for use as personal body armour. Their characteristically high hardness and high compressive yield stress contribute to this ballistic mass efficiency [1]. However, the attendant compromise is a low fracture toughness leading to significant crack propagation after impact and a large damage zone. This significantly inhibits the multi-hit capability of ceramic armours and leaves the wearer vulnerable to subsequent ballistic threats. Segmenting an armour into tiles may limit this damage zone and therefore improve multi-hit performance. However, this increases the concentration of the momentum from the projectile and increases deflection in the back face of the armour under impact [2]. This compromise, while acceptable and widely used in vehicle armour, is not acceptable for personal armour due to the risk of injury from blunt force trauma [3].

Bio-mimetics is a field of research that looks to nature and biological systems for inspiration to overcome engineering problems such as that described above. With a comparatively limited array of organic materials, biology has created many materials with incredible functional properties. This is achieved through a hierarchical architecture of macro-, meso- and even nanoscale features [4–6]. This has led to researchers looking to nature with the intention of transplanting the functional structures found there into systems constructed with the stronger, tougher and harder materials available to engineers, creating vastly improved materials in the process.

One biological material of particular interest in the design of ceramic armours is nacre, the inner-layer of the shell of the red abalone mollusc. Through a combination of a hard ceramic platelet structure and a more ductile organic polymer interlayer matrix, this material achieves a fracture toughness several orders of magnitude greater than that of the ceramic component in isolation [7,8]. Preliminary work with metals, primarily aluminium, has shown promise in this approach inhibiting damage zone growth while interlocking between tiles allows for greater momentum dissipation upon impact [9]. It has not yet been shown if the features of nacre can be adapted to a high-performance ceramic armour.

1.2 AIMS AND OBJECTIVES

This research aims to explore whether the meso-scale structures of nacre that provide significantly improved fracture toughness at the low strain rates experienced under impact by sea debris can be transposed to a macro-scale armour structure in a high strain-rate impact environment. The work

is focussed on understanding the influences of each component of a tiled armour design to develop a greater understanding of the design space for a nacre-inspired armour. This should direct the development of an optimal tiled armour design with the goal of producing a ceramic armour capable of maintaining ballistic performance over multiple threats, with single shot performance comparable to that of a monolithic material armour.

1.3 THESIS BREAKDOWN

After this introductory chapter, a review of the current literature provides a breakdown of current research in ceramic armour, damage mechanisms and bio-mimetic armour design (Chapter 2). The following chapter describes the verification and validation process in the development of the finite element (FE) model of a high velocity impact against a monolithic ceramic armour (Chapter 3). This model is calibrated against experimental data to ensure that the proceeding computational work is grounded in reality. There follows a comprehensive study, using FE analysis (FEA) of various design aspects relevant to a tiled armour including the effects on ballistic performance of tile size, thickness, impact location, number of layers and mosaic structure (Chapter 4).

A novel geometric tile shape is then introduced and optimised combining aspects of the interlocking substructure of nacre with the design elements explored in the preceding chapter (Chapter 5). The design space was then expanded to include a cohesive interlayer matrix between the ceramic tiles to increase tensile strength as well as the frictional and interlocking behaviour that provide nacre with its improved functional properties (Chapter 6). Finally, optimised tiled armour designs are tested against multiple impacts and compared to the performance of a monolithic ceramic baseline armour (Chapter 7). Conclusions from this work are then presented as well as suggested areas of future work (Chapter 8).

CHAPTER 2 – LITERATURE REVIEW

2.1 INTRODUCTION

The development of armour for use in combat and warfare dates back at least as far as the Assyrians of 1000BC in their use of bronze, iron and wood to protect against the spears, swords and arrows of their enemies although likely goes as far back as the human invention of clothes [10]. The threat has changed considerably since then, but the underlying general principles remain unchanged. These are that a useful body armour should minimise the physiological stress of any impact to the wearer, minimally inhibit mobility and be sufficiently damage resistant to everyday use. The primary function of armour, i.e. that of preventing injury to the user, is limited by these considerations. A heavier armour may well give greater protection but inhibits mobility, perhaps to such an extent that operational efficiency is reduced, or the wearer is more likely to be hit and subsequently injured. The ability to move freely and to efficiently make use of weapons plays as important a role in protecting a soldier as any additional physical protection [11]. For this reason, armours must be designed with operational efficiency as a paramount concern and not simply resistance to ballistic penetration.

In recent years there has been increasing interest in bio-mimicry as a potential source of innovation [12–14]. Bio-mimicry is the adaptation of designs and mechanisms found in nature and their application to engineering problems. Evolutionary development has imbued many plants and animals with highly specialised mechanisms and designs to overcome the limitations of the materials from which they are grown, some of which display complexity far beyond current engineering solutions. Potential sources of biological inspiration include the keratinised structure of horse hooves and the complex lattice structure in silica sea sponges [15,16]. For armoured designs there is significant promise in, for example, the nacreous inner-layer of red abalone (*Haliotis rufescens*) that is many times tougher than the base material, aragonite, of which it is comprised [17].

2.2 OVERVIEW: CERAMICS AND ARMOUR

The ultimate purpose of armour can be characterised as the absorption and dissipation of energy of an incoming ballistic threat so as to minimise or prevent damage to a specific target. In military applications the targets are building, vehicles and personnel. As buildings are not required to move, defensive structures are not as subject to weight limitations. Hence it was not in the protecting of buildings that the science of armour was developed as the structural components often provided significant protection and, in any case, thicker concrete walls could be added at minimal relative

cost compared to the cost of mobile armours. For vehicles and personnel, weight is a primary consideration as high weight increases the costs of transportation and can inhibit mobility in the field. Therefore, although cost remains an inhibiting factor, it is offset by the need to innovate systems that allow the military units utilising the armour to retain high levels of operational functionality.

Ceramic armour was first developed in the early 1960's as a response to evolving threats on the battlefield. These ceramic armours were designed for combat vehicles such as the UK's Challenger tanks and consisted of large monolithic slabs that could resist both high kinetic-energy threats and explosive anti-tank (HEAT) shells [18]. These early vehicle armour designs had areal-densities far higher than that appropriate for personal body armour but set the stage for a renewed interest in ceramic research and the development of ceramic-composite designs with further enhanced ballistic performance.

The first patent for ceramic body armour can be traced back to the Vietnam War era when protection was required for night watchmen standing guard exposed to the danger of .30 calibre bullets from snipers [19]. This investigation started with "dinner plate" sized alumina ceramics that, whilst capable of stopping a .30 calibre threat, would completely shatter upon impact. The shattering of the ceramic (sometimes described as the disturber layer) introduced the requirement for a backing material to collect these fragments and prevent injury to the wearer. This layer is often referred to as the absorber layer and is usually a more ductile material, such as Kevlar or rubber, than the ceramic layer in front, that is referred to as the disturber [20].

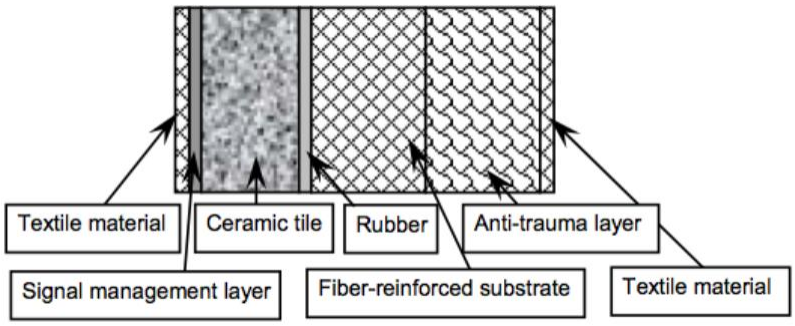

Figure 2-1: Schematic of composite body armour design with the impact face on the left [Adapted from [18]***].***

Ceramic-composite armour (Figure 2-1) consisting of disturber and absorber layers, uses different defeat mechanisms to overcome the threat during the various stages involved in stopping an incoming projectile. The ceramic disturber layer is used to blunt or potentially shatter the projectile

as well as taking it off-axis to reduce penetration of the underlying absorber. The disturber also dissipates a significant amount of the projectile's kinetic energy. In the case of ceramics, this energy is dissipated through fracture. The absorber layer primarily collects the decelerated projectile and spreads the momentum over a larger area to reduce behind armour blunt-force trauma, although the absorber layer can also dissipate kinetic energy through delamination and fibre splitting [3].

The ceramic disturber layer is often designed as a removable plate that is only inserted when entering a higher threat environment [21]. This gives considerable opportunity for after-market ceramic technologies to be retrofitted to existing armours with minimal additional cost. The current ceramic inserts for the British military's Osprey Mk 4 body armour features front and rear ceramic trauma panels as well as side inserts for greater protection. The majority of ceramic inserts for modern armour are monolithic plates with a confinement hoop to maintain some degree of structural integrity upon fragmentation and that also serves to increase the hydrostatic pressure and therefore the yield stress of the ceramic [22]. The National Institute of Justice (NIJ) has developed a standard against which body armours can be compared (Table 2-1). This provides a standard for body armour manufacturers to rate their armour in comparison to a series of standards threats.

Table 2-1: National Institute of Justice standards for ballistic performance [23]**.**

ARMOUR RATING	***TEST ROUNDS***	***TEST BULLETS***	***BULLET MASS***	***CONDITIONED ARMOUR TEST VELOCITY***	***NEW ARMOUR TEST VELOCITY***	***SHOTS REQUIRED***
IIA	*1*	*9 mm FMJ RN*	*8.0g*	*355 m s^{-1}*	*373m s^{-1}*	*144*
	2	*0.40 S & W FMJ RN*	*11.7 g*	*325 m s^{-1}*	*352 m s^{-1}*	
II	*1*	*9 mm FMJ RN*	*8.0 g*	*379m s^{-1}*	*398m s^{-1}*	*144*
	2	*0.357 Magnum JSP*	*10.0 g*	*408 m s^{-1}*	*436 m s^{-1}*	
IIIA	*1*	*0.357 SIG FMJ FN*	*8.1 g*	*430 m s^{-1}*	*448 m s^{-1}*	*144*
	2	*0.44 Magnum SJHP*	*15.6 g*	*408 m s^{-1}*	*436 m s^{-1}*	
III	*1*	*7.62 mm NATO FMJ*	*9.6 g*	*847 m s^{-1}*		*24*
IV	*1*	*0.30 Calibre AP M2*	*10.8 g*	*878 m s^{-1}*		*24*

2.3 CERAMIC ARMOUR AND CERAMIC MATERIAL PROPERTIES

There are several properties of ceramics that make them particularly appropriate for use in armour designs. Primary among those properties are their high hardness, high yield stress, high bulk and shear moduli and relatively low density [19]. It is of particular note that the yield stress of ceramics is often highly dependent on the ambient pressure applied to it (a proposed model of this

relationship will be discussed later). This is useful in that ballistic impacts often induce a high pressure in the target, but it must also remain a consideration in the design of the armour system to ensure pressure can be maximally maintained [2]. However, ceramics are also very brittle and have low fracture toughness (K_{IC}) having values in the range 1-5 MPa $m^{½}$ compared to a range of 5-170 MPa $m^{½}$ for metals [24]. This severely limits multi-hit performance as the cracks that propagate through the ceramic plate produce a large damage zone within the armour with severely compromised ballistic integrity against a second impact [25]. An overview of the material properties of a range of ceramics is presented in Table 2-2.

Table 2-2: Summary of a range of ballistic grade ceramics [11]**.**

CLASS OF MATERIAL	***SOURCE, GRADE***	***DENSITY (KG M^{-3})***	***HARDNESS (GPa)***	***ELASTIC MODULUS (GPa)***	***FLEXURAL STRENGTH (MPa)***	***FRACTURE TOUGHNESS (MPa M$^{-½}$)***
Al_2O_3	*CoorsTek, AD85* [26]	*3420*	*9.4*	*221*	*296*	*3-4*
Al_2O_3	*CoorsTek, AD998* [26]	*3920*	*14.1*	*370*	*375*	*4-5*
TiB_2	*CoorsTek, PAD* [26]	*4480*	*26.4*	*55*	*275*	*~7*
SiC	*CoorsTek, SiC-N, PAD* [26]	*3200*	*32.5*	*460*	*570*	*~5*
SiC	*MCC, RSSC* [27]	*3106*	*24.5*	*399*	*504*	*NR*
B_4C	*CoorsTek, PAD* [26]	*2500*	*25.5*	*460*	*410*	*4*

The precise relationship between ceramic material properties and the failure mechanisms observed during ballistic penetration are not well known [1]. However, several strong correlations between certain material properties and ballistic performance have been found. Hardness, bulk modulus, yield stress and fracture toughness all appear to correlate positively with ballistic performance [28,29]. Hardness of the ceramic, found through indentation tests, can be used to predict ballistic performance in terms of V_{50} (i.e. the velocity at which there is a 50% probability of penetration occurring in physical testing) and is a greater predictor of performance than fracture toughness for thinner tiles [30]. For larger tiles the dwell time is longer and thus allows for more complex fracture mechanics to develop, changing the defeat mechanisms and altering the predictive influence of the ceramic material properties such that fracture toughness and yield stress become more relevant [31].

One measure that has been reliably found to be positively correlated with ballistic efficiency is the normalised effective strength, defined as the average of the static and dynamic yield strength normalised by the density of the material [32]. Ballistic efficiency (η), through depth of penetration (DoP) tests of ceramic tiles backed by an aluminium block, is defined as

$$\eta = \frac{\rho_{Al} P^*_{Al}}{\rho_c h^*_c} \quad (2\text{-}1)$$

where h^*_c is the tile thickness required to prevent penetration for a given projectile and P^*_{Al} is the penetration into a bare aluminium backing for the same projectile and ρ_c and ρ_{Al} are the densities of the ceramic and aluminium respectively. In the same study [32], a linear relationship was found between η and normalised effective strength. This method of characterisation is made difficult by the complexity of measuring the dynamic strength of the ceramic i.e. the compressive strength of the ceramic under uniaxial strain conditions known as the Hugoniot elastic limit (HEL). During the dynamic loading in which the HEL is measured there are high hydrodynamic pressures that are not maintained during quasi-static loading, this is the main reason for the difference between static and dynamic loading.

The low tensile strength of ceramics is the primary factor in limiting ballistic performance as this is the mode of failure during any flexural stresses and during the development of axial cracking due to tensile stress fields generated during an impact. The tensile strength of a ceramic is often an entire order of magnitude lower than its compressive strength. For example, a standard commercial alumina exhibits a compressive strength of 2.95 GPa whilst having a tensile strength of only 130 MPa [33]. Further, the strain to failure of ceramics is very low relative to more ductile alternatives such as metals, the same commercial alumina exhibiting a plastic strain to failure of less than 1%., although precise failure is highly probabilistic and is related to the distribution of micro-defects in the ceramic. These negatives are offset by the much lower density, higher elastic impedance and greater compressive strength relative to most metals as well as the significantly higher hardness that enables good performance against armour-piercing rounds.

Defeat of a projectile in a ceramic armour system is generally considered to occur in three stages: shattering, erosion and capture (Figure 2-2) [34]. The ceramic is responsible for the first two stages and any backing material, e.g. a polymer fibre composite or metal, is responsible for increasing the stiffness of the ceramic during those stages followed by the final stage of capture. On initial impact, the high relative hardness and compressive strength of the ceramic overmatches the projectile causing it to deform and shatter. The contact can be considered Hertzian in nature until the projectile material yields, at which point it is no longer behaving elastically and the contact pressures are greatly diminished [35].

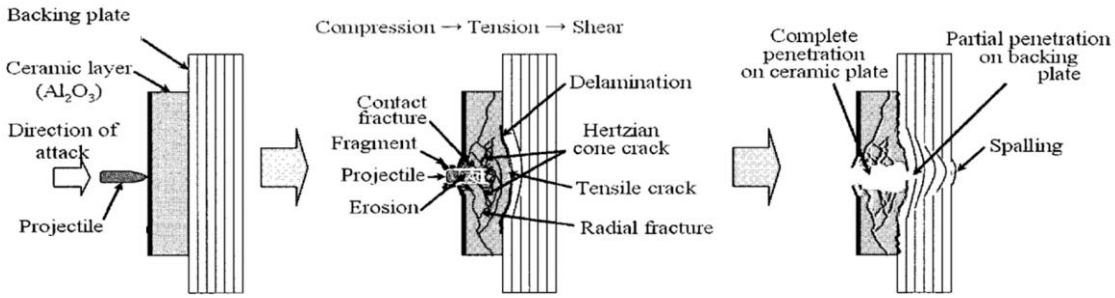

Figure 2-2: A schematic of a ceramic armour under impact showing the development of a fracture zone ahead of the projectile and subsequent crack propagation and spalling [Reproduced from [36]***].***

In the case of a steel projectile impacting an alumina plate at 1000 m s^{-1}, there is an immediate pressure of ~20 GPa generated directly below the point of impact (PoI). This stress exceeds the compressive strength of alumina (~2-7 GPa) but, as the pressure rapidly drops off due to relief waves from free surfaces down to around 2 GPa, the plastic yield in this initial stage of compressive failure is relatively limited, i.e. this stage is limited to less than ~3 μs after impact [11]. Although the relief waves are the primary and most common reason for alleviation of this pressure, changes in the ceramic lattice structure such as dislocations and amorphization also contribute. The compressive stress during this time leads to the development, of a Hertzian ring crack of a diameter slightly larger than that of the projectile as well as radial cracks propagating out along the front surface due to subsurface plasticity [37]. This ring then develops into a fracture conoid spreading out downwards from the PoI towards the rear surface (Figure 2-3, Figure 2-4). Momentum dissipation into the backing material occurs over the surface in which this fracture conoid is in contact with. A low-density material is preferred for the ceramic due to the increased thickness for the same areal-density that this affords. A thicker plate allows for a wider fracture conoid and greater dissipation of the impact force.

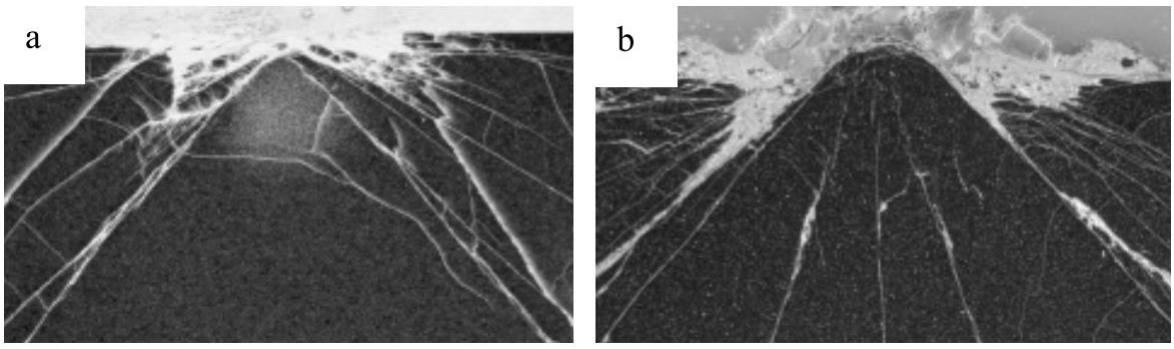

Figure 2-3: Fracture conoids induced by a cemented carbide sphere impact shown in cross-section in (a) SiC [38] ***and (b) B_4C [Reproduced from*** [39]***].***

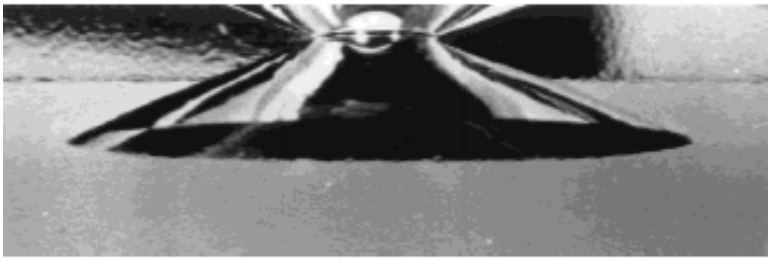

Figure 2-4: A fracture cone produced by an impact force of 4kN in a transparent soda lime glass specimen. The cone is approximately 30 mm in diameter and 7 mm deep [Reproduced from [40]***].***

However, these compressive shockwaves are reflected as tensile waves from the rear surface inducing a tensile stress field of 300-500 MPa (in this example). The period between the initial impact and the shockwaves travelling through and back to the surface of the ceramic is referred to as dwell (or dwell time) [41]. The tensile strength of ceramics is often at least an order of magnitude lower than the strength under compression and it is this reflected tensile stress that initiates axial cracking at the rear surface of the ceramic. The fracture conoid already created in the initial stage is then subject to the reflected tensile wave and considerable further damage is induced. The material beneath the PoI is broken into fine ceramic fragments, i.e. comminuted. The projectile begins to penetrate through the ceramic material and is subject to erosion by the comminuted material. As the backing material begins to move and the ceramic is allowed to bend, hoop stresses that exceed the biaxial flexural strength of the ceramic develop and radial cracking occurs on the back face. A stiffer backing material could delay the onset of these axial cracks and improve performance [42].

The jacket of the projectile is stripped during this stage and the remaining core may lose mass due to erosion. It may also be plastically deformed or shatter if the ceramic is of sufficient hardness. The deformation blunts the projectile allowing for a lower chance of penetration in the later capture stage. The projectile is also likely to be taken off-axis during this stage further lowering penetrative ability. Even in ballistic events leading to penetration, during dwell the ceramic retains its strength and thus ability to deform and decelerate the projectile. It is therefore of great utility in armour design to maximise the dwell time. Various methods of increasing this dwell time have been proposed including increasing strain tolerance, increasing the modulus of the backing material (thus delaying the flexural failure of the ceramic) and using matched acoustic impedances at interfaces between layers to reduce the reflected shockwaves [42,43]. The impedance of any backing material is a strong influence on the behaviour of the reflecting stress waves. A low-impedance support material leads to reflection from the tile/support interface whereas in systems

with a high impedance support material the shockwave, is reflected from the free surface of the support itself, leading to increased dwell time and subsequent lower damage in the latter case [44].

As this secondary stage occurs, circumferential cracks form along the top surface. It is estimated that less than 1% of the total kinetic energy from impact is absorbed via fracturing of the armour material; a large majority of the kinetic energy being dissipated via ejection of spall from the front surface [29]. Remaining energy is absorbed through other forms of material failure such as lattice dislocations and delamination of cohesive layers that may be present in the ceramic-composite system or backing. That which is not dissipated through the armour remains as kinetic energy that must be dissipated over as large an area as possible during capture, assuming an event in which penetration does not occur, to prevent blunt force trauma.

The final defeat stage, capture, refers to momentum dissipation in combination with the backing material to collect and stop the fragments of the projectile and damaged ceramic from penetrating further. During this phase and particularly in the inter-phase period whilst the projectile travels through the comminuted ceramic material, there is significant erosion of the projectile leading to mass loss and blunting of the ogival-nose geometry, both factors reducing penetrative capacity and further dissipating or decreasing the kinetic energy that the backing material must absorb [45]. The mass loss during this stage is due to both grinding and surface melting of the penetrator.

The damage to the ceramic accumulated in these phases are generally divided into four distinguishable failure modes: lattice plasticity, micro-cracking, radial cracking and the development of a fracture conoid [35]. Micro-cracking can be further divided into transgranular cracking directly through grains and intergranular microcracking following grain boundaries, the specific behaviour being dictated by whichever is the lowest energy path. The presence of these various failure modes during any specific impact is dependent upon the impact velocity of the projectile and, especially in the case of radial cracking, the thickness of the impacted ceramic (Figure 2-5). At lower velocities, only cone formation occurs. Radial cracks, lattice plasticity and microcracking occur successively at increasing velocities.

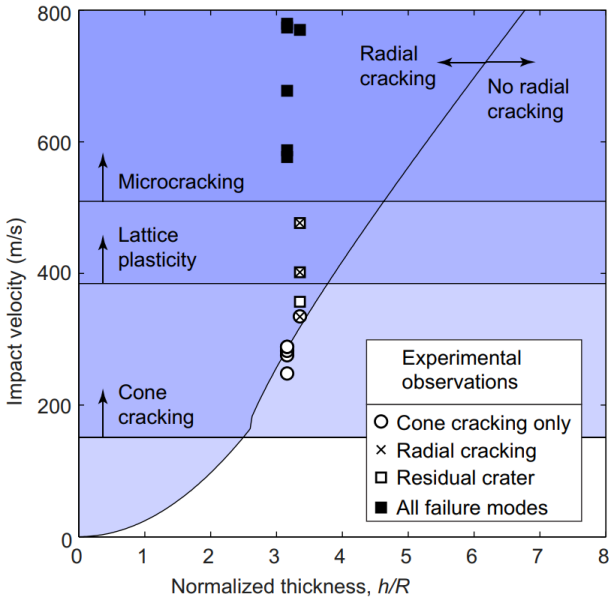

Figure 2-5: Failure map showing the observed failure modes for an alumina tile impacted by a spherical steel projectile. The zone markings are derived from theoretical predictions of failure mode boundaries [Reproduced from [35]***].***

Of the two granular fracture modes described as micro-cracking, intergranular fracture failure is correlated with a higher fracture toughness. This is believed to be a result of the path of the crack itself being more circuitous as it follows the grain boundaries, as opposed to propagating with much less deviation from its overall direction of travel in transgranular failure. However, despite the difference in fracture toughness there is no correlation observed between fracture mode and ballistic performance in experiments using 14.5 mm WC-CO ammunition against hot pressed SiC targets [46]. These experiments found that the granular fracture mode could be chosen during the sintering process with the inclusion of greater Al content in a SiC sintering process mediated by Al, B and C. However, this led to a reduction of the hardness of the material. It is hypothesised however that an optimum threshold limit may exist in which most of the hardness could be retained without the sudden drop in fracture toughness that occurs when the granular fracture mode transitions to transgranular failure, and therefore greater ballistic performance obtained, if the strength of the grain boundaries could be tuned to "just below" the strength of the grain itself [1]. However, testing for this optimum threshold and then achieving it consistently is non-trivial due to the high degree of compositional control required during manufacture. An inappropriate manufacture method may lead to ceramic failure due to porosity or some other defect in the quality of the ceramic when impacted rather than at grain boundaries or directly beneath (and radially out from) the POI as expected.

There are several types of lattice plasticity that can occur within the crystal structure of the ceramic. Dislocation defects within the crystal lattice can be caused to move until the grain boundary or another defect is met. Twinning may also occur in which multiple crystal lattices are forced to share the same atoms along an intermediate boundary. In some materials, such as boron carbide, at high impact velocities, amorphization may occur in which shock loading leads to a significant change in the lattice structure and the development of amorphous bands that are visible through HREM (Figure 2-6) [47,48].

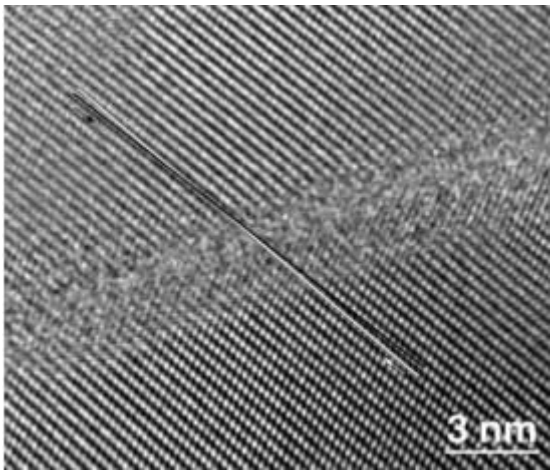

Figure 2-6: Localised amorphization of a boron carbide crystal lattice due to shock loading [Reproduced from [48]***].***

The most commonly used ceramic armours consist of a monolithic insert allowing for the build-up of bulking pressure within the tile and the corresponding increase of effective strength of the ceramic. This build up is alleviated in the volume close to the ceramic surface by relief waves. This alleviation is a primary reason for the reduction in performance of tile-based systems as greater total volume is subject to these edge effects. Lateral and surface confinements also take advantage of the same mechanism to increase performance. Having sufficiently large tiles also produces an effective lateral confinement of the material away from the edge by the surrounding ceramic. Surface confinement can be applied via a cover-plate, some form of over-wrap or through a shrink-fitted metal casing [49]. In practical terms, confinement can often add considerable weight to an armour system and is often heavily dependent on impact location.

Quasi-static compression tests on the effects of radial confinement on ceramic behaviour, with confinement pressure up to 1.25 Gpa, show significant increases in the strength of the material. For alumina, a 33% increase in strength from 4.5 GPa to 6.0 Gpa has been demonstrated as the confinement pressure increases from 0.1 MPa to 1.25 GPa [50]. Two other ceramics, aluminium nitride and beryllium oxide, have been shown to exhibit a brittle-ductile transition at confinement

pressures of 0.5-07 GPa in which plastic flow is observed instead of the brittle failure that occurs without confinement. For these ceramics, the ultimate compressive strength increase is much greater than for alumina at 47% and 111% for AlN and BeO respectively achieved through confinements of ~1.0 Gpa.

A further mechanism explaining the performance increase with confinement is related to the difference between comminuted ceramic and ceramic powder. As discussed, during impact the material beneath the PoI is comminuted. However unconfined ceramic material at the tile surface is not merely fragmented but becomes a powder. The difference is that the comminuted material retains some grain structure and exhibits some interlocking (Figure 2-7). The comminuted material has a three to four times higher bulk modulus compared to the powdered equivalent and exhibits greater resistance to the bullet during penetration [51].

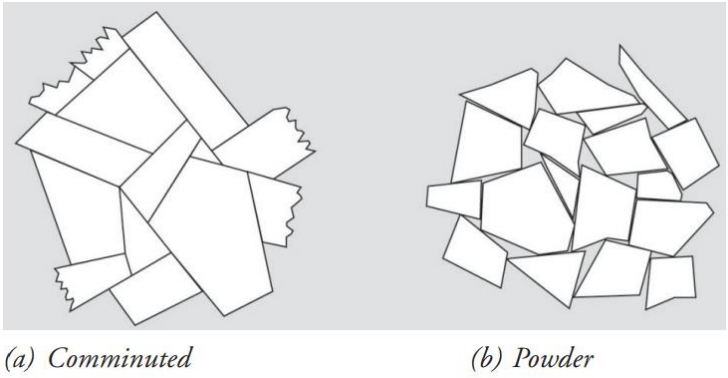

Figure 2-7: Schematic showing the difference in interlocking between comminuted and powdered ceramic material [Reproduced from [51]***].***

Ceramics exhibit a clear transition velocity in their response to ballistic impacts, i.e. an impact velocity above which penetration of the ceramic starts to occur. At velocities below this, the ceramic is extremely strong and provides a high degree of protection against incoming threats. Above this velocity, however, the ceramic suffers a considerable reduction in strength (Figure 2-8). Lundberg et al [52] have proposed that the onset condition of transitional failure is the point at which the boundary of the plastic yield zone produced beneath the point of impact is large enough to reach the surface causing a collapse in the damage zone ahead of the projectile (Figure 2-9). This appears to be dependent on surface pressure and it is an important factor when designing armour systems for specific threat environments as the projectile itself has a strong influence on the fracture modes initiated within the ceramic armour.

Experiments using a tungsten projectile have determined that the transition velocity increases with fracture toughness but not with Vickers hardness, a measure strongly related to the shear yield

strength [52]. This suggests that once the ceramic exhibits a hardness sufficiently greater than that of the projectile a discrete shift in the failure mechanics occurs and further increases in hardness yield only limited improvements in performance.

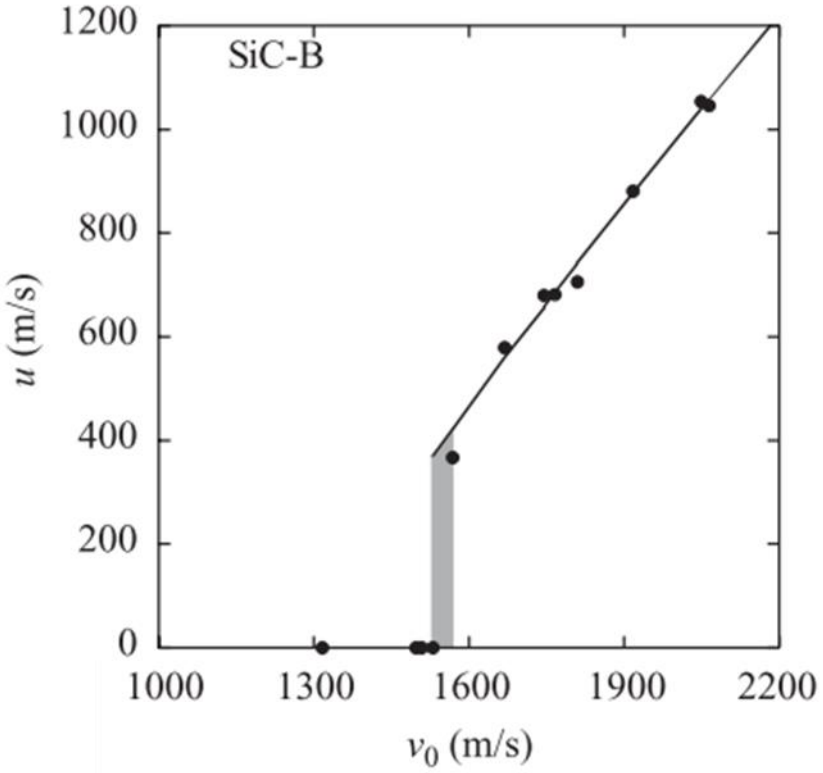

Figure 2-8: Penetration velocity versus impact velocity for boron-doped silicon carbide. Transition velocities shaded grey [Reproduced from [33]***].***

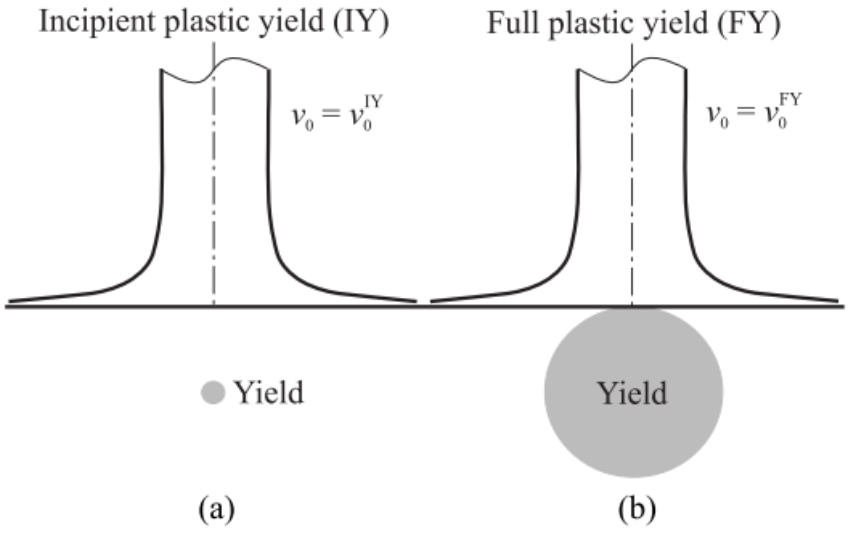

Figure 2-9: Plastic yield zones beneath the point of impact (a) below the transitional velocity and (b) above the critical velocity [Reproduced from [52]***].***

2.4 PROJECTILE BEHAVIOUR DURING IMPACT

At different projectile velocities, the contact pressures and forces exerted by the projectile during impact can be characterised in three different behavioural regimes [35]. At low impact velocities (e.g. 5 m s^{-1}), the projectile behaves almost completely elastically and quasi-static Hertzian analysis is an appropriate tool for predicting the contact force for the full duration of the impact event. The contact pressure is constant during the impact and, as shown in Figure 2-10a, closely matches the Hertzian elastic solution. The deviation is likely due to the friction, which is excluded in Hertzian analysis, or some yielding occurring in the projectile. The pressure is highest at the centre of the impact and decreases $\alpha\ (1-r^2)^{\frac{1}{2}}$ towards the outer radius of the projectile.

At high velocities (e.g. >500m s^{-1}), a shock front is established in the projectile and the stresses present are, in most cases, much greater than the yield stress of the projectile material such that the behaviour is equivalent to that of a liquid droplet. This shock front is generated in the projectile when the rate of expansion of the contact radius is greater than that of the wave speeds in the projectile and the target. Unlike in the low velocity case, the peak pressure generated is effectively independent of the projectile yield strength and instead is described by the "water hammer pressure" from liquid impact theory. The contact pressure is uniform in the vicinity of the PoI and peaks towards the outer radius of the contact. In this theory the peak pressure is only proportional to the acoustic impedance of the contact, dilatational wave speed and the impact velocity (Figure 2-10b)[53]. This pattern of contact pressure distribution is maintained until the contacting face of the projectile is slowed to below the acoustic wave speed of the projectile material (~6000 m s^{-1}) at which point release waves from the free surfaces can relieve the pressure leading to an overall drop in the contact pressure. As the projectile begins to deform, the contact surface increases and, as a consequence, the imparted force increases until it reaches a maximum as the contact surface expands to a radius equal to that of the projectile radius. The time at which this occurs is independent of elastic/plastic properties and instead is solely dependent on the velocity and radius of the projectile. This time, t_f^*, has been found to be given by

$$t_f^* = \frac{R}{3V_0} \qquad (2\text{-}2)$$

where R is the radius of the projectile and V_0 is the impact velocity [35]. The independence of this relationship from the material properties of the projectile suggest that the phenomena of maximal force during high velocity impacts is governed by hydrodynamic incompressible flow. This stands distinct from the phenomena related to the maximum pressure during the same impact that is

governed by shock front generation, a behaviour ultimately dependent on Young's modulus, density and Poisson's ratio.

At intermediate velocities (e.g. 50 m s^{-1}), the Hertzian assumptions do not hold and neither is a shock front developed as the rate of deformation is below the material wave speed. The projectile yields locally around the point of impact leading to a pressure distribution that is approximately uniform over the contact area (Figure 2-10b). The contributions to the contact pressure can be broken down into a plasticity-related component and a component dependent on plastic wave propagation, although projectile plasticity dominates. The observed failure modes of the ceramic (Figure 2-5) can be dictated by both the local contact pressures and the total forces applied by the projectile which vary across these velocity-characterised behavioural regimes. This interdependence can give rise to non-intuitive behaviour such as impacts of long rod penetrators into metal targets having some circumstances in which a reduction of the impact velocity leads to greater DoP due to a transition from fluid behaviour at the higher velocity to rigid behaviour at the lower [54].

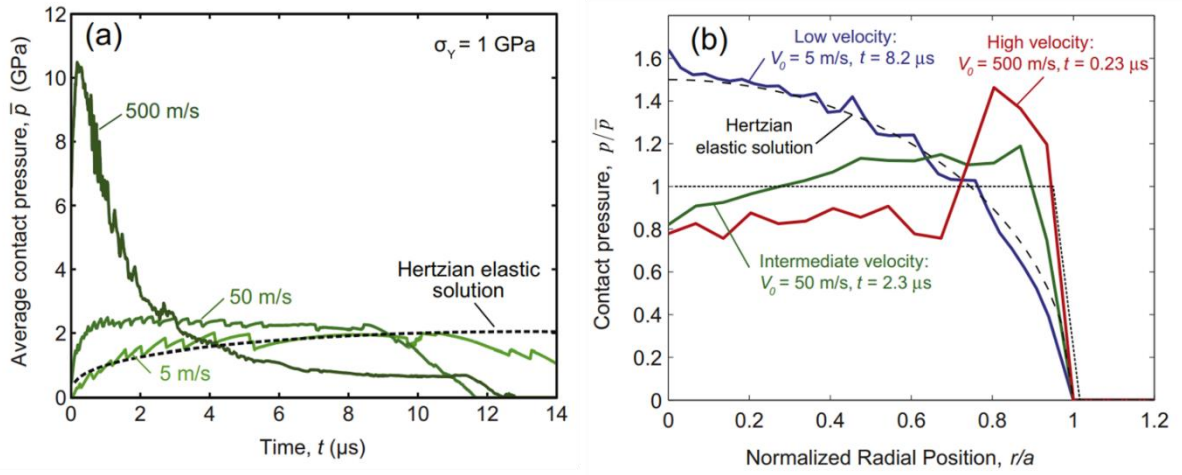

Figure 2-10: (a) Time history of contact pressure for an FE simulation of a metal sphere impacting a ceramic with a yield stress of 1 GPa at 5,50 and 500 ms^{-1} compared to a Hertzian analysis prediction. (b) Contact pressures of the same impacts as a function of radial distance from the projectile centre [Reproduced from [35]***].***

2.5 PROJECTILE THREAT

The specific threat that this work will be oriented towards overcoming is the 7.62 mm AP M2 round impacted at 878 m s^{-1} (Figure 2-11). An armour that provides protection against a single impact of this projectile at this velocity is classified as NIJ IV (Table 2-1). The total weight of the round is 10.7 g with the hard steel core comprising 5.25 g. The steel core has an ogive-nose with a calibre-radius-head of 3.0, a density of 7850 kg m^{-3} and a Rockwell scale hardness of 63 [55].

There are several existing personal armour systems capable of protecting against this threat. The goal of this work is to investigate novel methods of protecting against multiple impacts and, ideally, without a dramatic increase in the areal-density.

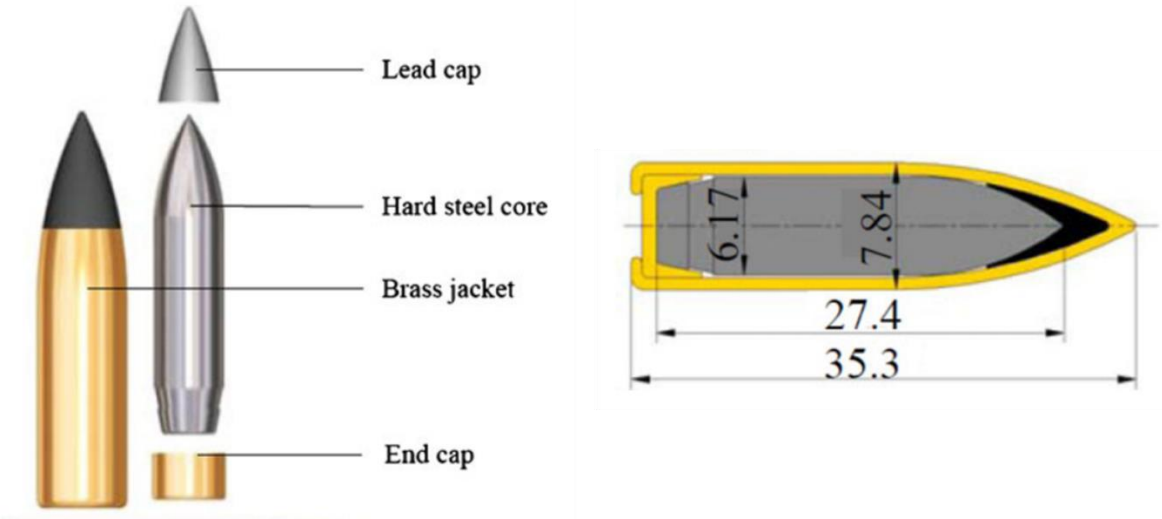

Figure 2-11: The geometry and constituent elements of the 7.62mm AP M2 bullet [Reproduced from [55]***].***

2.6 TILED SYSTEMS AND MULTI-HIT PERFORMANCE

In scenarios in which the wearer faces rapid machine gun fire or prolonged engagements, it is of great utility for the armour used to be able to provide ballistic protection against multiple successive impacts. The inherent brittleness of ceramics can often lead to cracks freely propagating from the point of impact until stopped by a free surface. This can strongly inhibit multi-hit performance as secondary impacts are highly likely to impact an area in which the material is, in some way, damaged. This can lead to a very large reduction in ballistic performance against a second impact. For example, on an otherwise undamaged target, impact in close proximity to a pre-existing 1 mm crack reduces performance by 9% [27]. In practice, a ceramic target that has been impacted once will likely have much more than a single crack in proximity to any secondary impact site and thus performance drops much further.

Confinement, as well as improving the single shot performance as discussed, can maintain the integrity of the structure of the armour even after the armour material itself is damaged and comminuted. This provides much greater performance than if the damaged material had not been retained in place but retaining undamaged material and localising crack propagation will provide much greater gains in multi-hit performance. To achieve this, mosaic tiled armours have been designed with the intent that cracks will be inhibited at tile boundaries. This is possible as the

nucleation energy for a crack is much greater than the energy required for propagation. Cracks may still propagate over tile boundaries but only if there is sufficient energy.

Tile performance drops off in close proximity to the tile edge and as such it is recommended that tiles be ~10 times the size of the core of the projectile it is protecting against (for small arms) [11]. Experiments on 85 mm thick hot-pressed silicon carbide tiles showed that the increase in DoP increases from 16mm to 44mm when comparing impacts at 42 mm and 12 mm away from the closest border [24]. These experiments also showed that the fragmentation of the projectile was significantly less after impacts close to the tile border. This is likely a consequence of the reduction in strength of the ceramic due to the reduced confinement as well as earlier onset of damage caused by reflected stress waves from the closer free surfaces. Ceramics that do not damage the projectile core in this way under ideal impact conditions do not appear to show this behaviour. Edge geometry such as chamfers can improve the performance under such conditions and mitigate the need to resort to thicker tiles to provide the same level of protection when deploying a tiled design (Figure 2-12). In designs employing a 45° chamfer at the tile edge, a 6 mm thick tile was shown to have the similar performance as an 7.5mm thick straight-edged tile when impacted within 5 mm of the tile, leading to potential weight savings of almost 30% [2].

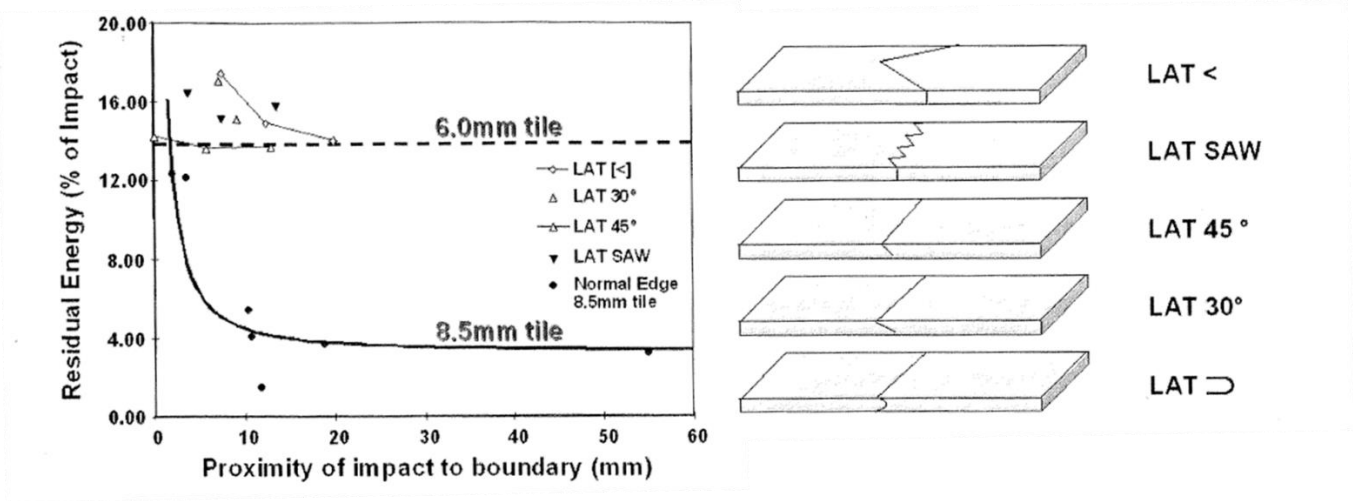

Figure 2-12: Comparison of the residual kinetic energy after impact for a series of edge profiles as a function of boundary proximity [Reproduced from [2]***].***

In the design of tile armour, greater consideration of momentum dissipation must be taken as, without continuity of the material, the force could be concentrated over a much smaller area of the backing material, a significant problem for users due to behind-armour blunt force trauma [56]. Most designs use some form of mosaic pattern and, further to this, stagger the arrangement to

reduce quad-points to triple-points (Figure 2-13) [11]. An overlapping design may allow for greater dissipation of momentum between tiles while still retaining the localisation of the damage.

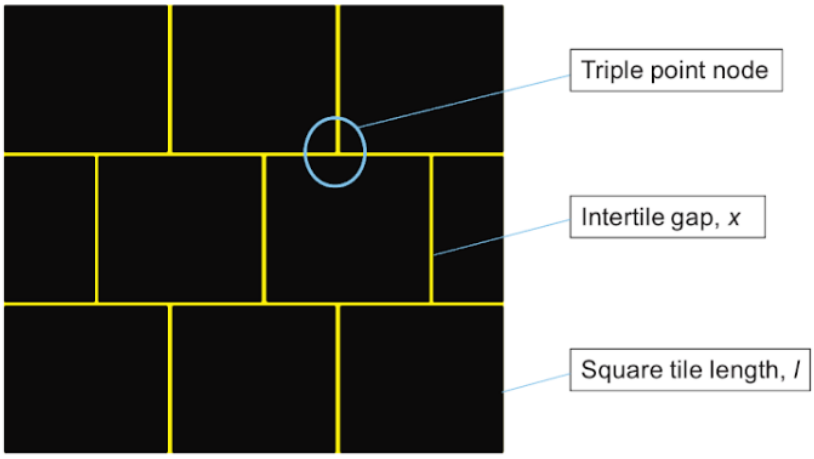

Figure 2-13: A schematic of an offset mosaic tile system [Reproduced from [11]***].***

There are several conflicting factors when considering the adhesive layer that is necessary to maintain the structural integrity of a tiled armour. Greater adhesion results in higher absorption of energy as the adhesive fails, however it may result in a smaller distribution of the load resulting in greater stresses exerted onto subsequent layers and onto the wearer. Weaker adhesion absorbs less energy and may not confine the damaged material well to maintain ballistic performance over multiple impacts. Further, thin adhesive layers confer greater performance over a single impact in a mosaic armour but leads to greater damage of adjacent tiles resulting in lower multi-hit performance [57].

Any tiled system introduces a greater number of interfaces closer to the point of impact in comparison to a monolithic ceramic. If there is a mismatch of acoustic impedance between the materials on either side of the interface, both reflected tensile and transmitted compressive waves are generated. In tiled armour, this impedance mismatch occurs due to the presence of the adhesive required to bind the tiles together as well as at the rear surface at the contact with the absorber layer, as in monolithic armour. The difference in wave speed between the compressive waves either side of the interface produces shearing that can cause adhesive failure in the interlayer. The resultant damage from the tensile wave has already been discussed. Although it should be noted that the reduction in dwell time due to the interface being closer to the surface of the armour system is a significant factor in the reduction in ballistic performance of tiled armour compared to monolithic for a single hit.

One method of reducing the reflected stress waves is to use an adhesive that most closely matches the impedance of the ceramic. Alumina has an impedance of 37 MRayls, much higher than that of most epoxy resins that have an impedance ~ 1 MRayls [58]. Using certain ceramic adhesives with an impedance of 6 MRayls has been shown to reduce the reflected stress by 33%. However the adhesion is weaker and mechanical confinement is required to maintain the integrity of the system when such adhesives are used [2]. Mechanical confinements in the form of a surface material over the tiles also serve to pre-strip the jacket of the projectile as well as conferring the same advantages that radial confinement provides, see above. Although consideration must be taken such that, in maintaining a reasonable areal-density, the inclusion of a confining plate does not lead to too great a reduction in the high performing ceramic [59].

When creating a layered ceramic armour with any variation of density between layers, the highest ballistic performance is achieved when layered in order of increasing density in the direction of penetration [60]. In the same analysis it is shown that the ballistic performance of the system as a whole is improved by the placement of higher-performing layers in front of those that perform worse. It follows therefore that for layers of unequal thickness but of the same material, the thicker layers should be at the front to optimise performance [61].

2.7 FINITE ELEMENT ANALYSIS AND THE JOHNSON-HOLMQUIST-2 MODEL

Ballistic trials are often expensive and take considerable amounts of time to plan, manufacture and execute. For an iterative process such as the design of a new armour system, this can be extremely prohibitive. Variations in results due to manufacture defects or slight differences in test conditions are also difficult to control. Finite element analysis (FEA) can be used to overcome both of these limitations as test conditions are explicitly declared and, once the model has been set up, further iterations can be run very rapidly [11,62]. Further, FEA can be used to test geometries that would be difficult to manufacture to determine whether physical testing of a certain design is worth pursuing. With these benefits, however, comes the requirement to validate the model with physical test data as well as a duty by the researcher to limit the extent of the conclusions drawn from models that are simplifications of the physical reality they are designed to simulate.

The current standard ceramic material model most commonly used in finite element analysis is known as the Johnson-Holmquist-2 (JH-2) model; first developed by Gordon Johnson and Timothy Holmquist in 1994 as an improvement over their earlier work [63]. The JH-2 model is a constitutive material model developed to describe the behaviour of brittle materials under high strain and pressure. The notable improvements of this model over previous work is the inclusion

of damage parameters that allow for the gradual accumulation of damage to be taken into account and give an approximation of the strength of the ceramic during failure [64]. It also allows for several of the material properties (described below) to vary with pressure with an analytic function as compared to the sectioned linear variation in their older legacy material model (Figure 2-14).

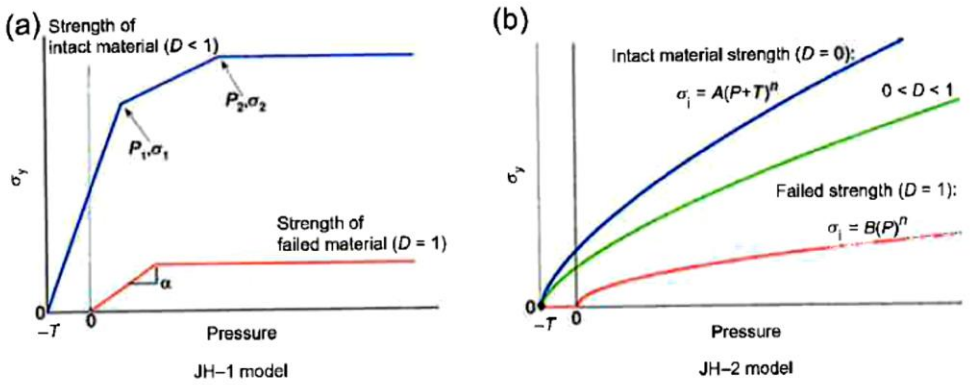

Figure 2-14: Description of the evolution of the Johnson-Holmquist models [Reproduced from [11]***].***

In the Johnson-Holmquist 2 (JH-2) model, the normalised equivalent stress of the material is based on the hydrostatic pressure, P (Figure 2-14). The effective yield stress, σ^*, transitions between an intact, σ_i^*, and fractured, σ_f^*, strength curve according to

$$\sigma^* = \sigma_i{}^* - D\left(\sigma_i{}^* - \sigma_f{}^*\right), \tag{2-3}$$

as damage, D, accumulates from 0 to 1. The asterisk indicates that the value is normalised with respect to the hydrostatic pressure at the Hugoniot elastic limit (HEL). The normalised intact strength of the undamaged material, i.e. D = 0, is

$$\sigma_i{}^* = A(P^* + T^*)^N(1 + \mathrm{C}\ln\dot{\varepsilon}) \tag{2-4}$$

where $P^* = P/P_{HEL}$ and $T^* = T/P_{HEL}$, T being the tensile strength of the material derived from experimentation. $\dot{\varepsilon}$ is the equivalent strain rate, i.e. the actual equivalent strain rate normalised by a characteristic reference strain rate. The normalised fractured strength of the fully damaged material, i.e. D = 1, is

$$\sigma_f{}^* = B(P^*)^M(1 + \mathrm{C}\ln\dot{\varepsilon}). \tag{2-5}$$

A, B, M and N are not directly measurable experimentally and are calibration variables that are approximated from experimental data and then calibrated to match characteristic material behaviour during development of a specific series of finite element analyses [52]. C is the strain

rate dependence of the material. The equations of state for the hydrostatic pressure response of the material are

$$P = k_1\mu + k_2\mu^2 + k_3\mu^3 \qquad (2\text{-}6)$$

in compression and

$$P = k_1\mu \qquad (2\text{-}7)$$

in tension. The parameters k_1, k_2 and k_3 are constants. μ relates to the change in density due to bulking and is defined as

$$\mu = \frac{\rho}{\rho_o} - 1. \qquad (2\text{-}8)$$

In the Johnson-Holmquist 2 model, the damage variable, D, accumulates over time as

$$D = \max\left(\sum \frac{\Delta\varepsilon_p}{\varepsilon_p^f}, D_{t-1}\right) \qquad (2\text{-}9)$$

in which $\Delta\varepsilon_p$ is the equivalent plastic strain increment during a cycle of integration and ε_p^f is the calculated equivalent plastic strain to failure. The uniaxial stress-strain curve at a constant pressure is shown in Figure 2-15 and with confinement allowing for the build-up of hydrostatic pressure in Figure 2-16.

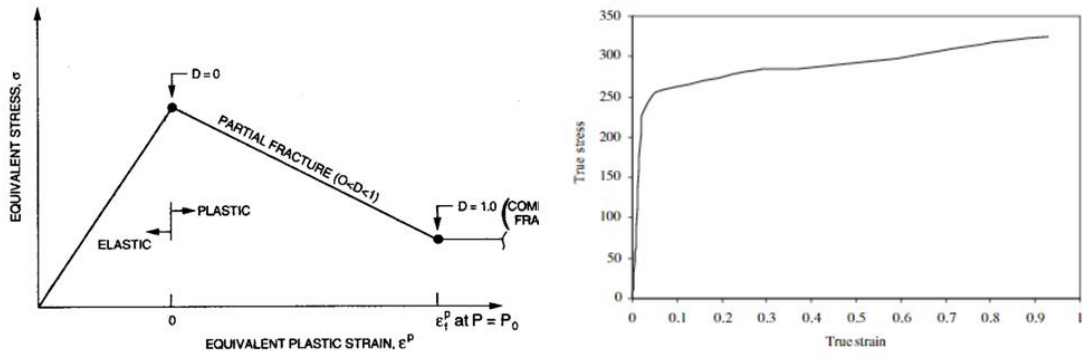

Figure 2-15: (Left)The stress-strain curve during uniaxial loading (compression) for the Johnson-Holmquist 2 model at a constant pressure, P_0. This shows the softening effect of the model as damage is accumulated during partial fracture [Reproduced from [63]***]. (Right) The true stress-true strain curve for the same loading conditions (shown qualitatively with arbitrary units). [Reproduced from*** [65]***].***

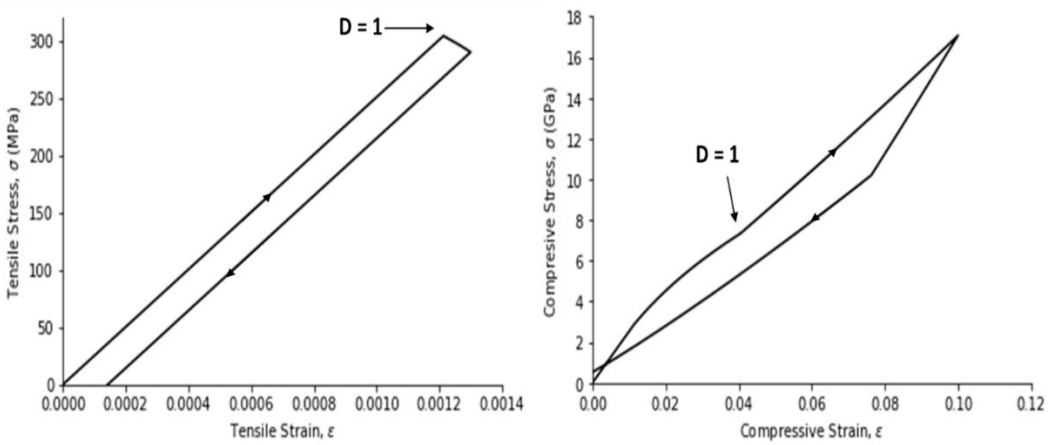

Figure 2-16: Stress-strain curve of an alumina ceramic under tensile (left) and compressive (right) loading and unloading when lateral surfaces are confined i.e. hydrostatic pressure is allowed to build. Material properties taken from [22]***.***

This material model uses a radial return method in which a trial stress is calculated assuming a perfectly elastic response to the calculated nodal displacement and then, if the trial stress is greater than the yield stress, resolved to return the stress to the maximum yield stress. The trial stress is calculated by

$$\boldsymbol{\sigma}^{\boldsymbol{trial}} = \boldsymbol{\sigma}_t + 2\,\mu\,\dot{\boldsymbol{\varepsilon}}\,\Delta\mathrm{t} \tag{2-10}$$

where Δt is the time-step, σ_t is the stress state from the previous time step and the strain rate, $\dot{\varepsilon}$, is calculated from nodal accelerations and velocities. Multi-axial stress and strain scenarios are handled using the von Mises formulation to produce a scalar stress value, $\overline{\sigma^{trial}}$ from the double dot produce of the deviatoric component, S^{trial}, of the stress tensor for comparison against the given yield criterion:

$$\overline{\sigma^{trial}} = \sqrt{\frac{3}{2}\boldsymbol{S}^{\boldsymbol{trial}} : \boldsymbol{S}^{\boldsymbol{trial}}}. \tag{2-11}$$

Similarly, multi-axial strain is handled using a von Mises yield condition such that the effective strain rate is

$$\dot{\varepsilon} = \sqrt{\frac{2}{3}\dot{\varepsilon}_{ij}\dot{\varepsilon}_{ij}}\ . \tag{2-12}$$

From this effective strain rate term, the equivalent plastic strain increment for a given time step can then be calculated by

$$\Delta\varepsilon_{\mathrm{p}} = \dot{\varepsilon}\,\Delta\mathrm{t} - \frac{\sigma^{*}\sigma_{\mathrm{HEL}}}{\mathrm{E}} \tag{2-13}$$

where E is the bulk modulus, the second term being the elastic strain component.

Finally in the radial return method, if the trial stress is outside of the yield surface in the material stress-space, the stress is updated by taking a projection of the trial stress to the nearest point on the yield surface. The excess stress is alleviated by an increment in the equivalent plastic strain and the deviatoric stress state for the element is "returned" radially to the yield surface in stress space and updated as

$$\boldsymbol{S_{t+1}} = \frac{\sigma^*}{\overline{\sigma^{trial}}}\, \boldsymbol{S^{trial}} \quad . \tag{2-14}$$

The plastic strain to failure is a function of the applied pressure and is calculated by the equation

$$\varepsilon_p^f = D_1(P^* + T^*)^{D_2} \tag{2-15}$$

where D_1 and D_2 are constants that can be calculated from the experimentally measured failure strain at a known hydrostatic pressure.

Under dynamic loading, the equation of state, Equation*(2-6)*, has an additional increment, ΔP, applied derived from the increase in potential energy as the deviatoric stresses decrease to material softening during the accumulation of damage. The internal energy, U, is related to the non-normalised effective yield stress, σ_Y, of the material i.e. $P_{HEL}\sigma^*$,by the relation

$$U = \sigma_Y^2/6G \tag{2-16}$$

where G is the shear modulus of the ceramic. As σ_Y is dependent on the damage state and hydrostatic pressure, the change in internal energy between successive time steps is also dependent on these states,

$$\Delta U = U_{D(t)} - U_{D(t+\Delta t)}. \tag{2-17}$$

This energy is converted to the aforementioned potential hydrostatic pressure increase, ΔP, and this energy conservation relation is approximated by Johnson and Holmquist as

$$(\Delta P_{t+\Delta t} - \Delta P_t)\mu_t + \frac{\Delta P_{t+\Delta t}^2 - \Delta P_t^2}{2K_1} = \beta \Delta U \tag{2-18}$$

where β is a constant determining the fraction of elastic energy converted to potential energy, typically set to 1; this is the therefore the energy lost due to damage accumulation. Solving for the updated bulking pressure, $\Delta P_{t+\Delta t}$, gives

$$\Delta P_{t+\Delta t} = -K_1\mu_t + \sqrt{(K_1\mu_t + \Delta P_t)^2 + 2\beta K_1 \Delta U} \tag{2-19}$$

This then gives an updated total stress state of

$$\boldsymbol{\sigma} = \boldsymbol{S_{t+1}} + P_{t+1}\,\delta \qquad (2\text{-}20)$$

where δ is the Kronecker delta.This process within the implemented model framework is shown in Figure 2-17.

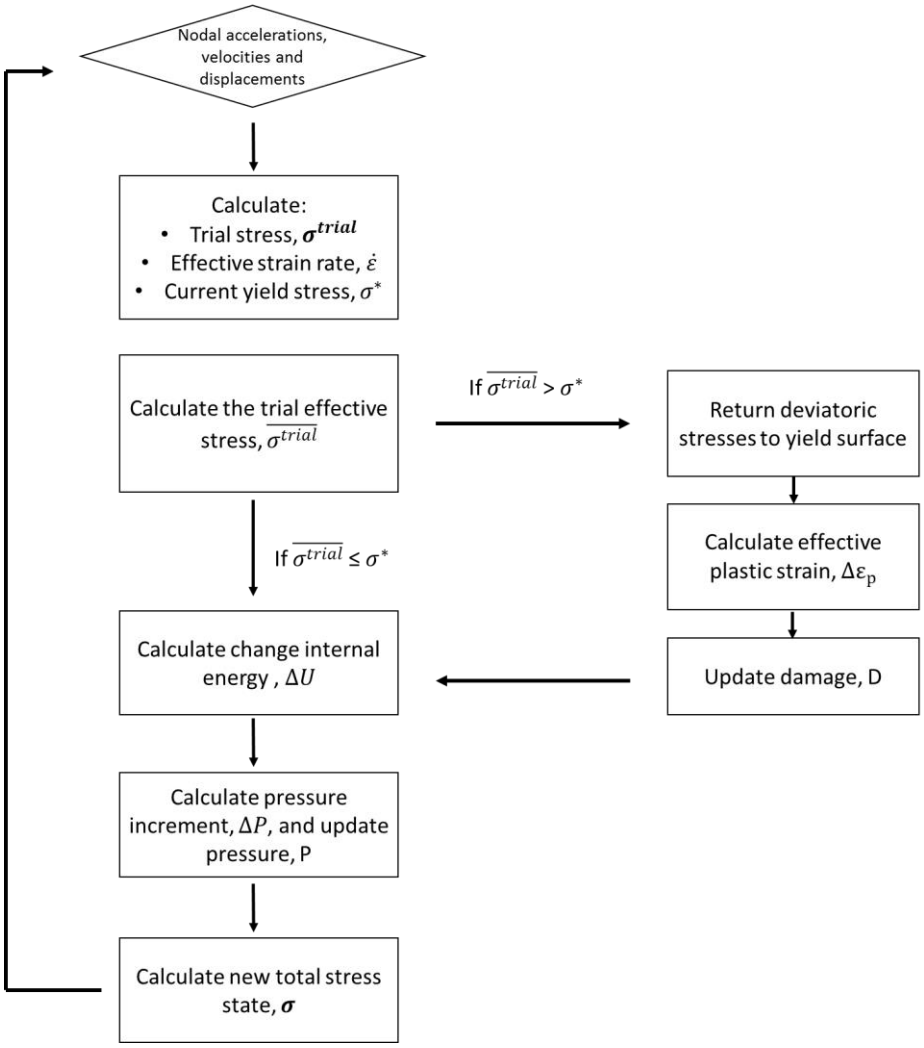

Figure 2-17: Flowchart of the Johnson-Holmquist 2 framework.

This material model has become a reliable, widely used tool for the simulation of ceramic behaviour at both high and low strain rates, and has accurately predicted damage patterns and ballistic performance for a range of ceramics and impact conditions (Figure 2-18, Figure 2-19). Krishnan et al [66] have used this material model to accurately simulate depth of penetration experiments in which boron silicon carbide backed by aluminium is impacted at high velocity (877 m s^{-1}). The end state of these simulations accurately matches the damage pattern for the ceramic armours from physical experiments and were used to determine the kinetic energy absorbed by

different layers within a ceramic-composite armour system. This energy analysis was then used in the development of an optimised ceramic-composite armour proposed by the authors. The researchers found these models required a locally fine mesh (<0.5 mm element length) around the impact site to capture spalling and crack propagation accurately. Some researchers have been critical of this material model, noting that while it is capable of accurately modelling the ballistic performance and the residual damage state of a ceramic impact, it is often difficult to calibrate a given material in order to achieve both [67]. Rahbek et al [67] have shown accurate capture of the damage pattern obtained for medium velocity impacts (299 m s^{-1}) onto alumina using a pseudo-geological model, 72_R3 in LS-DYNA. However, this material model is not widely used as material characterisation for use with this formulation is difficult.

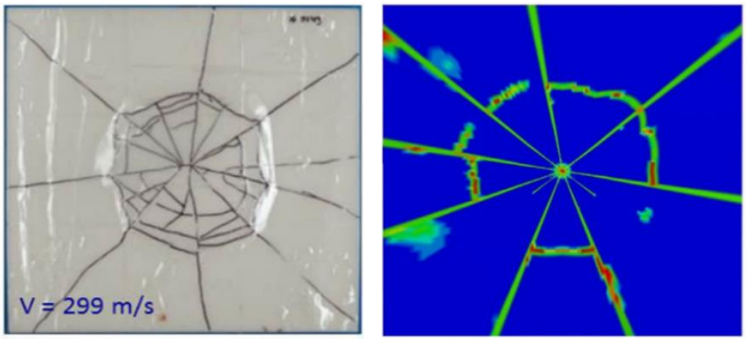

Figure 2-18: A side-by-side comparison of the back surfaces of a ceramic target after projectile impact at a velocity of ~300 m s^{-1}obtained experimentally (left) and through FEA (right) [Reproduced from [67]***].***

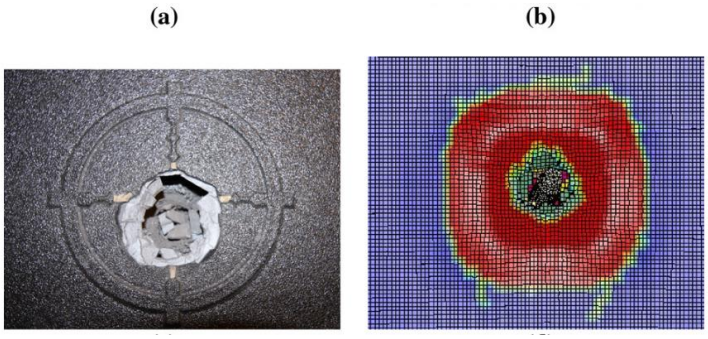

Figure 2-19: The front face of (a) an experimentally tested alumina armour plate in comparison to (b) FE prediction after an 877 m s^{-1} impact by a 7.62 mm AP M2 round [Reproduced from [66]***].***

2.8 BIO-MIMETIC DESIGN SOLUTIONS

Biological systems have been of interest to many different engineers who have noticed the remarkable functional properties achieved with the limited organic materials available to the environment through evolution [7,68–77]. From self-healing vascular networks embedded in

polymer composites to adaptive camouflage systems, there are many mechanisms and material designs that can be taken from nature and applied to engineering problems [78,79]. The meso-, micro- and nano-scale architecture of these natural materials allows for the use of mechanisms such as sub-component interlocking, crack blunting and increased surface contact to significantly increase functional properties, e.g. fracture toughness, in the biological material. Materials that are architected in such a way as to introduce interlocking and take advantage of these observed mechanisms are called topologically interlocking materials (TIMs) [80].

Of particular interest to the design of ceramic armour is the high fracture toughness and damage localisation achieved by nacre, the inner layer of mollusc shells. Nacre is comprised of aragonitic calcium carbonate (aragonite) platelets in a matrix of more ductile protein biopolymer layers in a ratio of 95:5 by volume [7]. While aragonite tested in isolation has a strain to failure of 0.1%, in nacre with the inclusion of a ductile interlayer strains of up to 1% have been measured, and some gastropod samples have exhibiting strain of up to 2% for similar biological systems [73]. This allows for much greater dissipation of energy and a fracture toughness of 8 MPa $m^{½}$, with some reports of this being more than two orders of magnitude greater than that of the base material [75]. With a modulus of 48-70 GPa and a tensile strength of 170 MPa, nacre itself is not to be considered a ballistic material, which is expected as it is limited to materials that can be grown organically and is adapted for much lower strain rate environment involving sea debris and not ballistic impacts [7]. However the improvements in the performance of nacre in comparison to its constituent parts show that it is worth exploring integrating aspects of its microstructure for adaption into ceramic armour systems using high-grade ceramics [17,81].

There are three functional elements of the nacre sub-structure that appear to impart these performance gains, the first of which is an interlocking platelet geometry. These platelets have an approximately hexagonal shape, ~8μm in diameter and ~0.4 μm in thickness, with a non-flat through thickness profile that allows for interlocking as the tiles slide past each other under tension (Figure 2-21). This observed "waviness" can reach amplitudes of up 200nm, i.e. almost half the thickness of a tile [82]. During tensile failure, nacre plastically yields through tiles first sliding over each other before a brief stiffening domain as the tiles are compressed laterally together and interlock before finally reaching failure (Figure 2-21).

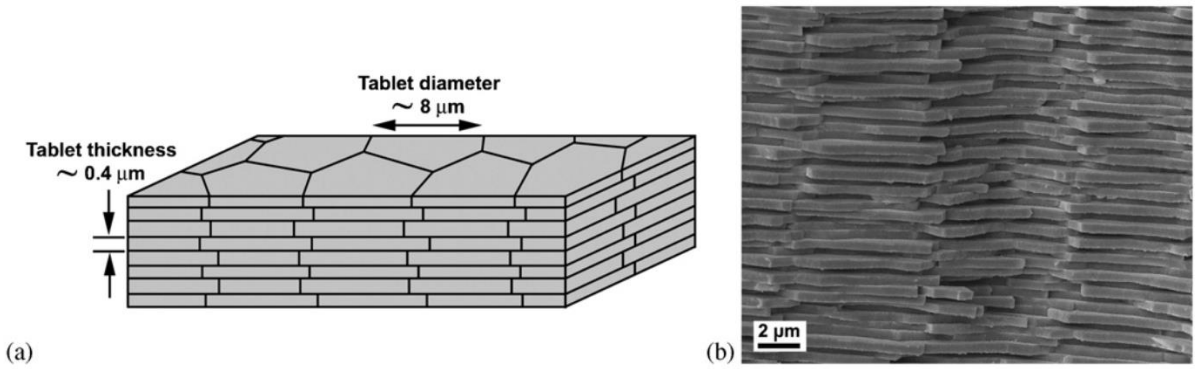

Figure 2-20: The mesoscale structure of nacre. (a) A schematic showing the arrangement of the interlocking platelets within nacre and their approximate dimensions and (b) an SEM image of a fracture surface cut through nacre showing the platelet structure in-situ [Reproduced from [68]***].***

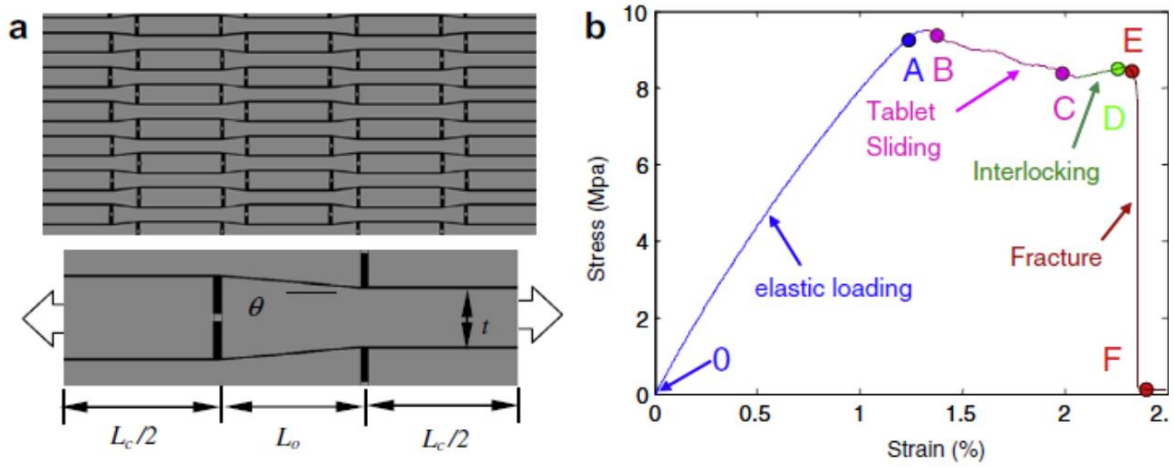

Figure 2-21: (a) A schematic of idealised nacreous platelets in cross-section showing the edge tapering that allows for interlocking [Reproduced from [70]***]. (b) The stress-strain response of nacre subject to tensile loading [Reproduced from*** [68]***].***

The second relevant observed substructure of nacre are nanoscale mineral bridges, called nanoasperities, between the platelets. These are believed to allow the tiles to interact before direct surface contact and also to act as a sacrificial element designed to break and further absorb energy just prior to the tiles beginning to move as well as adding surface roughness to increase friction at points of platelet contact [5]. The final relevant aspect of the nacre design is the inclusion of the ductile biopolymer that allows for adhesion between the platelets during sliding and greatly increases the tensile strain to failure compared to pure aragonite, i.e. from <0.002 to 0.0085 (Figure 2-22) [82].

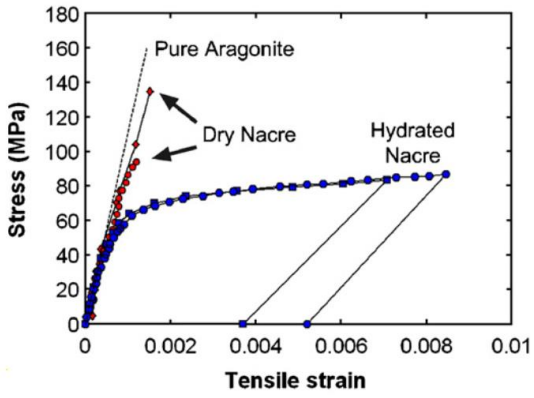

Figure 2-22: The stress-strain response of nacre in comparison to pure aragonite and a dehydrated sample [Reproduced from [68]***].***

Initial investigations into armour design inspired by nacres hierarchical structure have shown promise in the approach. For armour design the length scale is increased from the micrometre up to the millimetre, the aragonite is replaced by a ballistic grade ceramic such as SiC-N and the biopolymer proteins are replaced by an epoxy resin [9,83]. One such investigation used finite element analysis to simulate impact by a spherical impactor into armour designs made from aluminium with and without cohesive and interlocking, by a spherical impactor resulting in an almost 50% improvement in the reduction of the residual velocity (Figure 2-23) [9].

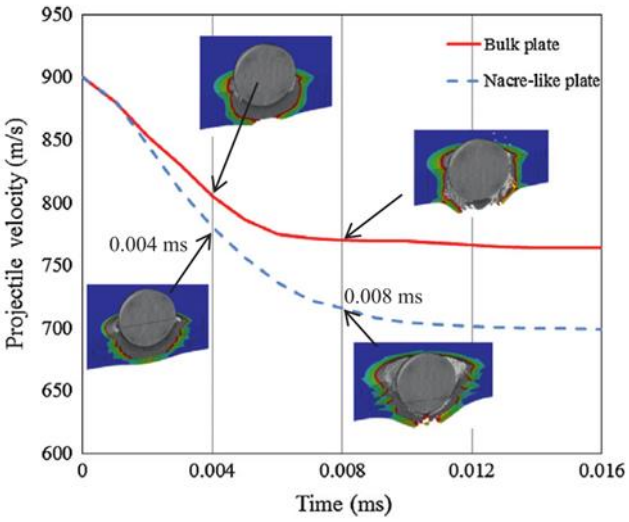

Figure 2-23: Time history of projectile velocity showing a 5.4 mm thick nacre-like plate out performing a bulk plate of aluminium (i.e. an equivalent thickness single layered system) [Reproduced from [9]***].***

It is not certain if this ballistic performance improvement due to simple nacre-inspired designs carries over to ceramic systems as the introduction of layers affects the dwell time, a phenomenon not present in the failure mode of aluminium. Other investigations into topological interlocking

during impact show tile pull-out occurring over the time scale of a ballistic interaction indicating the mechanism may have an effect during high-velocity impacts, a non-trivial finding given the increased strain-rate at much shortened time span over which a ballistic event occurs compared to impacts by sea debris ($10^{-6}s^{-1}$ vs $10^{-1}s^{-1}$ respectively) [5,84]. Simulations of a hexagonally-tiled interlocking plate with inter-layer cohesive have shown a localisation in the damage zone around the point of impact, compared to monolithic material, which may infer greater performance for tiled armours against multiple impacts (Figure 2-25).

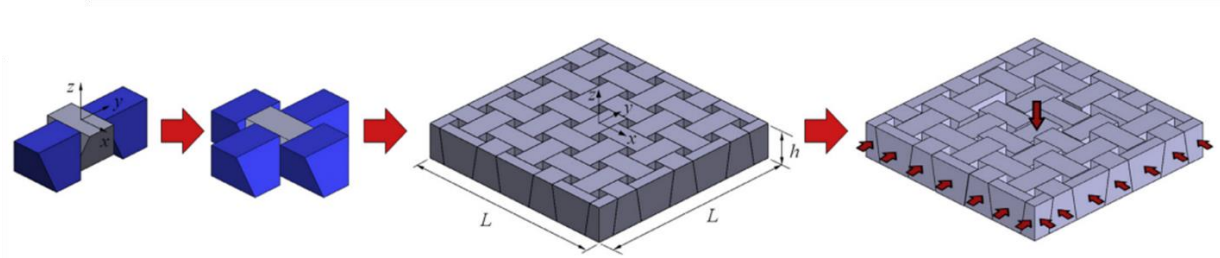

Figure 2-24: The construction of a "topologically interlocked" panel of tetrahedral tiles designed to interlock under loading [Reproduced from [85]***].***

Single-layer nacre-inspired ceramic designs with simpler interlocking architecture have also been shown to improve certain mechanical properties at the cost of others. In work by Mirkhalaf et al [85], a tiled panel of interlocking tetrahedral tiles was shown to absorb between 5 to 20 times more mechanical energy than a monolithic equivalent, although at the cost of a 75% decrease in overall strength (Figure 2-24). The trend of greater energy absorption from this design held for dynamic as well as quasi-static loading. It was observed that smaller numbers of tiles covering the same surface area (i.e. larger tiles) performed considerably better with a smaller degradation of stiffness and strength. The optimal angle for the sides of this tetrahedral tile shape is 5^{o} from the normal, relative to the flat top and bottom surfaces. In later experiments it was found that the mechanical response of the TIM could be controlled by varying the confinement conditions around the system [86].

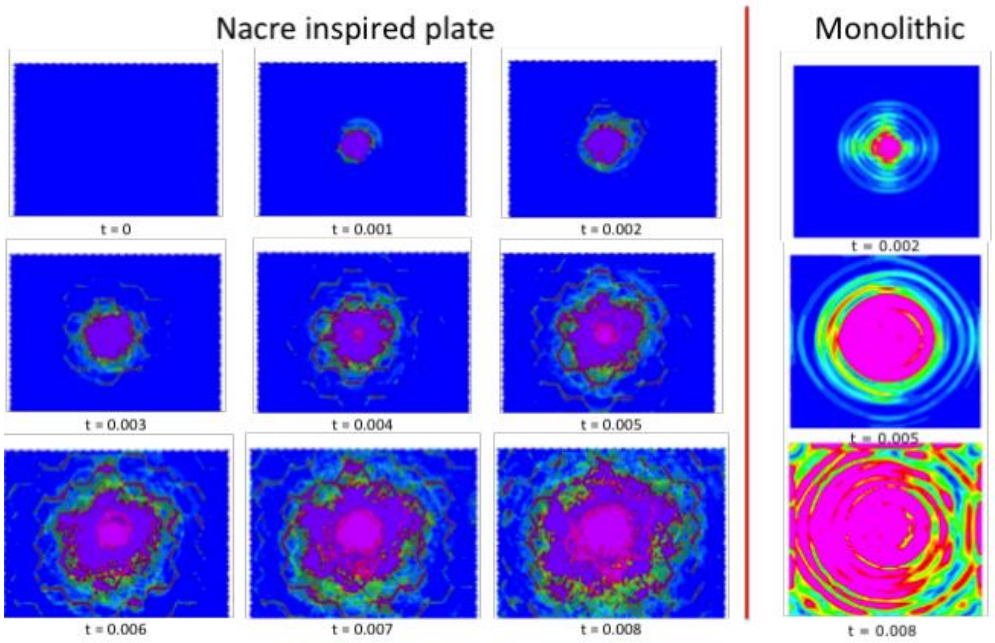

Figure 2-25: A comparison of the impact damage of a nacre-inspired and a monolithic armour system [Reproduced from [84]***].***

The ceramic manufacture techniques of the intricate shapes required to produce a bio-mimetic armour are not yet developed to a point that it is easily scalable to industrial production. The non-uniform through thickness can lead to variations in density due to uneven pressure application during sintering and requires specially crafted graphite dyes. However, ceramic manufacture techniques are rapidly improving such that these designs may be feasible in the future for use in functional armour once a working design has been developed. The simpler tile architecture shown in Figure 2-24 has a more achievable manufacturer process to scale, although only limited aspects of the key features of nacre are implemented.

3D printing of plastics, EDM (electric discharge) machining of metals and even planar assembly of ice structures have allowed for intricate and complex shapes to be investigated and have demonstrated the potential for topologically interlocking designs to increase the performance of their constituent materials. Although, as noted, it could more precisely be described as a method to fine-tune the specific material properties than providing a blanket all-purpose improvement [87–89].

The ability to control material parameters, combined with a greater understanding of the underlying fracture mechanics during ballistic impact and therefore of the relevant material properties, gives considerable promise to the idea that TIMs and biologically-inspired materials could provide the next generation of ballistic armours.

2.9 SUMMARY AND RESEARCH SCOPE

The behaviour of ceramics under impact at high strain rate are understood sufficiently well to be accurately modelled through finite element analysis [22,63,90–92]. Of the ceramics identified for use in ballistic armours, the focus of much of the current research is on alumina, silicon carbide and boron carbide [41,93,94]. However, certain behaviours such as amorphization of BC_4 at high strain rate is, as yet, beyond the scope of FE analysis [39,48]. In comparison, there has been considerable success in the simulation of high velocity impacts against alumina [22,52,91]. For this reason, alumina has been chosen as the primary material for the research presented in this thesis.

Most impact modelling on biologically inspired materials and TIM armour designs up to this point has focussed on single impacts at low and medium velocities (10 – 500 m s^{-1}) [9]. This leaves considerable space to explore the potential for optimising ballistic performance against high-velocity (<850 m s^{-1}) threats and achieving multi-hit capability with designs of this type. This research is motivated by the desire to expand on our current understanding of the design space for biologically inspired armours and create an armour based on these principles that is capable of NIJ IV ballistic performance [23] against a single impact as well as achieving multi-hit capability.

CHAPTER 3 – MODELLING VALIDATION

3.1 INTRODUCTION

The manufacture process of prototypes for ceramic armours can often be long and prohibitively expensive. Especially as the primary method of investigation into the ballistic performance of these armours is unavoidably destructive of the sample. The temporal and spatial resolution for post-analysis of these impact events is also a limiting factor in the understanding of the specific failure behaviour of the ceramic [1]. Finite element analysis (FEA) can prove a vital tool in overcoming these limitations.

For impact modelling, the most commonly applied form of FEA uses an explicit dynamic solver. "Dynamic" refers to the nature of the scenario being modelled, i.e. this is not a static or quasi-static test case and the time evolution of the model is highly relevant. Explicit analysis refers to a type of analysis in which nodal forces and accelerations are solved directly from one time step to the next, as opposed to an implicit analysis in which a single time step is iterated over until an equilibrium state is found [95].

The explicit dynamic solver chosen for this project was LS-DYNA ver. 7.1. This was chosen as it has a strong history of use in industry and an implementation of the Johnson-Holmquist 2 material model that has previously been identified as an appropriate tool to determine the behaviour of a ceramic target under impact (see Chapter 2, Section 1.6). LS-DYNA input files are written as a series of keywords to define the physics and initial conditions of the model, including material cards, contact rules, elements and nodes etc. When referred to in this thesis, keywords will be written in capitals and preceded by an asterisk. The specific meshing tools used in the creation of the geometry of the models in this research are LS Pre-Post and MSC Patran. A Python meshing script was also developed in order to mesh the geometries of the novel tile designs presented in Chapter 5.

At the outset of an investigation of this kind, it is necessary to first verify that the model is functional and mathematically correct, i.e. that no non-physical outcomes are observed. After this is complete, it is necessary to validate the model against available experimental data to determine that model is also physically correct. The first of these checks is the verification of the material model in a test environment, a mesh convergence test and boundary condition tests. As the complexity of the model builds towards a complete simulation, each step should be verified and

validated where possible to ensure the model corresponds to its physical counterpart as closely as is necessary for the research question.

3.2 VALIDATION OF THE JOHNSON-HOLMQUIST-2 CONSTITUTIVE MODEL

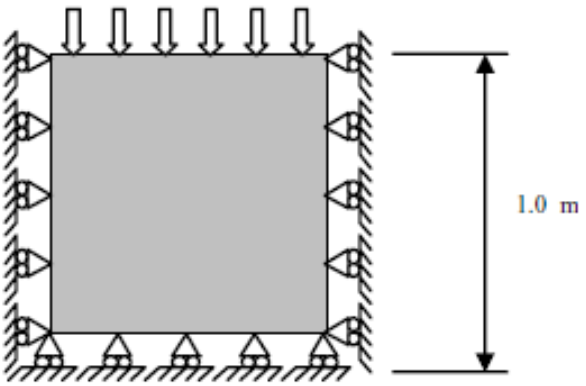

Figure 3-1: Boundary conditions for a diamond-press-like single element load case [Reproduced from [22]***].***

The first verification test is a replication of a simple single 1x1x1m cubic-element diamond-press-like load case as shown in Figure 3-1. This was done to confirm that the Johnson-Holmquist-2 (JH2) ceramic model, as implemented in LS-Dyna version R7.1 as *MAT_110_JOHNSON_HOLMQUIST_CERAMICS, behaves correctly and replicated initial modelling test work by Cronin et al [22], particularly for the stress-strain response and damage accumulation. The boundary conditions during this test on a single element were fully restrictive on the lower 4 nodes and restrictive in X and Y on the upper surface, note that in Figure 3-1 the z-axis is directly upwards. The top 4 nodes were then displaced using LS-DYNA *BOUNDARY_PRESCRIBED_MOTION keyword, in the negative z direction by 0.05m and then returned to the original co-ordinates.

The validation cases, shown in Figure 3-1 and Table 3-1, successively increase the complexity of the model to check each feature of the material model is functional. Case A, the first model, is the simplest application of the model and does not feature the damage accumulation discussed in chapter 2 that the JH-2 model is capable of simulating. In Figure 3-2, it can be seen that in this case the material transitions from an undamaged response curve (linear stress-strain relationship) to a fractured state with no retained strength. In case B, with non-zero values of D_1 and D_2, the ceramic accumulates damage as it undergoes plastic strain, leading to a gradual reduction in the effective stress of the element. Finally, in case C the parametric values B and M in Equation *(2-5)* are included which allow for the element to maintain some residual strength in a fully damaged

state. A close match of the results from Cronin has been made showing that the model has been implemented correctly for a simple single-element test case and can be developed further, building towards a complete model of ballistic impact (Figure 3-2). The stress-strain curves for each case is shown in Figure 3-3. In each case, the effect of the changing variables can be clearly seen. In Case A, for which the damage accumulation variables are zero and the fractured strength is also zero, it can be seen that relatively early failure occurs at a strain of ~0.013. In Case B, in which the damage variables are non-zero but fracture strength is zero, it can be seen that the ceramic softens before failure. Similarly, in Case C with both damage accumulation and a non-zero fracture strength, the higher fracture strength can be seen during the initial phase of unloading as can the damage accumulation phase as in Case B.

Table 3-1: The alumina material properties used for the single element validation of the JH-2 model [Reproduced from [22]***].***

	Case A	Case B	Case C
Density (kg/m^3)	3700	3700	3700
Shear Modulus (GPa)	90.16	90.16	90.16
Strength Constants			
A	0.93	0.93	0.93
B	0	0	0.31
C	0	0	0
M	0	0	0.6
N	0.6	0.6	0.6
Ref Strain Rate (EPSI)	1.0	1.0	1.0
Tensile Strength (GPa)	0.2	0.2	0.2
Normalized Fracture Strength	0	NA	NA
HEL (GPa)	2.79	2.79	2.79
HEL Pressure (GPa)	1.46	1.46	1.46
HEL Vol. Strain	0.01117	0.01117	0.01117
HEL Strength (GPa)	2.0	2.0	2.0
Damage Constants			
D1	0	0.005	0.005
D2	0	1	1.0
Equation of State			
K1 (GPa) (Bulk Modulus)	130.95	130.95	130.95
K2 (GPa)	0	0	0
K3 (GPa)	0	0	0
Beta	1.0	1.0	1.0

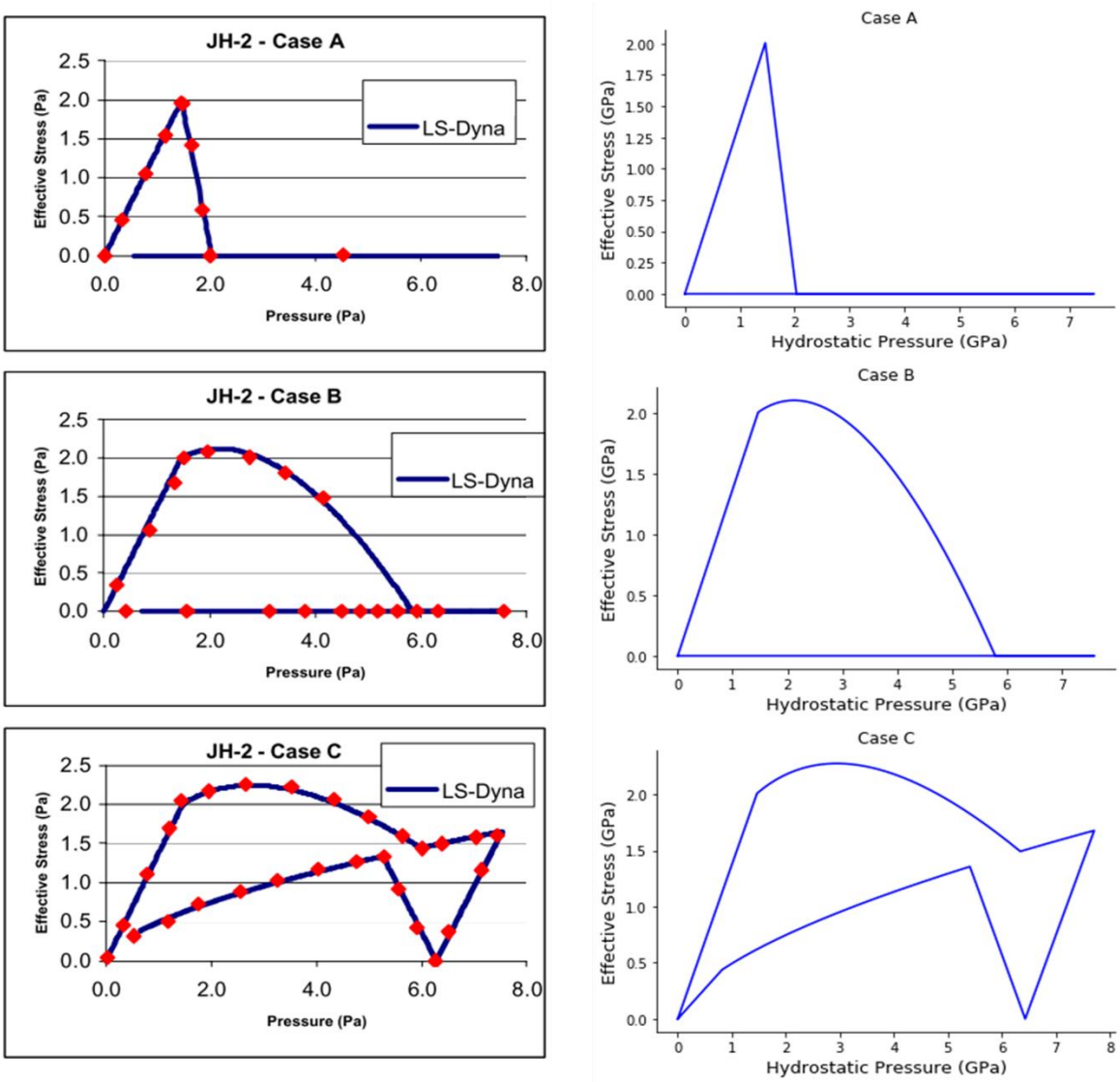

Figure 3-2: A comparison of the outputs (pressure vs effective stress) from Cronin et al [22] ***(left) and the replicated models performed during validation for this work (right). The properties of each case are described in Table 3-1.***

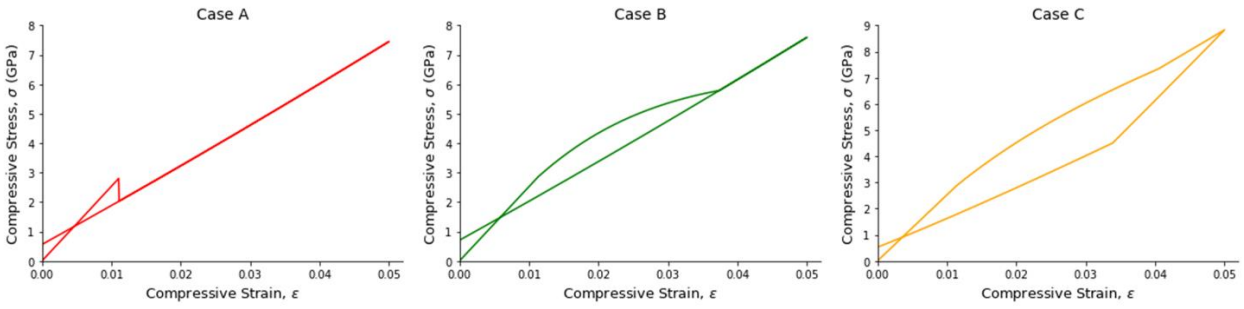

Figure 3-3: The compressive stress-strain responses of each test case illustrating the effect of damage accumulation and differences in fractured strength on the material response.

3.3 BUILDING THE IMPACT MODEL

After confirming the fundamental JH-2 model specific material parameters were behaving as expected, a series of convergence and validation steps were performed building up towards a full impact model for a monolithic ceramic tile. Alumina material properties were taken from Lundberg [96] and impactor properties taken from Dean [97]. The polycarbonate backing has properties taken from Dwivedi [98]. The initial convergence test is performed modelling an 8 mm spherical impactor striking an 8 mm thick alumina target with a length and width each of 100 mm (Figure 3-4).

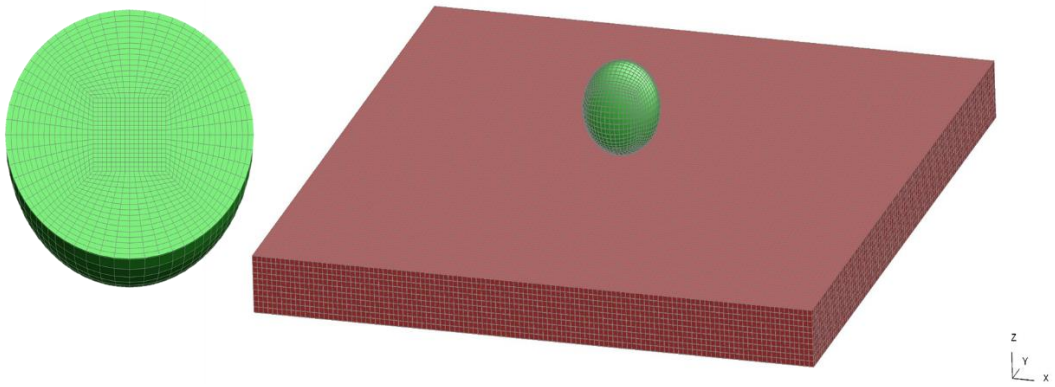

Figure 3-4: A cross section of the 8mm diameter spherical projectile (left) showing the internal mesh and the full simple monolithic ceramic impact model (right).

It is necessary to perform a mesh-sensitivity study, also called a convergence test, in order to choose an appropriate element size for the mesh i.e. an element size at which higher resolution does not continue to significantly change the results of the model for a chosen marker of performance. In this case, total energy of the projectile and target over time as well as residual velocity after impact are the chosen performance indicators for convergence. Given that the backing is in place as exclusively an inertial boundary condition, it can be assumed that a lower mesh density than that of the target ceramic and the projectile can be used without significantly affecting the results. Further, as the backing is restricted to exhibiting purely isotropic elastic behaviour, it is assumed that a mesh density between half and two-thirds that of the ceramic part is likely to be an acceptable trade-off between accuracy of response and computational efficiency [99]. The projectile requires a greater mesh density near the point of impact that can be reduced further away towards the back of the bullet. Convergence tests can often be iterative processes as changing the mesh density of one aspect of the model can change how it interacts with other parts. There is a trade-off in any FEA between accuracy of results with a finer mesh and the subsequent

increase in computational cost that accompanies a greater number of elements. With the geometries being chosen to be approximately analogous to a real-world impact on armour, the mesh of the ceramic layer was first investigated for mesh sensitivity.

The complexity of the model is built up in phases, leading up to the complete model described below in Section 3.6, to test each sub-component. The first stage of the convergence test was a simple impact model of a spherical hardened steel projectile impacting a thin plate of alumina (Al_2O_3), the material parameters for which are taken from Lundberg (Table 3-2) [52]. The ceramic target was 60mm x 60mm with a 5mm thickness and the projectile has a radius of 4mm. The target thickness was chosen to correspond to approximately half of the thickness of alumina armour systems that are known to prevent penetration; this would ensure penetration of the target whilst still providing resistance to the projectile [1]. The steel projectile, modelled using *MAT_024: PIECEWISE_LINEAR_PLASTICITY, has material properties that will be used for the 7.62 mm AP M2 round. These properties are density, modulus, Poisson's ratio and yield stress which are 7850kgm^{-3}, 206 GPa, 0.3 and 472 MPa respectively (Table 3-3) [97]. This pressure-independent elasto-plastic material model used defines the effective stress vs equivalent plastic strain of the material through a bilinear stress-strain curve. Strain rate dependence by defining load curves for further stress-strain responses at defined strain rates. However, there is no strain-rate dependence applied in the implementation in this work. The use of load curves can allow for more complicated stress-strain responses such as strain hardening.

When using a material model for the projectile that has no pressure dependence, there are limitations that must be addressed as many materials, including hardened steel, exhibit higher yield and flow stresses when subject to increased hydrostatic pressure [100]. This is particularly relevant for projectiles with ogival heads in which the curved shape can act, similarly to arches, to increase the hydrostatic pressure significantly within the ogival section of the projectile. Alongside the pointed tip serving to concentrate force on the target, this can produce significant performance increases for ogival projectiles over flat headed shapes. However, it has been observed by Gupta et al [65] that this effect is most prominent at impact velocities close to the transition velocity and that the shape can significantly affect the transition velocity itself with ogival-nosed projectiles penetrating at lower velocities compared to blunt-nosed projectiles, although for thicker ceramic plates a blunt projectile exhibits greater performance. However, the difference between the residual velocities of ogival, hemispherical and blunt nosed projectiles is significantly reduced at higher velocities dropping to <5% differences in residual velocities as compared to the >30% observed between transition velocities (Figure 3-5). Therefore, this pressure dependent material

model can be considered acceptable for this work as the impact conditions are chosen such that penetration occurs with significant residual velocity in order for clearly differentiated results to be produced.

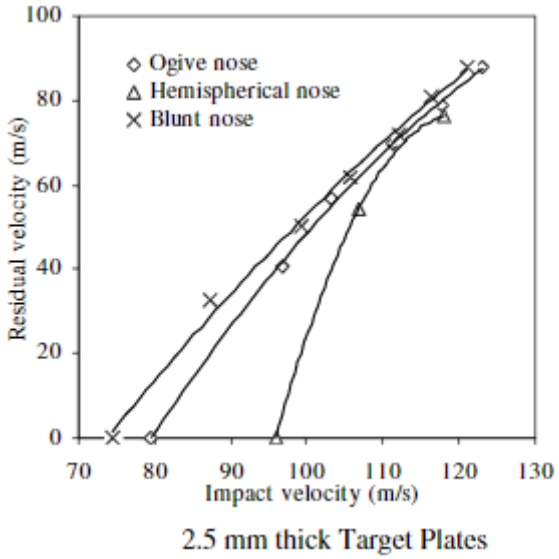

Figure 3-5: A graph showing that the differences in ballistic performance of projectiles of different shape reduces significantly at velocities greater than the transition velocity [Reproduced from [65]***]***

Table 3-2: Material parameters for alumina used in the JH2 constitutive model [52]***.***

Parameter	Notation	Al_2O_3
Density (kg/m^3)	ρ_0	3800
Bulk modulus (GPa)	K_1	200
Shear modulus (GPa)	G	135
Pressure coefficient (GPa)	K_2	0.0
Pressure coefficient (GPa)	K_3	0.0
Hugoniot elastic Limit (GPa)	HEL	8.3
Effective stress at HEL (GPa)	σ_{HEL}	5.9
Pressure at HEL (GPa)	p_{HEL}	4.37
Intact strength coefficient	A	0.989
Intact strength exponent	N	0.3755
Strain rate coefficient	C	0.0
Fracture strength coefficient	B	0.77
Fracture strength exponent	M	1.0
Maximum fracture strength (GPa)	S^f_{max}	2.95
Damage coefficient	D_1	0.01
Damage exponent	D_2	1.0
Bulking factor	β	1.0
Tensile strength (GPa)	T	0.13

Table 3-3: Material properties for the hardened steel core of the 7.62mm AP M2 round [66]**.**

Parameter	Notation	Bullet core
Density (kg/m$^{3)}$	ρ	7850
Elastic modulus (GPa)	E	210
Poisson's ratio	ν	0.33
Yield strength (GPa)	σ^Y	1.40
Tangent modulus (GPa)	E_t	15.0

Based on previous impact models of similar ballistic events in the literature [66,101], convergence was expected to occur around an element size of approximately 0.5 to 1mm, i.e. equivalent size to a hexahedral element with sides of 0.5 to 1mm. In the case of the target, the elements are perfectly cubic hexahedral elements whereas the projectile mesh is non-uniform. The spherical projectile was meshed using the MSC PATRAN primitive shape function that produces a hexahedral mesh structured around a central cube, this was chosen to maintain an aspect ratio close to 1:1 for the sphere. The element size for the sphere ranges from 0.25mm for the central elements up to 0.5mm for the elements on the outer surface.

The convergence test for this initial model started by taking a fixed mesh for the projectile and varying only the target mesh. The projectile was given an initial velocity, via the keyword *INITIAL_VELOCITY_NODE, of 900ms^{-1}. The total energy of the ceramic and projectile as well as the residual velocity of the projectile were used to determine when mesh convergence has occurred (Figure 3-6). Much of the energy absorbed by the ceramic target is dissipated through the production of, first a fracture conoid and later by the formation of radial and circumferential cracks. In the model, elements undergoing this behaviour will usually reach an element deletion criterion, in this case set by the material parameter FS (failure strain) and set as 1.5 on advice from industry collaborators. Note that this is not the strain at which the ceramic is in a fully damaged state which is determined by the parameters D_1, D_2 and T specific to the JH-2 model. The FS parameter dictates only element deletion after material damage is accumulated However, this deletion does lead to a drop in the total energy of the model and should be accounted for when analysing the energy balance of a set of results.

There are no constraints including in the model as the inertia of the ceramic and, in later models, backing is sufficient to support the target during impact. Contact between the impactor and the ceramic was implemented using CONTACT_ERODING_SURFACE_TO_SURFACE between parts. Both contacts used soft constraint option 2 as the contacts are between two parts of relatively dissimilar meshes. This is a segment-based contact, i.e. it detects penetration of segments

into each other rather than nodes to apply penalty forces. This is a more appropriate formulation for non-flat geometry, i.e. the projectile tip, as the nodes of angular elements could easily "miss" each other but this is not an issue for segments. SBOPT option 3 warped segment option with DEPTH option 5 is used for both contacts which checks for both surface and edge-to-edge penetrations. Edge-to-edge penetration is unlikely to occur on initial impact of the projectile with a flat ceramic surface but may occur later after deformation of the mesh or occur with non-flat geometries in later simulations.

In the simple case it is apparent that changes in these three outputs flattens out around 1mm element size and there is no significant change or gradient around 0.5mm element size (Figure 3-6). This suggests that an element size for the target of between 0.5mm and 1mm is sufficient to capture the behaviour under impact. Although it is first necessary to confirm this by looking at the convergence for both the projectile (progressing to a projectile representative of the AP M2 round instead of a sphere) and the backing.

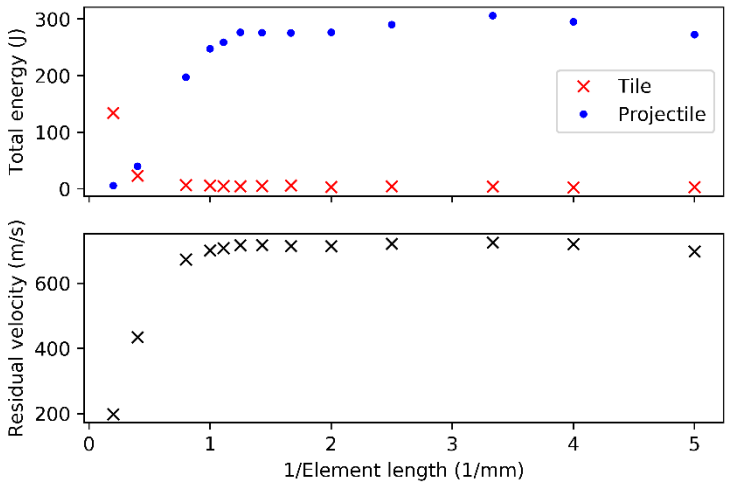

Figure 3-6: The convergence test for the ceramic tile mesh against a spherical projectile showing the total energy for the tile and projectile parts at the end of the run and the residual velocity of the projectile.

3.4 7.62MM AP M2 PROJECTILE MESH AND CONVERGENCE

With a baseline of convergence established for the mesh of the ceramic tile, the projectile geometry was changed from a simple spherical impactor to a geometry representative of the core of a 7.62mm AP M2 round (Figure 3-7). The full impact model simulates the impact of a 7.62mm AP M2 round travelling at 875ms^{-1} against an alumina strike-plate with width, length and thickness of 300mm, 250mm and 10.5mm respectively, to match modern ceramic armour insert sizes [11]. The

brass jacket and lead filler are omitted from this model and only the hardened steel core is included, with material properties given in Table 3-3 and taken from Dean et al [97]. The brass and lead components of the projectile are omitted in this model in order to simplify the projectile behaviour for these models and because these softer components, in comparison to the steel core, are rapidly eroded on impact and considered to minimally effect performance against a material with sufficiently high hardness, such as a ballistic-grade ceramic, for the purposes of optimising a ceramic armour design for this research [102]. Further work could include these components and increase the accuracy of the modelling of the specific projectile response. The diameter for this projectile is 6.17mm, the total length is 27.4mm with the ogive having a calibre-radius-head of 3.0 [55].

This mesh was created using MSC PATRAN via creating a 2D surface mesh and then using the "sweep" function to create the 3D elements around the central axis. The shaft mesh is entirely constituted of hexahedral elements whereas the ogival mesh is a combination of both hexahedral and tetrahedral elements. This requires the use of the *ESORT keyword in LS-DYNA to automatically apply an alternative single integration point element formulation for those tetrahedral elements. The mesh was created with a one-way bias such that the element length was finest at the tip of the projectile and gradually increased to a third of the mesh density at the rear.

Figure 3-7: Cross-section of the mesh of the model of the core of a 7.62mm AP M2.

As shown in Figure 3-8, the residual velocity of the projectile is stable above the 0.66mm length scale. The curve appears to have plateaued by the 0.33mm element length model and this mesh is carried forward into all future models. A small number of extra models with element lengths between 0.66mm and 0.33mm may show that a coarser mesh still captures the projectile behaviour with sufficient accuracy however, given that the change in total number of elements would be minimal relative to the number of elements in the full model, i.e. including the target and backing meshes, these further tests were not run and the 0.33mm element length projectile mesh was chosen as an acceptable mesh density.

In early testing of the model, a sensitivity was found with the initial proximity of the of the projectile to the target surface. Initially, this gap was 0.001 mm but was later increased to 0.1mm

for the final convergence studies and for all future models. The cause of this sensitivity is likely due to the time step of the model (~5 x 10^{-9} s) being greater than the time taken for the tip of projectile to move from its starting location to penetration of the target.

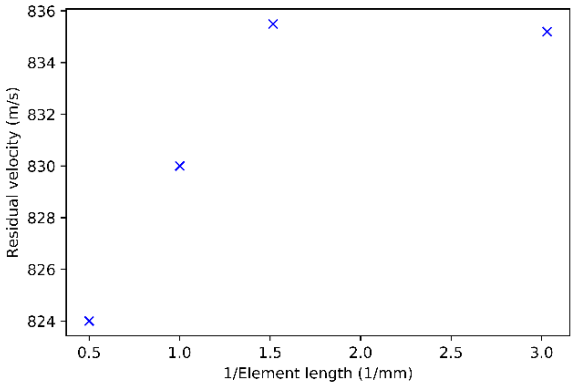

Figure 3-8: Convergence test showing residual velocity of the projectile after penetration for a range of element sizes. The representative element length is that of the outside length of the element at the tip of the ogive. Note that the x-axis is the inverse of the element length.

To determine the projectile model was behaving correctly, an impact test was performed against a flat rigid target for both the ogival-nosed projectile shown in Figure 3-7 as well as a flat-faced cylindrical projectile of the same dimensions as the shaft of the 7.62mm APM2 core model, i.e. a diameter of 6.17 mm and a length of 20.5 mm. These models were tested to check for reasonable deformation behaviour as well as a reasonable numerical response in terms of the impact pressure generated at the front of the projectile.

The analytical solution for the maximum contact pressure generated by a cylindrical projectile impacting a rigid surface can be approximated by

$$P \approx \rho c V_0 \qquad (3\text{-}1)$$

where ρ is the density of the projectile material, c is the wave speed in the material and V_0 is the projectile velocity [35].

Using the material properties from Table 3-3, this suggests a maximum initial contact pressure of 35.5 GPa. The expected deformation is as illustrated in Lundberg [33], i.e. radial flow in the front region of the projectile (Figure 2-9). As can be seen in Figure 3-9 and Figure 3-10, the cylindrical projectile shows a close match to the expected maximum contact pressure (33.26 GPa) and both projectiles exhibit radial deformation upon impact as expected. This shows that this material model is suitable for use in this finite element study.

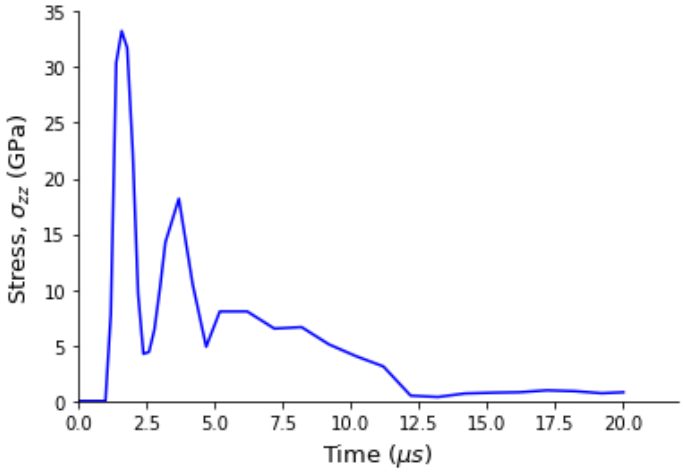

Figure 3-9: The time-evolution of the direct stress in the z-direction (i.e. normal to the impact surface) for a single element on the front face of the flat cylindrical projectile impacting at 875 ms^{-1} against a rigid target.

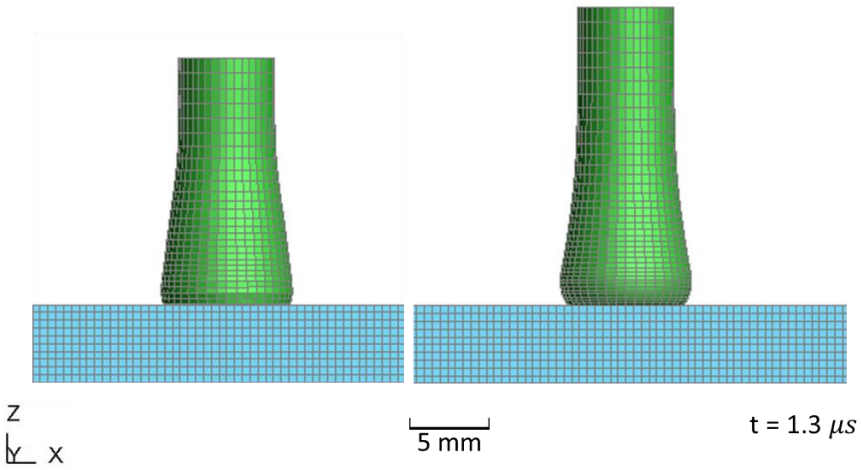

Figure 3-10: A flat-faced cylindrical target (left) and a 7.62 mm AP M2 core model (right) 1.4 µs after impact showing radial deformation.

3.5 POLYCARBONATE BACKING

Much of the available experimental ballistic data conducted with ceramics is performed with a polycarbonate rod as backing with the depth of penetration into the rod acting as the performance indicator for the test armour [103]. This also serves the purpose of including an inertial constraint to the armour and allows a greater build-up of bulk pressure during the impact, generally leading to greater ballistic performance and more accurately recreating the conditions of armour use in theatre when it is backed by some form of absorber layer such as Kevlar. Adding this backing layer to the model required both a convergence test and a thickness study to determine the appropriate

thickness of backing. The material properties for the polycarbonate are taken from Dwivedi [98] and are shown in Table 3-4.

Table 3-4: Polycarbonate material properties from Dwivedi [98]**.**

Parameter	Notation	Polycarbonate
Density (kg/m$^{3)}$	ρ	1197.75
Modulus of Elasticity (GPa)	E	2.59
Poisson's Ratio	ν	0.3
Bulk Modulus (GPa)	K	432

As a fully accurate model of polycarbonate penetration was beyond the scope of what was necessary for this model, the backing was modelled using *MAT_001_ELASTIC, a simple isotropic elastic material model. Only model contact between the backing and the target ceramic was modelled, i.e. no contact was added between the projectile and the backing such that, after penetration of the tile, the residual velocity of the projectile would not be affected by the backing but would instead level off. The residual velocity after target penetration is compared with experimental data from post-impact depth of penetration tests in Section 3.6.

Segment based contact using AUTOMATIC_SURFACE_TO_SURFACE was used between the ceramic and the backing with the same secondary card options as for the projectile-to-ceramic contact. It may not be necessary to check for edge-to-edge penetration for ceramic to backing contact as they are flat, parallel surfaces however this has been used as it may be necessary in future non-flat armour geometries to ensure comparisons can be made.

The backing was 20mm thick for the convergence test with the length and width matching the target, i.e. 60x60mm (Figure 3-11). A gap of 0.001mm was left between the backing and the tile to minimise future contact issues with the knowledge of some of the curved surfaces to be modelled later in the study. As can be seen in Figure 3-12, the backing absorbs a steady amount of energy after a 2mm element size although there is a slight outlier at 1mm element length. The deviation is not significant in the context of the backing merely acting as an inertial constraint to provide support to the ceramic itself, i.e. that it does not have to accurately model the behaviour of a polycarbonate backing except insofar as it provides support to the tile. For this reason, a 1- or 2-mm element length scale is appropriate for the backing.

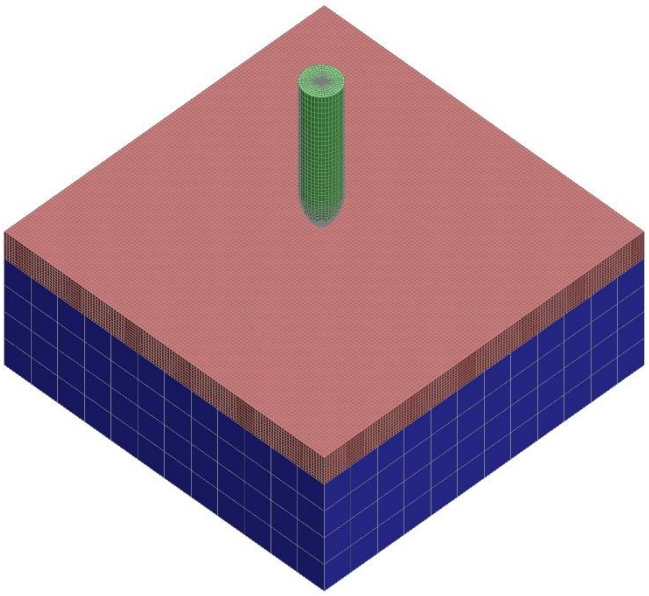

Figure 3-11: The model used in the mesh convergence test for the 20mm thick backing layer (blue) with a coarse mesh of 2x2x2 mm elements. The ceramic target geometry is 60x60x5 mm.

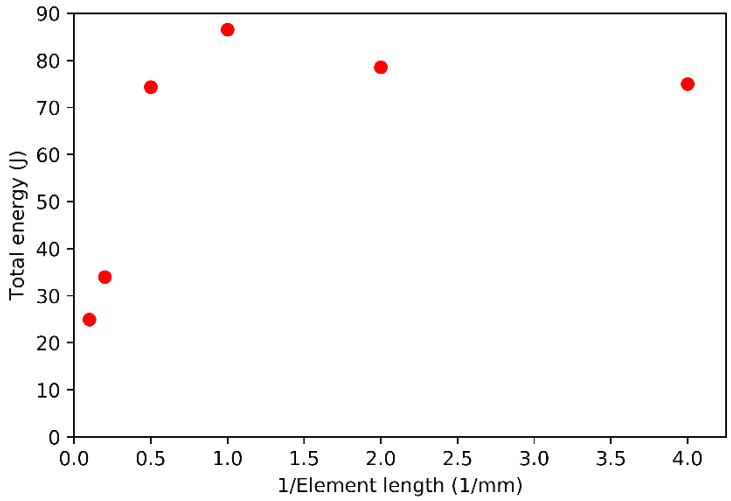

Figure 3-12: Backing convergence test showing the total energy absorbed by the backing as function of 1/element size.

With the length scale established, an appropriate thickness of backing needs to be chosen with a trade-off between greater thicknesses offering more support, with the experimental set-ups from DoP tests acting as quasi-infinite backings, versus the computational cost of incorporating extra elements into the model. The element size was chosen to be at least 1x1mm in the x- and y-directions but could be increased in the through-thickness z-direction provided there were at minimum three elements through-thickness and the aspect ratio was kept below 10:1 based on guidelines published by the Aerospace Working Group [99]. For this reason, an aspect ratio of 2:1

was chosen such that the element size was 1x1x2mm for all models in the thickness study shown in Figure 3-13. This reduces run-time by as much as 30% depending on the thickness of the backing. There is a small effect on the final result of the model (e.g. 745.9ms^{-1} vs 742.5ms^{-1} for 1x1x2mm and 1x1x1mm respectively for two models with 10mm backing). This effect was considered negligible compared to the benefit in reduced run-time for this work.

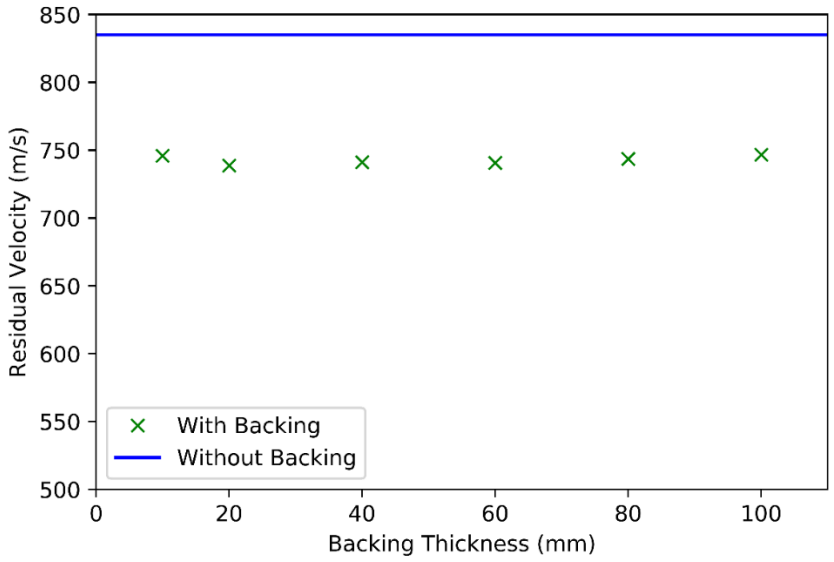

Figure 3-13: The effect of backing thickness on residual velocity compared to the same model without backing.

The addition of a backing layer increases ballistic performance in these models considerably, e.g. 753ms^{-1} vs 835 ms^{-1} residual velocity after an 875ms^{-1} impact for two otherwise comparable models with the addition of a 20mm polycarbonate backing. The model geometry for the backing thickness study was expanded from that used in the backing convergences tests to 200x200mm in length and width. There is very minimal difference due to increasing the thickness of the backing although a significant difference with the inclusion of a backing compared to no backing (Figure 3-13).

The backing thickness for experimental DoP testing is 300mm, however it was deemed unnecessary to model the full thickness given that increasing backing thickness shows minimal change to energy absorbed during impact and increases computational run-time. The negligible effect of increased backing thickness is likely due to an effect analogous to dwell in the ceramic itself. The most important time period during penetration, in terms of fracture mechanics and ballistic performance, is the time it takes for the initial compressive shockwave to travel through the ceramic, be reflected from the backing surface and then reach the impact point again. As long

as the backing is sufficiently thick that any shockwave transmitted across the ceramic-backing interface is not reflected back to the ceramic prior to the end of the ballistic event, any further thickness will have little to no effect on ballistic performance [104]. For this reason, a backing of 20mm thickness was chosen for the final baseline.

As far as this applies to this model, that would mean that a backing of at minimum half the thickness of the target ceramic is necessary but, to minimise edge effects due to the backing, a thickness of twice the maximum thickness is used, i.e. 20mm thickness as the later tiled models will be a maximum thickness of 10.5mm total thickness to compare to areal-densities found in use in modern military armour today. This is in-line with the parametric study results shown in Figure 3-13. It is worth note that experimentally greater thicknesses of polycarbonate are necessary as they are required to fully stop and contain the projectile in order to obtain a measurable result.

3.6 FINAL BASELINE GEOMETRY AND MESH

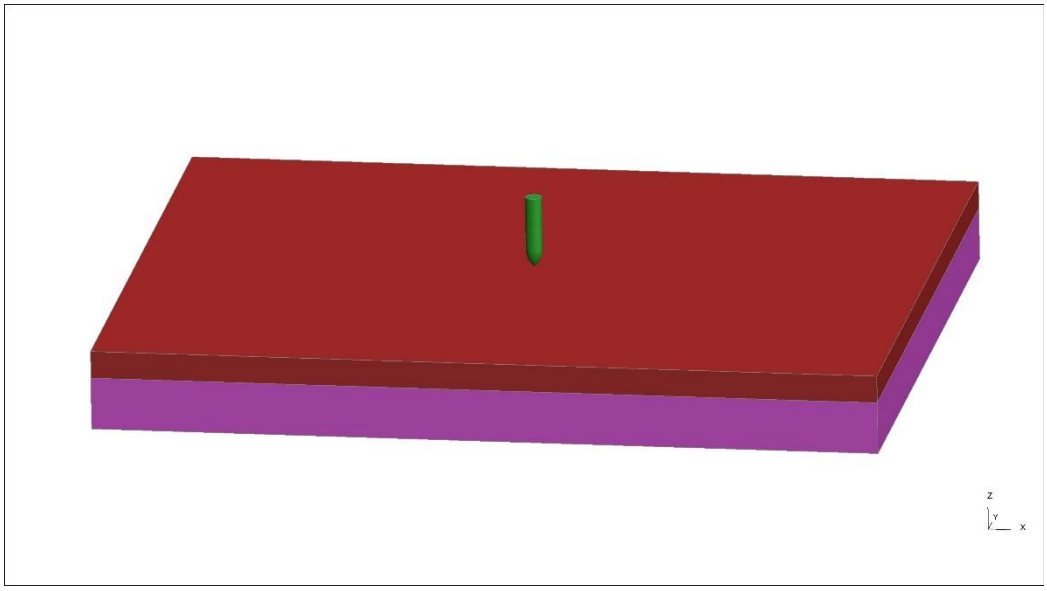

Figure 3-14: The final baseline monolithic impact model of a 7.62mm AP M2 round striking a 300mm x 250mm x 5.17 mm alumina strike plate backed by a 20mm thick simple linear elastic model of polycarbonate.

The above convergence, mesh and geometry studies were used to inform the decision on the final geometry and mesh of the baseline model i.e. the monolithic ceramic impact model from which comparisons to experimental data and, subsequently, comparisons with novel bio-mimetic geometries and designs could be made (Figure 3-14). The thickness of the baseline model is 10.5mm to match the areal-density of existing ceramic front-plates [21]. The length and width of

the ceramic tile and the backing beneath it are 300mm and 250mm respectively for the same reason. The chosen polycarbonate backing is 20mm thick.

The sides of the elements are 0.5 mm in length with the exception of the z-axis (i.e. through-thickness) which is 0.52 mm. The backing elements are meshed with 1x1x2mm elements as there is less complex behaviour to be modelled by the backing as compared to the ceramic. There is a 0.001 mm gap left between the ceramic and backing to ensure an accurate comparison with future non-flat geometries in which this would be necessary to ensure no initial penetration between the parts, which may have led to contact issues.

Contact between the projectile and the ceramic is managed by the ERODING_SURFACE_TO_SURFACE formulation between a coat of segments on the upper surface of the tile, the slave side, and the entire part ID of the projectile, the master side. As the ceramic part is subject to element deletion throughout the model run this "ERODING" contact type ensures the contact surface is updated as the initial exterior contact elements are deleted [95]. As no element deletion criteria are in place for the backing, an AUTOMATIC_SURFACE_TO_SURFACE contact type was used between segments coating the lower surface of the ceramic part and the upper surface of the backing part. As stated previously, there is no contact between the backing and the projectile such that residual velocity after penetration of the ceramic can be used as the measure of ballistic performance. In order to be able to use residual velocity as a measure of performance, it is necessary to limit the thickness of the armour to ensure penetration of the target occurs. This allows the effects of changing the various geometrical and material components to be looked at in terms of comparative studies with a measurable output. In practice, these armours function in the context of a ceramic-composite system such that it is not the performance of the ceramic fore-plate in isolation that determines the NIJ rating.

There are several checks that can be performed to determine if the model is an accurate representation of the real system it is simulating. The first is a visual check to determine if the behaviour of the model approximately matches the expected behaviour. This includes looking for excessive element deformation and other clearly non-physical occurrences. The primary method, however, is to check that the crack propagation and damage mechanisms displayed are consistent with the expected ceramic behaviour as these are the main effects that the ceramic model is aiming to replicate. Figure 3-15 shows the model displaying radial cracking that closely matches the damage patterns on a post-impact ceramic armour. Also seen in the model on the boundaries of

the tile are the reflected compressive shockwaves, now tensile, causing damage to accumulate on the edges.

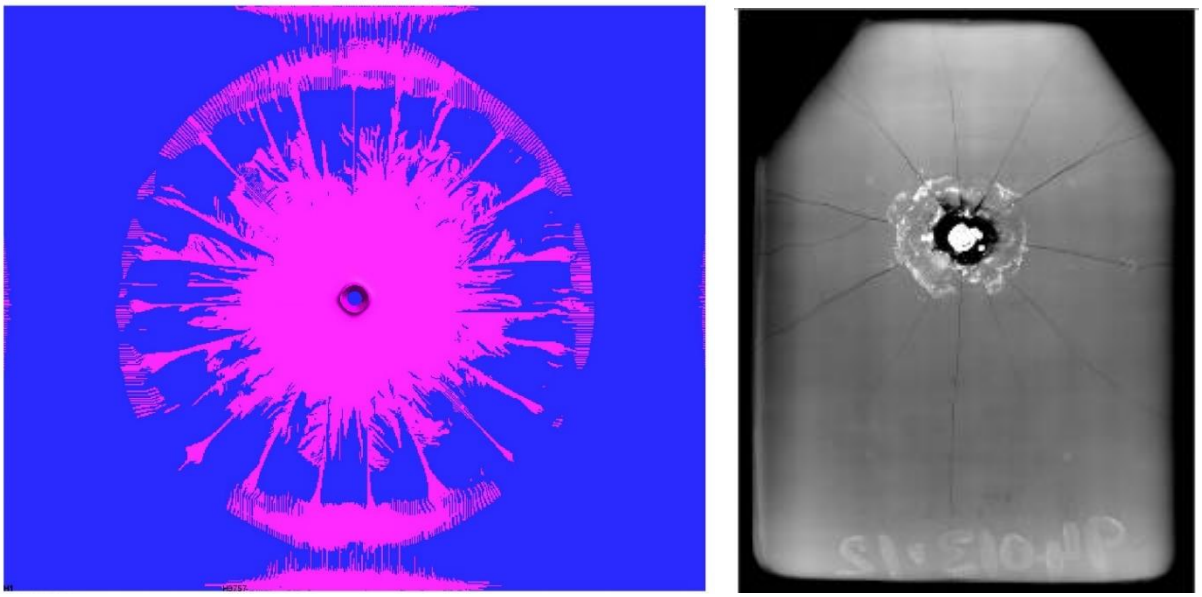

Figure 3-15: (Left) A top down view of the baseline monolithic alumina tile 18 μs after impact with full damaged (D=1) elements highlighted in pink. (Right) A SiC hard armour plate after impact showing a similar radial crack pattern [Reproduced from [27]***].***

3.7 VALIDATING AGAINST EXPERIMENTAL DATA

After performing these convergence tests and verifying the model to ensure it is working correctly, it is necessary to then validate the model against appropriate experimental data. The material properties used up to this point are taken from Lundberg [105]. The elastic moduli K and G were deduced from the Poisson's ratio, measured density and longitudinal sound speed. Compressive strengths were measured by split Hopkinson pressure bar experiments and further values taken from compressive testing by Nicholas [106]. The six parameters A, N, B, M, D_1 and D_2 within the JH-2 model that are not directly measurable were derived in Lundberg from these sources. A and N refer to parameters relevant to the intact strength of the ceramic, B and M are parameters relevant to the fractured strength whilst D_1 and D_2 affect the plastic strain to failure of the ceramic and therefore the transition of the ceramic strength from intact to fractured values. The normalised fracture strength, $S^f{}_{max}$, was determined experimentally on a post-failure ceramic sample, also in Lundberg [105].

Experimental data was provided by DSTL for depth of penetration (DoP) testing of the 7.62 mm M2 AP round against three thicknesses of commercially available pressureless sintered alumina: 5.17mm, 6.12mm and 7.14mm. These experiments quantify ballistic performance in terms of the

depth of penetration into a polycarbonate rod clamped in place behind an alumina (Al_2O_3) target. In order to use this data to verify the ballistic simulations in this work, it is necessary to translate that DoP data into an estimated residual velocity after impact. To do this, several key assumptions were made, the justification for which is laid out as follows. The primary assumption is that the only damage mechanism for absorption of kinetic energy by the polycarbonate backing is cavitation energy and that cavitation energy goes linearly with the square of the velocity [107]. As cavitation energy is also directly proportional to the length of the cavitated volume, the relationship between the depth of penetration, H, and the velocity of the projectile, *v*, is

$$H \propto k\, v^2 \qquad (3\text{-}2)$$

where k is a constant for a given projectile of some fixed mass.

It is also assumed that that the deformation of the projectile during impact would have minimal effect on the subsequent penetration of the backing, this may not hold on near-interface defeat impacts in which the projectile was almost, but not quite, prevented from penetrating and as such would have undergone significant deformation away from an ogival shape. However, as the verification data is of residual velocities that are in the range of 30-60% of the impact velocity, the projectile deformation between impacts can be considered comparable. As it is being compared to DoP data for direct polycarbonate impacts in which no prior deformation of the projectile will have occurred it should be noted that the calculated residual velocities will be slight underestimates. For a more accurate comparative tool it would be necessary to fire post-ceramic-impact projectiles into polycarbonate at a range of velocities to determine the depth of penetration relation for deformed projectiles. However, for the purposes of this work, the DoP to impact velocity relation for non-deformed projectiles is considered sufficient for the purposes of model validation.

The final necessary condition for the data to be useful in verifying the baseline model is that the impacts are occurring well above the transition velocity for the ceramic, such that the impact and residual velocities vary linearly with respect to each other. Around the transition velocity, the behaviour of the ceramic is much more difficult to predict as it subject to the local conditions of the ceramic around the impact site, such as voids, defects and microcracks [52,108]. Significantly above and below the transition velocity, the statistical variation in these defects is much less likely to produce large variations in results between samples and therefore Equation *(3-2)* will not hold for low residual velocities or for low depths of penetration. However, this is not the case for any of the three thicknesses of ceramic used in the ballistic experiments as the mean calculated residual

velocity remains higher than that observed of impacts in the range of transition velocities, i.e. >20% of the impact velocity [52]. This is explored in more depth in Chapter 4.

Experiments conducted by Weiss et al impacting a polycarbonate rod with a 7.62mm AP projectile over a range of impact velocities shows that the assumptions leading to the form of Equation *(3-2)* hold true and that for this specific projectile against polycarbonate the equation becomes

$$H = \frac{v^2}{2660}\ [mm]. \qquad (3\text{-}3)$$

The fit for this curve against experimental data is shown in Figure 3-16. This relation holds for a non-blunted projectile into the polycarbonate, whereas in DoP tests into polycarbonate behind a ceramic plate the projectile will have been deformed and possibly taken off its central axis resulting in lower penetration at the same velocity. Therefore, using this relation to estimate residual velocity from DoP data for ballistic impacts through ceramic front plates will likely result in an underestimate of velocity. Given the much lower Young's modulus and plastic yield strength of the polycarbonate in comparison to the hard steel core of the 7.62 mm AP M2 round and assuming the projectile is not subject to complete fracture, the difference may be minimal and will not be considered for the purposes of material parameter calibration. However, for future work it may of interest to investigate further. Using this method, the residual velocity of the projectile after ceramic impact was deduced from the DoP data and is presented in Table 3-5.

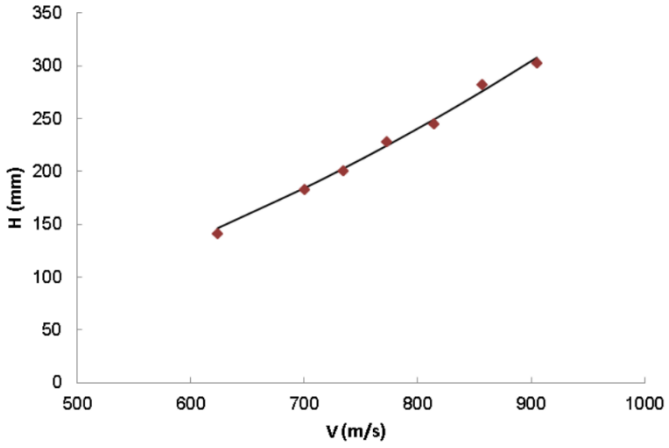

Figure 3-16: Final depth of penetration of a 7.62mm AP round impacting a polycarbonate rod as a function of impact velocity. The line of best fit shown is of the form of Equation (3-2) [Reproduced from [107]***].***

In order to confirm the reliability of the simulated models the results should closely match the experimental data. To check this, the developed model (Figure 3-14) was adapted to match the thicknesses of the experimental data and the residual velocity from the model compared to that of

the ballistic experiments. A concern when comparing FEA simulations against experimental ballistic data is that the boundary conditions can cause significant differences in outcomes. In the experimental procedures the target was clamped into position but was sufficiently large that the clamping served only to manage the post-impact behaviour of the ceramic and not to affect ballistic performance. This assumption is made on the basis that the impact event is over within the time taken for the impact stress wave to have reached the nearest boundary and returned to the point of impact. Any boundary constraints could provide resistance to flexural failure, a common failure mode in unsupported ceramics due to their low tensile strength [11]. The wave speed for the ceramic is 7160 ms^{-1} and the smallest lateral distance is 125mm. This gives a total reflection time of 34.8 μs. The total time of the impact event for a projectile impact against a 5.17 mm ceramic target is ~23 μs (see Figure 4-2 in the next chapter). This suggests that, while there may be a small period at the end of the impact event for thicker targets (>8 mm) in which ballistic behaviour is affected, the applied boundary conditions (i.e. free edges) are sufficient for this work. The requirement for the backing is that the thickness should be sufficient to allow the dwell period to pass and the reflected incident impact stress wave to interact with the interface between ceramic and backing fully prior to any return reflections from the backing backface. As the polycarbonate has a much lower wave speed (1470 ms^{-1}) than that of the ceramic, this suggests a minimum viable thickness of 2.1 mm for a 5.17 mm thick ceramic target. As shown in Figure 3-13, simulations including backing thicknesses greater than or equal to 10 mm show minimal effect on residual velocity with increasing thickness. This suggests that the 20 mm backing used is sufficient to avoid errors due to differences in the boundary conditions between experimental and simulated impacts while keeping computational run time to a reasonable level.

The results for these models in comparison to the experimental data is shown in Table 3-5. This table shows a poor match between experimental and simulated results, likely as a result of the much higher strain rates occurring in the modelled ballistic impacts compared to the experiments from which the initial material parameters were obtained.

Table 3-5: Residual velocity data for a sintered alumina target calculated from depth of penetration tests provided by DSTL compared to data from FEA using material parameters from Lundberg [105]**.**

Material	***Thickness (mm)***	***Residual Velocity (ms^{-1})***	
		Experimental	**Simulated**
A commercially available pressureless sintered alumina	5.17	556.2 (±35.1)	746.9
	6.12	452.2 (±59.8)	729.6
	7.14	292.5 (±35.9)	712.5

As a result of the lack of correlation with the initial literature-based data, it was necessary to revisit the parameters used, especially those which were deduced and not directly derived experimentally, i.e. A, N, B, M, D_1 and D_2. A parametric study was undertaken to calibrate these model parameters to better match the experimental data using the models developed for validation, i.e. of ballistic impacts on three ceramic thickness of 5.17 mm, 6.12 mm and 7.14 mm. Initially, a brief parametric study into the effect of changing each of these six variables individually was undertaken. The available experimental data plotted as thickness versus residual velocity forms a straight line, the y-intercept and gradient of this line were used as the comparative values used to calibrate these parameters from the results of this parametric study. It is worth noting that the intercept for the experimental data is higher than the impact velocity showing that relationship does not continue to approximate a straight line outside of the range of thicknesses spanned by these data points. As this assumed linear relationship is only for this material property validation, in which all thicknesses are within the range for which this relationship holds, it is considered to be an acceptable simplification in this case.

Although parameters A, D_1 and D_2 are potential calibration variables, they were left out of the final material study as, although they do not correspond directly to measurable physical properties, they do most closely relate to them. D_1 and D_2 are used in conjunction with the in-situ pressure and tensile strength to determine the strain to failure for the ceramic. As A is the coefficient for the intact strength of the ceramic, any changes to it are equivalent to changing the given maximum intact strength away from the known measured value, albeit within the constitutive equations rather than within the inputted parameters. As the effective stress of the ceramic is measurable experimentally, A is therefore considered an immutable material parameter. This leaves B, N and M as the remaining calibration variables and reduces the scope of the material study to a more reasonable range of possible values. From Table 3-2, the values of the variables B, N and M from

Lundberg [105] are 0.77, 0.3775 and 1.0 respectively. As the strain-rate coefficient for this material model is 0, the relevant equations from the JH-2 model featuring these parameters become

$$\sigma_i^* = A\,(P^* + T^*)^N \tag{3-4}$$

for the normalised intact strength and

$$\sigma_f^* = B\,(P^*)^M \tag{3-5}$$

for the normalised fractured strength. The curve described by Equation *(3-5)* is also limited by a maximum fracture strength obtained experimentally.

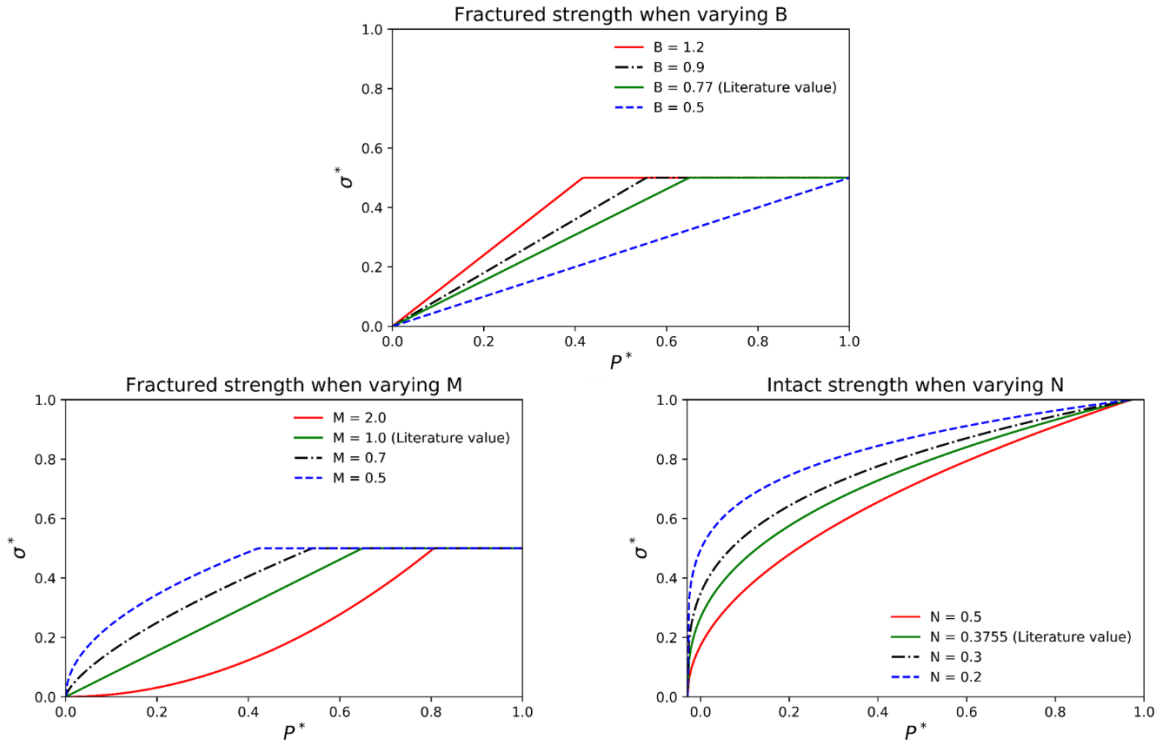

Figure 3-17: These graphs illustrate the change in the effective strength-pressure response for the fractured and intact ceramic equations of state as B, M and N (the three variables used to "tune" the material model) are varied.

As the initial values for these parameters underestimated the ballistic performance, the model needs to be slightly changed to be stronger in some aspect of its response to impact. This can be achieved by reducing N and M or by increasing B as illustrated in Figure 3-17. After some preliminary tests of values chosen to give some understanding of the effect of the changes in these numbers, a series of values for B, M and N were chosen and a script written to create models featuring all combinations of the chosen values. These values are: B = (0.9,0.95,1.0,1.1), M = (0.3,0.35,0.4,0.5,0.6,0.7,0.8,0.9) and N = (0.1,0.15,0.2,0.25,0.3,0.35). For each combination of values, a model was run of the three thicknesses of alumina from the DoP experiments in Table

3-5, i.e. 5.17mm, 6.12mm and 7.14mm. From this, trend lines were extracted for thickness vs residual velocity. In this section, use of the terms gradient and intercept refer to the properties of these trend lines.

The results of these parametric study are presented in Figure 3-18 and Figure 3-19, the gradient data is presented in terms of percentage deviation from the target value, i.e. the experimental data, whereas the intercept data is presented in terms of its absolute values. In Figure 3-18, the gradients of the trend lines are displayed in terms of their percentage deviation from the experimental value (-134.2×10^{-3} s^{-1}) with the white zones indicated a match of within 10%. For each of the four values of B, this zone occurs in approximately the same area, roughly around M=0.35 and N = 0.25. In Figure 3-19, the intercept is shown. As expected, at lower values of B the intercept increases as the effective damaged strength is lower in the initial stages of pressure build up. It is worth noting that for each of the four chosen values, the maximum fracture strength limit of 0.5 is reached over the course of the application of pressure. The areas in Figure 3-19 for which the intercept is within 10% of the target intercept of 1257.7ms^{-1} occur for approximately similar combinations of M and N.

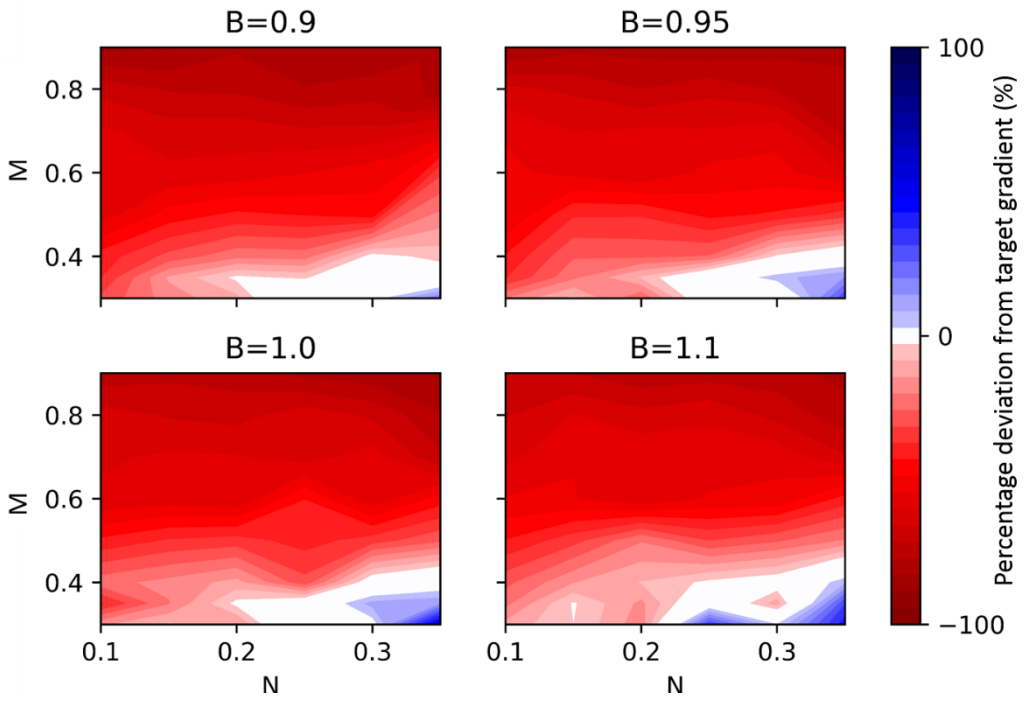

Figure 3-18: The gradient of the trendlines for thickness of alumina vs residual velocity compared to the target experimental gradient of 134.1 x 10^{-3} s^{-1}.

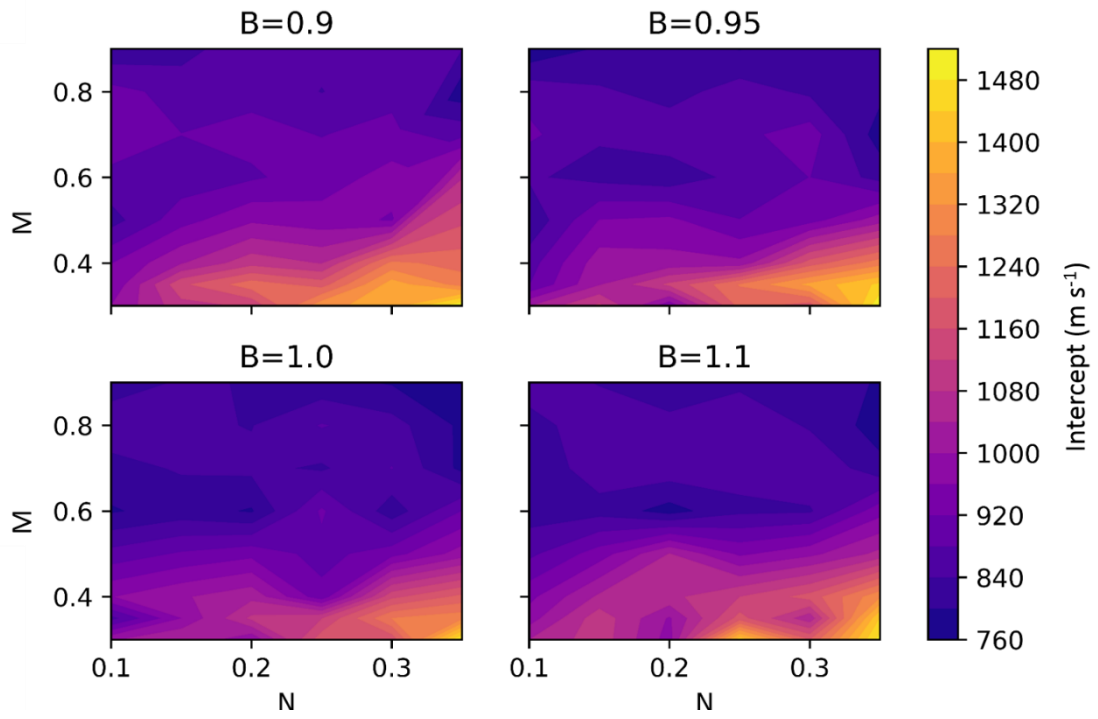

Figure 3-19: A contour plot of the intercept extracted from the lines of best fit for thickness vs residual velocity in the material parameter study to shown the effect of changing B, M, and N during calibration.

Using Figure 3-18 and Figure 3-19, the values for which B, M and N most closely match the experimental data were identified as 0.9, 0.4 and 0.35 respectively. For each thickness of ceramic, this combination of parameters produced the closest match although the actual gradient was slightly below the 10% target at -118 x 10^{-3} s^{-1}. The intercept of 1143.8ms^{-1} is within the target range. The calibrated material properties for the alumina are presented in Table 3-6.

The initial material study was performed on a model in which the upper surface of the backing mesh and the lower surface of the ceramic mesh were co-incident. In physical specimens, the two surfaces would not be perfectly smooth and there would be a small micro-metre scale gap across much of this interface as a result. This could have significant effects on the reflection or transmission of shockwaves at this interface and therefore a 0.001 mm gap was introduced into the model. It was observed that this had the effect of lowering the thickness-residual velocity gradient across the models, suggesting a greater model sensitivity to ceramic thickness. This has the additional benefit of minimising any contact problems that may arise in later models with curved surfaces at this interface as a result of discretising those curves. If the study were repeated it would include this gap from the start for consistency as it is a feature of subsequent models. In this case, the calibrated material parameters were applied to models with this small gap included

and the results show a very strong match to the target values with a gradient and intercept of 139.5 x 10^{-3} $s^{-1}$and 1278.0ms^{-1}. A comparison of the experimental data, the original matched model and the further model with a 0.001 mm gap at the backing are shown in Figure 3-20. The line of best fit for the gapped model shows very close matches for both gradient and intercept to the experimental data.

Table 3-6: Calibrated alumina material properties used in the JH2 constitutive model. Original values taken from Lundberg [52]***.***

Parameter	Notation	Al_2O_3
Density (kg/$m^{3)}$	ρ	3800
Bulk modulus (GPa)	K_1	200
Shear modulus (GPA)	G	135
Pressure coefficient (GPa)	K_2	0.0
Pressure coefficient (GPa)	K_3	0.0
Hugoniot elastic limit (GPa)	HEL	8.3
Effective stress at HEL (GPa)	σ_{HEL}	5.9
Pressure at HEL (GPa)	p_{HEL}	4.37
Intact strength coefficient	A	0.989
Intact strength exponent	N	0.35
Strain rate coefficient	C	0.0
Fracture strength coefficient	B	0.9
Fracture strength exponent	M	0.4
Normalised maximum fracture strength	S^f_{max}	0.5
Damage coefficient	D_1	0.01
Damage coefficient	D_2	1.0
Tensile strength (GPa)	T	0.13

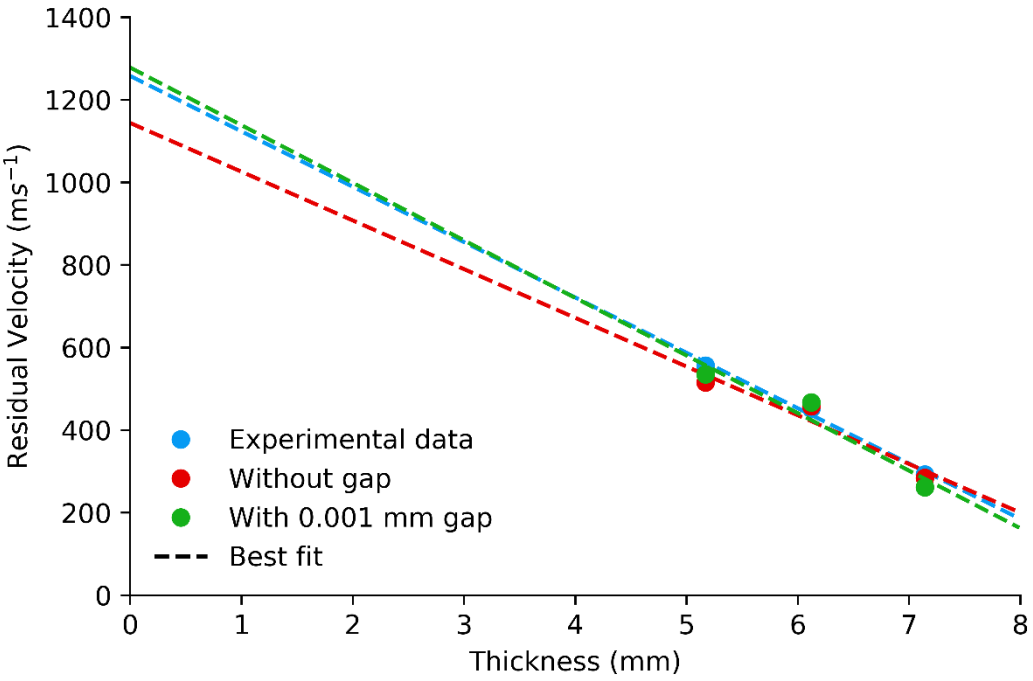

Figure 3-20: The results and lines of best-fit comparing the experimental data with the calibrated models, with and without a gap between the backing and ceramic meshes.

Ballistic experiments have shown that alumina targets with an areal-thickness of ~40 kg m^{-2} can overmatch the 7.62mm AP M2 round at NIJ IV impact speeds [1]. For a density of 3800 kg m^{3}, this corresponds to a thickness of 10.5mm. Therefore, as a final, further check of the material model being appropriately calibrated, a test model was created of the AP M2 round against a 10.5mm thick monolithic alumina tile. This thickness of tile reduced the velocity of the projectile to below zero showing that the chosen material properties behave appropriately when extrapolated beyond the bounds of the thicknesses used for calibration.

As a close match to the ballistic data has now been found, the material parameters can be considered calibrated for the specific impact conditions and, in combination with the other verified and validated fundamental aspects of the model, can be taken as a sufficiently reliable tool for use in predictive models of novel armour designs.

CHAPTER 4 – MOSAIC ARMOUR DESIGN

4.1 INTRODUCTION

When moving from a monolithic to a tiled armour design, the available design options for consideration and optimisation are greatly increased. This chapter investigates a range of geometric features in this design space and their effects on ballistic performance. A tiled system introduces interfaces in both the through-thickness plane as well as in-plane. These effects are explored separately, as layers and tiled structures, before looking at as a multi-layered tile system. The effects of edge proximity, impact site and arrangement of the tiled structure is also examined.

4.2 TILE THICKNESS AND BASELINE

The absolute thickness of an armour system is critical to its ballistic performance. If areal-density, cost and total volume were not considerations, the simplest solution to improve ballistic protection would always be to increase the thickness of the armour material. Although the relationship of thickness to residual velocity has been explored in the previous chapter on the calibration of the material parameters, a brief further study using those newly calibrated variables was performed to determine an appropriate thickness for the parametric studies on the various tile systems that follow. A baseline monolithic ceramic armour for the chosen thickness is also modelled to give a standard for comparison of future tiled designs.

An appropriate total armour thickness for the subsequent parametric studies needs to be sufficiently thick to allow time for the various functional elements of the models, such as interlocking and adhesion, to affect the failure mechanics while still being thin enough that penetration occurs. In this case, it is vital that penetration occurs because, analogous to physical experiments involving depth of penetration testing, the residual velocity after impact is the primary means of assessing the effect of the various features investigated and must therefore be non-zero.

4.2.1 Thickness model specifications

The backing and projectile meshes are as described in full detail in the previous chapter and shown in Figure 4-1. The polycarbonate backing has surface dimensions of 250mm x 250mm and is 20mm thick modelled using *MAT_ELASTIC as an isotropic hydro-elastic material. The impactor is the simplified model of the core of a 7.62mm AP M2 round described in Section 3.4, modelled using *MAT_PIECEWISE_LINEAR_PLASTICITY with a bilinear elasto-plastic stress-strain curve. The material properties for the projectile core and polycarbonate are described in Table 3-3 and Table 3-4. The alumina material properties for the ceramic target are described in Table 3-6.

The element size of the ceramic target is consistently 0.5 mm by 0.5 mm in the x and y directions and 0.5mm through thickness for all but the 1 mm thick tile that is modelled using 0.33 mm through thickness elements to ensure the advised minimum of three through thickness elements is achieved [99]. In line with the NIJ level IV ballistic standard [109], all impacts are at 875 m s^{-1}.

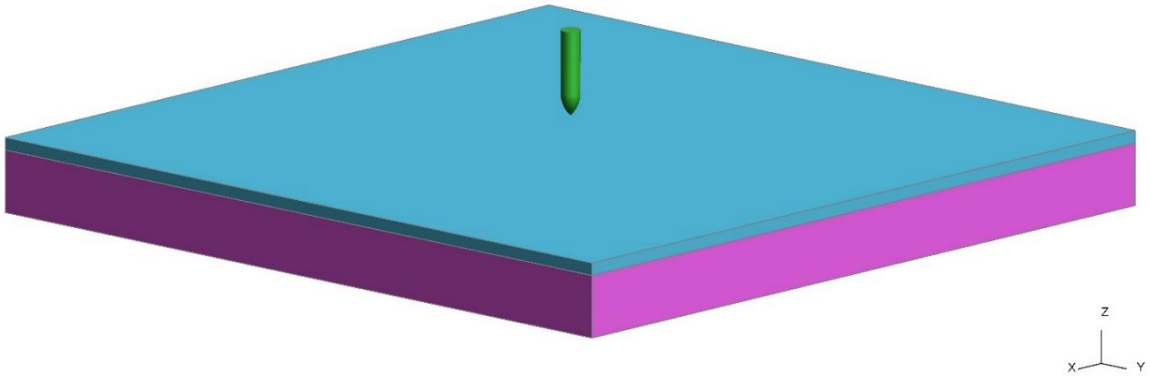

Figure 4-1: The model geometry for a 5mm through thickness tile backed by polycarbonate against a simplified model of the core of a 7.62mm AP M2 round.

4.2.2 The effect of thickness on performance

Based on the results in Figure 4-2, an appropriate thickness for further models would be 7.5 mm. This thickness has been chosen as it must thin enough to ensure penetration, i.e. below the thickness at which residual velocity is zero, while being sufficiently thick that failure does not occur too quickly allowing a chance for various intrinsic and novel damage mechanisms to be exhibited and explored. It is important for penetration to occur so that residual velocity can be used as a comparative dependent variable. As the specific thickness above which penetration does not occur is a range as opposed to a single value, it is also appropriate to choose a thickness below this range of transition thicknesses [33], indicated in grey in Figure 2-8. Impact results within this zone exhibit highly variable results and would be a confounding factor in later analysis due to this unpredictability.

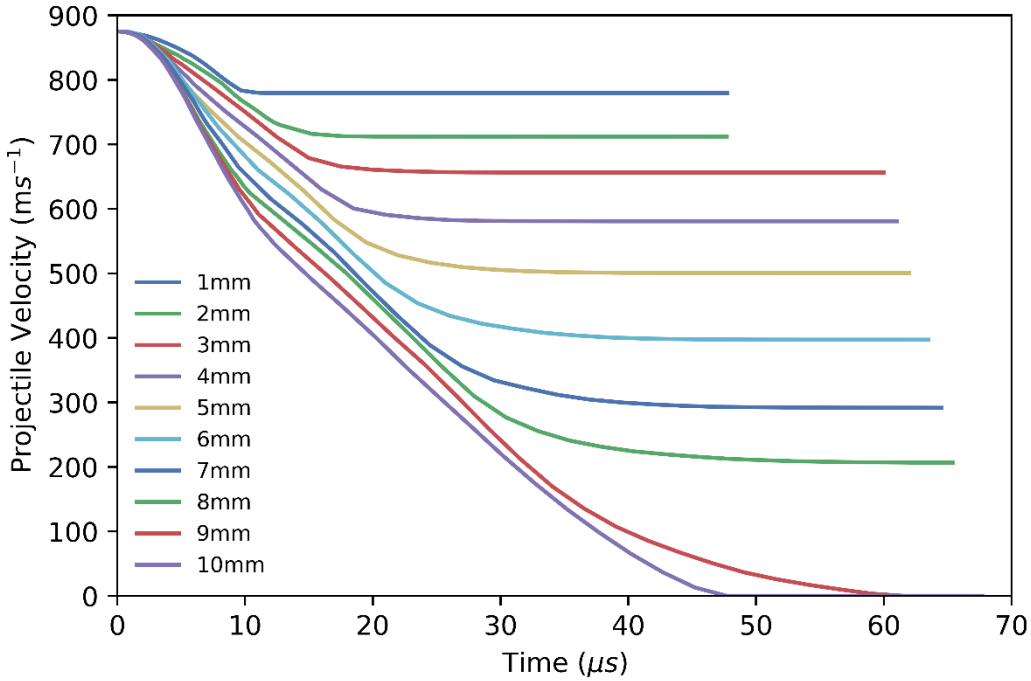

Figure 4-2: Time history of projectile velocity during impact for a range of thicknesses of alumina.

A 7.5 mm thick, 250 x 250 mm monolithic ceramic armour model was then run to provide a baseline for ballistic performance. The residual velocity for this armour is 209.6 m s^{-1}. It can be seen in Figure 4-3 that, prior to reflection from the back face, wave propagation through the ceramic is identical regardless of thickness of the target. However, after reflection it can be seen in the 7mm thick target that there are some relief waves returning from the back face by 1.8 μs that reduce the von Mises stress in the ceramic that have not yet been reflected in the thicker ceramic at the same time after impact. The initial reflection can be made more apparent by reducing the maximum shown pressure of the contour plot down to 1 GPa to allow for a finer gradient over slightly lower stresses, this allows for the reflected wave to be seen in the 7 mm tile (Figure 4-4).

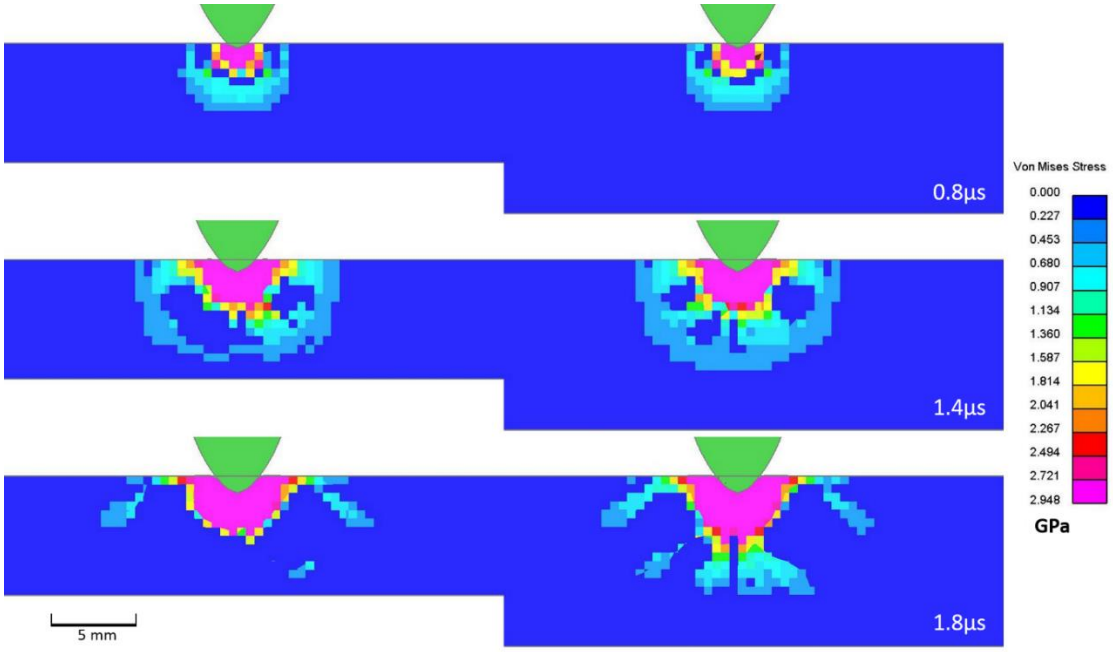

Figure 4-3: A cross-section showing a comparison of the von Mises stresses ahead of the projectile in a 7 mm and 10 mm alumina target.

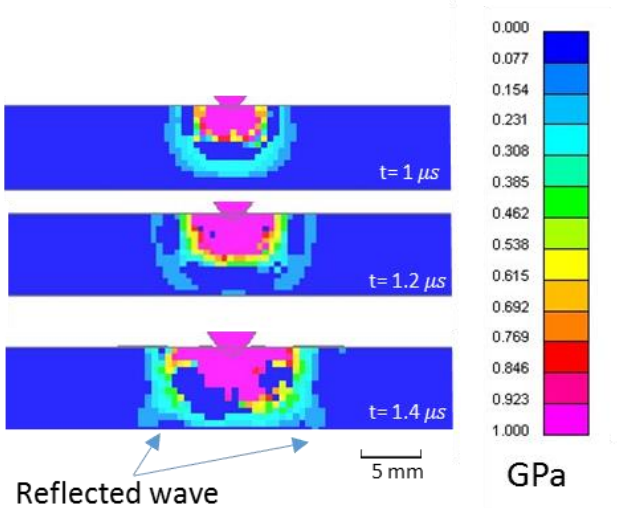

Figure 4-4: By gating the contour plot gradient to show a maximum of 1 GPa of stress, the reflected stress wave can be seen in a 7 mm thick ceramic target.

Previous numerical simulations investigating thickness have used an exponential decay fit of the form

$$V_R = V_0 + Ae^{-\frac{t}{\lambda_1}} + Be^{-\frac{t}{\lambda_2}} \qquad (4\text{-}1)$$

relating the thickness, t, the residual velocity, V_R, dependent upon the impact velocity, V_0, and three fittings constants: A, λ_1 and λ_2 [110].

4.3 TILE LENGTH AND EDGE PROXIMITY

As discussed by James and Hazell [2,24], increased proximity of an impact to the edge of a tile introduces a range of effects that have a negative impact on ballistic performance. The proximity of these free surfaces allows for dissipation of the bulking pressure that would otherwise increase the yield stress of the ceramic, both intact and comminuted, effectively ending the period of dwell prematurely. Therefore, when creating a tiled array, it is important to be aware of the extent of this influence on ballistic performance. Studies of silicon carbide made through two different manufacturing techniques, liquid-phase-sintered vs hot processing, showed that edge proximity is not correlated with ballistic performance if the ceramic is unable to damage the projectile core but shows a strong influence should the ceramic be of sufficient strength and hardness [24].

4.3.1 Tile edge length

A series of simulations of square tiles of different edge lengths for a fixed thickness of 7.5 mm were performed. Further to the reasons described at the conclusion of the previous section, this thickness also shows residual velocities equivalent to those in the material that exhibited an edge-proximity effect in Hazell [24]. In this work, it was seen that thinner tiles did not exhibit these effects; likely due to the occurrence of earlier failure. The models in this section have the same set-up as previously described, including mesh density, with the exception of the ceramic tile that is replaced with differently sized tiles. An example of the mesh for the 160 x 160 mm tile edge length model is shown in Figure 4-5.

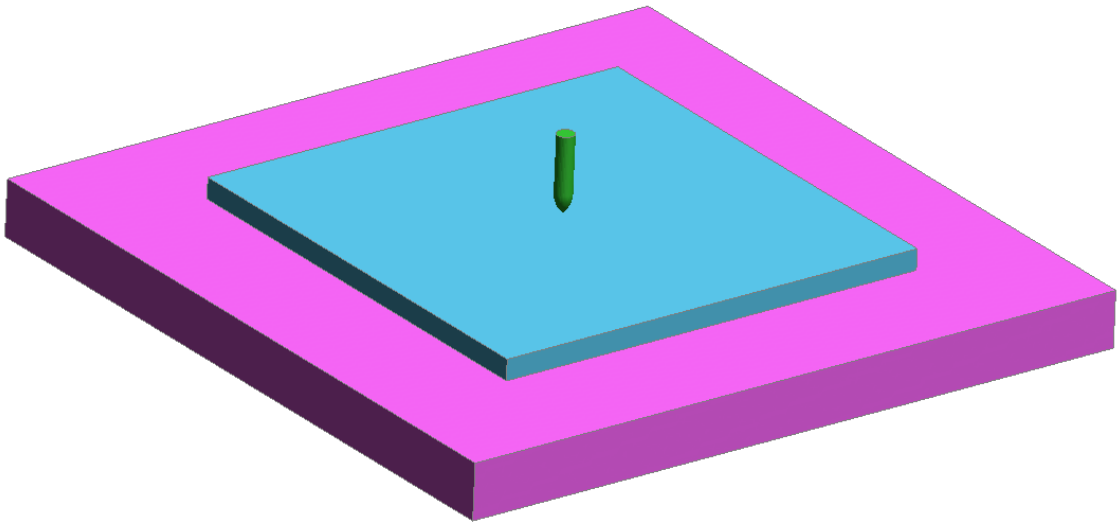

Figure 4-5: A model showing a 160 x 160 mm tile above a polycarbonate backing prior to impact.

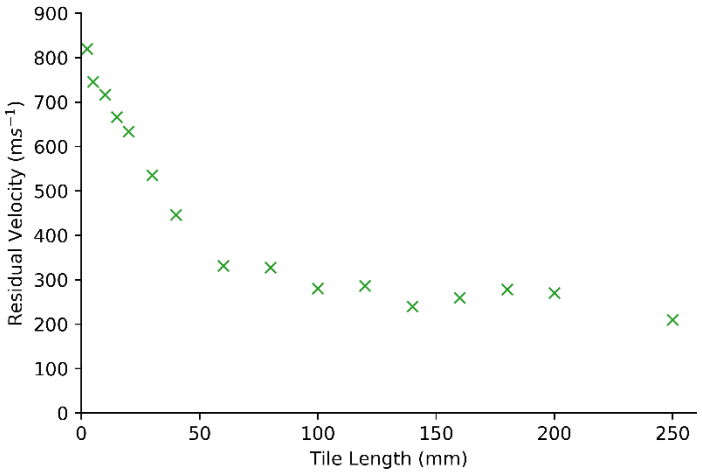

Figure 4-6: The residual velocity for a centred impact of a 7.62mm AP M2 core on a 7.5 mm thick alumina tile as a function of varying the tile side lengths.

Rough industry guidelines have an advised minimum tile size for mosaic armour of ~10 times the diameter of the projectile they are designed to protect against to minimise edge effects [11]. The results of the tile length study in this work shows diminishing returns for tile sizes beyond approximately 60 mm tile length against a projectile of 6.17 mm in diameter, showing strong agreement with the industry "rule-of-thumb".

One phenomenon that may influence performance is the difference between shear and compressive wave velocities in a given material. These waves speeds being different suggests that for some combinations of tile length and width the first returning waves reflecting from interfaces will be from the compressive shockwave travelling through the thickness of the tile and for others it will be the shear wave reflected from the tile edges traveling perpendicularly to the projectile velocity. This transition point would depend on the difference between shear and compressive velocities. Compressive wave speed, V_p, is given by

$$V_P = \sqrt{\frac{K + \frac{4}{3}G}{\rho}} \tag{4-2}$$

and shear wave speed, V_s, is given by

$$V_s = \sqrt{\frac{G}{\rho}} \tag{4-3}$$

in which K is the bulk modulus and G the shear modulus. For the alumina material properties used in these simulations, G = 135 GPa and K = 200 GPa [52]. Therefore V_P = 10,000 m s^{-1} and V_S = 5960 m s^{-1}. This gives a relation between the two wave speeds in the ceramic of

$$\frac{V_p}{V_s} = 1.678\,. \qquad (4\text{-}4)$$

Taking the wave travelling radially outward in the plane perpendicular to impact as a shear wave and the shockwave travelling ahead of the projectile as compressive, the shockwave reflections would return to a centred point of impact (PoI) from the tile edges ahead of the reflected compressive waves for tile edge lengths $\leq$ 4.5 mm for a 7.5 mm thick tile. These waves will act as relief waves and allow for the dissipation of the built-up bulk pressure that acts to increase the yield stress during impact, as such the returning waves act both to weaken the material due to damage and due to the drop in pressure. This may be noticeable in the slight steepening of the trend shown in Figure 4-6 but given the variations between the data points, this cannot be drawn conclusively.

This study also provides the baseline of performance for a 250 x 250 mm, 7.5 mm thick monolithic ceramic tile of 209.6 m s^{-1} against the simplified 7.62 mm AP M2 model impacting at 875 m s^{-1}. This is to provide the baseline of comparison for all future models.

4.3.2 Proximity of impact to the tile edge

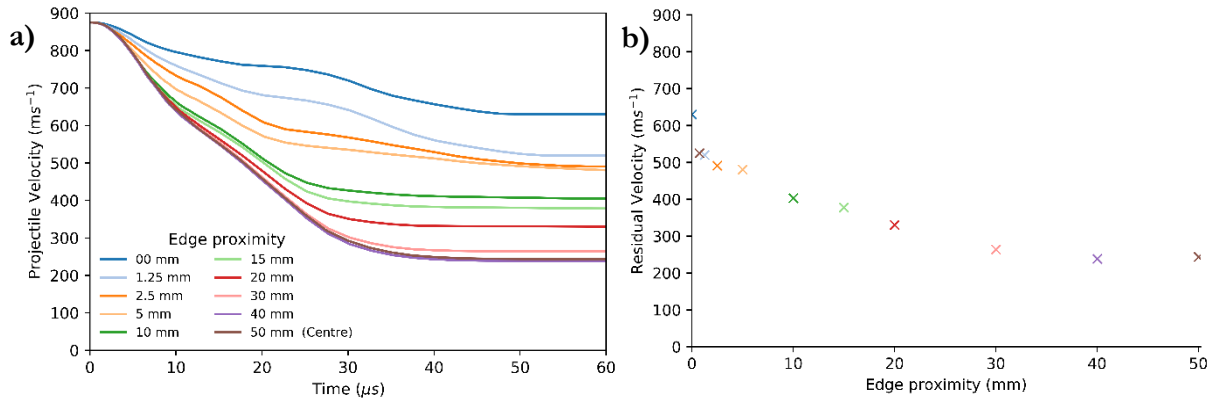

Figure 4-7: (a) The velocity time history for a projectile on a 7.5mm thick 100mm edge length square alumina tile for various edge proximities. (b) Residual velocity as a function of edge proximity.

A study of the effect of edge proximity for a fixed width square tile of 100mm edge length and 7.5 mm thickness impacted at 875 m s^{-1} was performed (Figure 4-7). As expected, there is a considerable drop in performance near to the tile edge with a considerable further drop for impacts that directly strike the edge. During direct edge impacts, the projectile is also rotated about the x-axis (where z is the impact direction) by ~30°. In accordance with the previous tile length study (Figure 4-6), improvements in ballistic performance with increasing distance plateau for distances above 30 mm from the edge, i.e. the same distance from the edge as for a centrally struck tile of approximately 10 times the diameter of the projectile.

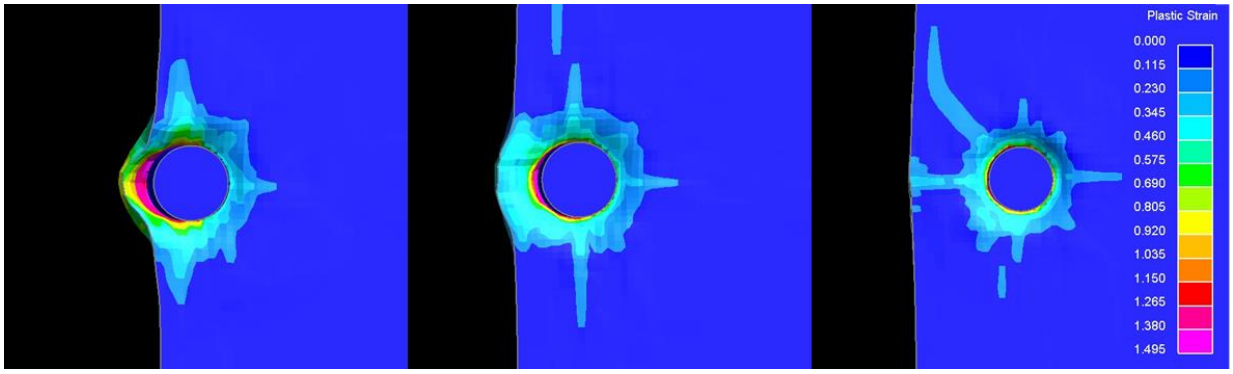

Figure 4-8: 11 μs after impact at edge proximities of 2.5 mm, 5 mm and 10 mm (left, centre and right respectively) with plastic strain displayed.

For impacts within 5 mm of the edge, flexural failure at the edge is observed due to the immediate damage zone around the PoI (Figure 4-8). In these cases, there is considerable spalling of material laterally out from the free surface. At proximities greater than this, failure occurred at the edge due to cracks propagating radially out from the PoI. This change in failure mode at the nearest free surface may be responsible for the observed change in the trend line of residual velocity vs edge proximity i.e. the impacts at a distance of 0.75mm to ~5mm from the edge form a cluster around 520 m s^{-1}. It is possible this is because, for the impacts run that are closer than 4.5 mm to the edge, the nearest free surface is that of the edge of the ceramic tile. In such cases the relief waves first arriving at the damage zone below the point of impact would be from the edge rather than, as in most cases further away from the edge, from the interface of the tile with the backing. It may be a useful course of inquiry for future research to further investigate the effect on failure mode of the proximity of the tile edge to the PoI on ballistic performance.

4.4 LAYERS

4.4.1 Layered systems

The inclusion of layers into a ceramic design introduces interlayer surfaces that affect the underlying shockwave behaviour after impact. This is significant as the propagation and reflection of the impact shockwave is one of the primary influencing factors in the subsequent damage and ballistic performance of a ceramic under impact. A series of impact simulations were performed of an alumina ceramic tile with a width and length of 250 mm and a total thickness of 7.5mm divided into layers with a 0.001 mm gap between them. All models were meshed with the same element density as previously with the through-thickness element size being approximately 0.5mm with adjustment to maintain the appropriate geometry. Models of 6, 7 and 8 layers were considered, however the through-thickness mesh required further refinement to ensure 3 elements through-

thickness and, given the mesh sensitivity effects discussed in the convergence studies of the previous chapter, these results have been excluded.

In moving from a monolithic system to a two-layered system there is an immediate 8.5% reduction in ballistic performance, when comparing residual velocity with the initial impact velocity (Figure 4-9). In future analysis, kinetic energy may be a more useful measure of performance but residual velocity and total reduction in projectile velocity are sufficient here. Further increases in the number of layers shows continued decreases in ballistic performance. Comparing the overall change in velocity of the projectile, a three-layer system reduces performance further to 86.4 % of that of the equivalent thickness monolithic system. Increasing to four and five layers give ballistic performances that are 73.6% and 70.7% that of the monolithic system respectively. These are tiles performing in the absence of any cohesive interlayer, an addition that will be investigated at a later stage. A further possible future study, not undertaken here but potentially of interest, would be into the effect of subdividing the same total thickness into unequal thicknesses of layers.

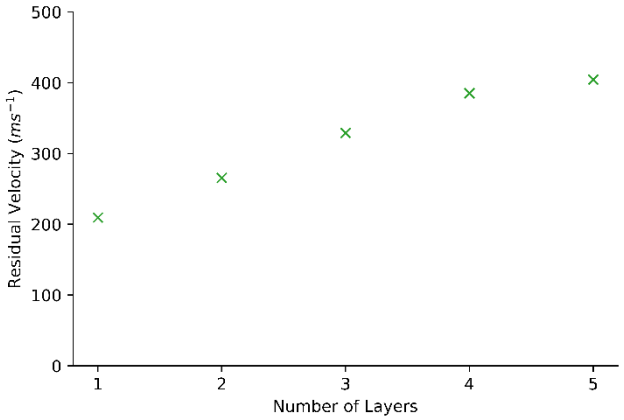

Figure 4-9: The residual velocity of a 7.62mm AP M2 round impacting at 875 m s^{-1} on alumina targets of total thickness 7.5 mm divided equally into a range of sublayers.

A comparison of one, two and three-layered targets, all of total thickness 7.5 mm, show the initiation of secondary Hertzian cones originating at points on the lower surfaces directly below the PoI (Figure 4-10). The two- and three-layered targets show this repeated conoid stress pattern whereas the single layer only presents the stress pattern propagating spherically from the PoI. Interestingly, the three-layered target also shows a higher peak stress (4.5 GPa vs 3.5 GPa for the triple and double layered targets respectively) during impact. This may be due to the superposition of the reflected waves from each subsequent interface causing more complex wave interactions.

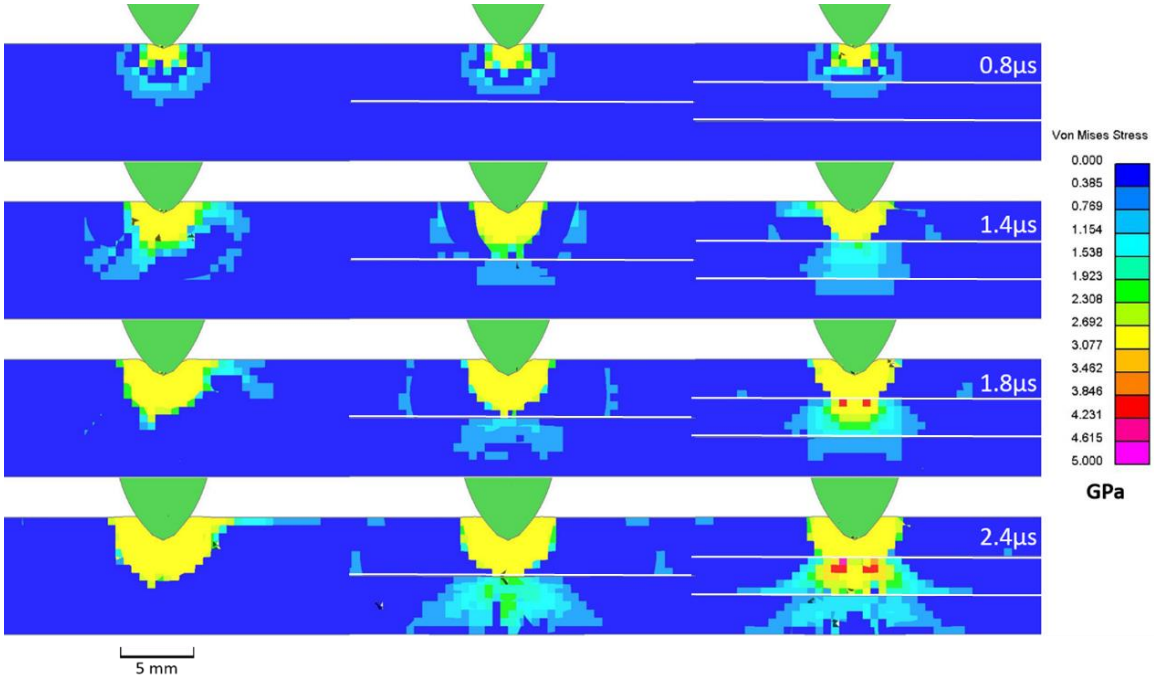

Figure 4-10: A comparison of the von Mises stress wave propagation through the ceramic on impact. Each target is 7.5 mm in total thickness divided into one, two and three layers respectively left to right. The interfaces have been highlighted for clarity.

4.4.2 The effect of tile edge length in layered systems

There is an expected trade-off in choosing the tile size for a tiled armour system between single-impact ballistic performance and localising the damage for greater multi-hit performance. As suggested by previous research, spread of the damaged volume is inhibited by a smaller tile size [24]. When considered alongside the results from Figure 4-6, this suggests that the optimal tile size will be the smallest tile after the point of diminishing returns. It is plausible that the tile edge length (as explored in Section 4.3.1) at which a performance plateau is reached is dependent on the tile through-thickness profile. For this reason, a series of tests were run varying the tile edge length of a system of three stacked 2.5 mm thickness tiles, i.e. maintaining a fixed total thickness of 7.5 mm. The results are shown in Figure 4-11 and are shown in comparison to a 7.5 mm thick single-layered alumina block.

Both series begin to level off at approximately 50 mm edge lengths although the single layer trendline continues to show performance improvements as far as ~120 mm edges, the three-layered series showing no marked improvements beyond 90 mm. This suggests that optimal tile size for a layered system is lower than that for a non-layered (or single layer) system. This is possibly due to edge-effects influencing the impact behaviour sooner in a system made up of thinner layers compared to a monolithic material and becoming the dominant factor in determining ballistic

performance. In a layered system there is a shorter dwell time, or even a series of shorter dwell periods, compared to the longer dwell time that a thicker tile affords and this factor becomes the overwhelmingly dominant influence on ceramic high strain rate behaviour when the in-plane edges are sufficiently far away such that the impact event is effectively "over" prior to shockwave reflection from those edges.

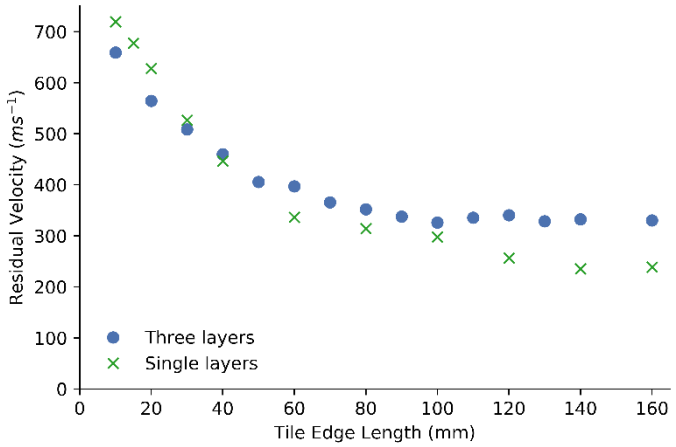

Figure 4-11: The effect of tile edge length for a three-layered system of three 2.5 mm thick alumina tiles against the standard 7.62mm AP M2 simplified model impacting at 875m s^{-1}.

For very small tiles the three-layered system outperforms the monolithic tile with an intersection occurring between 30 mm and 40 mm tile edge lengths. At greater tile edge lengths, the trend lines plateau and show a steady difference in performance after approximately 120 mm of the three-layered system causing a deceleration in projectile velocity of ~88% that of the higher performing monolithic system, similar to earlier results for a 250 mm tile edge comparison in Figure 4-7.

As discussed previously it is clear that the introduction of through-thickness interfaces acts to reduce ballistic performance by the reduction of the dwell time and the subsequent reduction in bulk pressure that would otherwise increase the in-situ yield stress of the ceramic during impact. However, it is not entirely clear why there is a greater performance of the three-layered over the single-layered system for sub-40 mm tile lengths. This behaviour could be related to the conic shape of the stress waves created at the boundary interfaces between subsequent layers that is, obviously, not present in the single -layered designs due to the lack of tile interfaces. Comparing the two systems using the 10 mm tile edged models, it can be seen that at $1\mu s$ after impact the stress wave pattern below the PoI is very similar, i.e. the same spherical stress wave radiating from the PoI. However, just $1\mu s$ later there is significant divergence as the compressive shockwave meets the first through-thickness interface and is propagated as a stress cone instead of continuing the hemi-spherical spread as in the single-layered case.

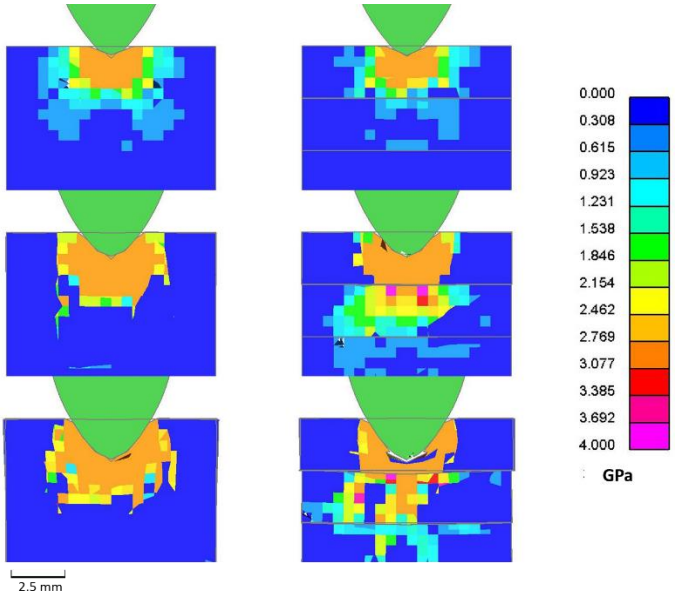

Figure 4-12: The von Mises stresses below the point of impact for a single layered and triple layered 7.5 mm thick alumina target of edge length 10 mm.

4.5 TILED ARRAYS

4.5.1 Single Layered

Having investigated the effects of tile dimension on ballistic performance for individual tiles, the next step is to move to a tiled array. The first investigation is into the effect of impact site on a basic 2 x 2 tile system, in particularly the differences from the edge proximity effects shown in Figure 4-7. This design comprises of 4 tiles 125mm x 125 mm x 7.5 mm arranged in a "square" mosaic formation with the backing material extending to the tile edges (Figure 4-13). In the same manner that a 0.001 mm gap is left between the backing and the tiles in all previous models, this and all future tiled arrays are separated by a 0.001 mm gap between any one tile edge and the next nearest surface. This serves to minimise material failure occurring due to the contact algorithm overcompensating for any small initial penetrations caused by a mesh mismatch between curved surfaces; soft-contact option 2 also serves to reduce this issue by zeroing all initial displacements prior to the first time-step of the model.

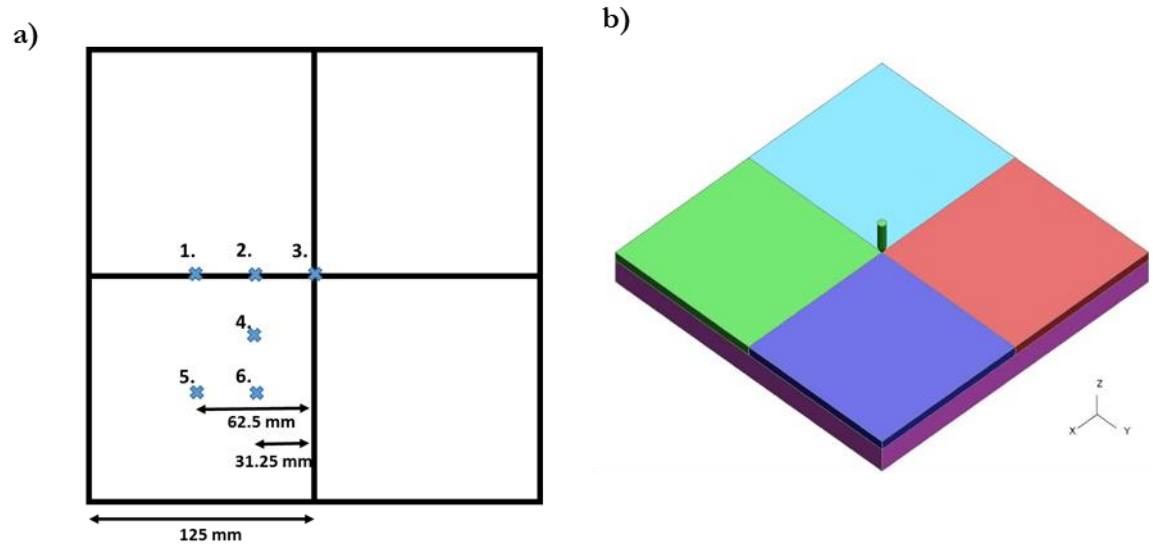

Figure 4-13: a) A schematic in plan-view of the impact sites chosen to investigate the effects of impact position relative to tile geometry for a tile array of 4 square tiles of edge length 125 mm and thickness 7.5 mm. b) An isometric view of the FE model of the same schematic showing a centred impact.

As shown in Figure 4-13a, six distinct impact locations were chosen to represent the possible types of impact that may occur on a tiled design. There are impacts central to the tile, on tile interfaces and on a triple or quad-point (for offset and square designs respectively), as well as three further impact sites chosen to be midway between these sites. For mosaic structures with more than one layer there are also further cases representative of different through thickness profiles, not all of which will be explored.

The results of this test show considerable dependence on impact site for a tiled armour (Table 4-1). They also show that a tiles performance is greatly improved by being part of a tile array rather in isolation (in comparison to results shown in Figure 4-7). As these tiles are large enough to not be bounded on all sides by other tiles, the performance for impacts at the centre of the tile is comparable to similar tiles in isolation, with residual velocities of 253.2 m s^{-1} and ~256.6 m s^{-1} respectively. However, tile edge performance for tiles with edges internal to the array (impact sites 1, 2 and 3) is much greater than would be expected by the trend shown in Figure 4-7b. Instead, edge-on impacts in a tile array have a similar performance as impacts on pre-existing cracks. Impacts on external edges, or on the edges of isolated tiles, reduce performance by as much as ~60 % when compared to impacts at the centre of a tile. When tiles are impacted at boundaries with other tiles, the performance reduction is ~18%. The failure mechanics are much more similar to impacts in proximity to pre-existed cracks; for comparison, physical tests involving 1 mm cracks showed a reduction in ballistic performance of 9% [27].

Further, the performance in both on-edge and quad-point impacts is still greater than impacts on single tiles in which the entirety of the diameter of the projectile is only just within the bounds of the tile, i.e. for impacts greater that 3.08 mm (i.e. the radius of the projectile) from the tile edge. For example, an impact at 5 mm from the edge of a single-tile target is reduced to 480.2 m s^{-1} residual velocity in comparison to 364.8 m s^{-1} and 384.9 m s^{-1} for on-edge and quad-point impacts respectively. This shows that the material across the boundary is involved in the failure mechanics of the impacted tile both in the form of confinement of the damaged material and in energy absorption due to the partial transmission of the shockwave across the interface rather than full reflection as in the unbounded case.

Table 4-1: The variation in ballistic performance based on impact site for a single layer of tiled armour of 7.5 mm thickness and tile edge length of 125 mm. Impact site numbering corresponds to Figure 4-13a.

Impact Site	***Residual Velocity (m s^{-1})***	
	125mm	***62.5mm***
1. Two-tile interface	364.8	370.6
2. Interface mid-point	376.1	375.7
3. Quad-point	384.9	400.0
4. Interstitial	316.8	321.4
5. Tile Centre	253.2	300.6
6. Interstitial	289.6	320.6

A further study was conducted of a similar range of impact locations with an array of smaller tiles, 62.5mm edge length, tiled to cover the same total area, i.e. 4 x 4 total tiles. The chosen target tile was one of the four inner tiles that share the centre and is therefore bounded on all sides by other tile providing a form of confinement not found in equivalent single tile studies. The first clear observation is that the 62.5 mm tile in an array performs better than even the 80 mm single tile due to this confinement for reasons similar to the 125 mm arrayed tiled (300.6 m s^{-1} vs 327.8 m s^{-1}). The overall trend in ballistic performance matches closely that of the 2 x 2 array of 125 mm tiles.

A brief study was undertaken of a range of single layered tile arrays, in both a square pattern and a staggered (or offset) pattern, all impacted centrally at 875 m s^{-1}(Figure 4-14). In the square-tiled

arrays, every row and column lines up evenly as in the 125 mm tiled array in Figure 4-13. For the offset array, the tiles are lined up evenly within each column individually, but each column is offset from the adjacent columns by half the length of the sides creating the staggered offset pattern. Examples of these tile patterns can be seen in Figure 4-15 and Figure 4-17.

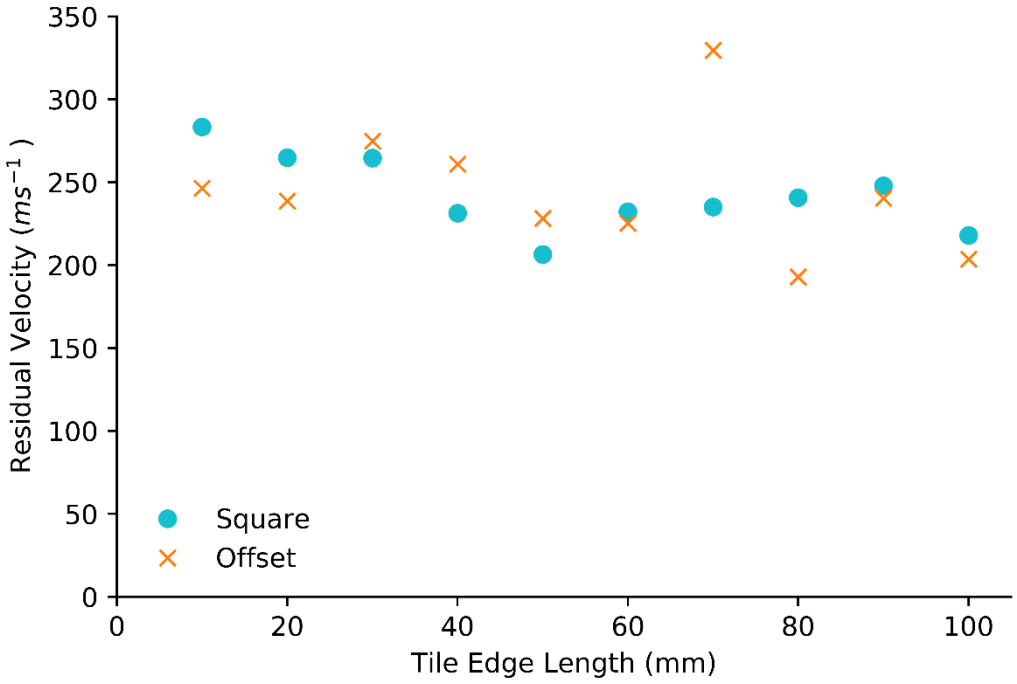

Figure 4-14: A comparison of residual velocity after an 875 m s $^{-1}$ impact for a range of single layered 7.5 mm thickness tile arrays in square or offset layouts.

When placed into a tiled array, the ballistic performance for centred impacts of the tiles is considerably increased over that of a single tile of equivalent edge length in isolation (compare Figure 4-6 to Figure 4-14). For example, a single 7.5 mm thick square tile with an edge length of 10 mm leaves the projectile with a residual velocity of 717.2 m s $^{-1}$ whereas the same tile in an array reduces the projectile velocity to 283.3m s $^{-1}$. Further, unlike in previous studies of tile edge length effects on ballistic performance, there is a very limited effect of increasing the tile size when used in a tiled array. Whereas in the single tile case the 100 mm edged tile is 4 times the ballistic effectiveness in terms of reduction in velocity compared to the 10 mm tile, for a tiled array the 100 mm tile outperforms the 10 mm tile by only 11%. This is likely due to the effect of the mass constraints adding greater confinement, a feature noted previously to greatly increase ceramic performance under impact, outweighing the reduction in performance introduced by the inclusion of closer lateral interfaces for wave reflection. With sufficient mass around the target area, the tile edge does not greatly affect ballistic performance. The tiles in an array perform comparably to the same size monolithic tile; residual velocity for a monolithic 7.5 mm thick 250mm x250mm alumina

tile is 209 m s^{-1} compared to ~260 m s^{-1} when divided into 20mm x 20mm tiles of the same thickness.

However, as ballistic performance is notably weaker when directly impacting tile edges (with 125mm square tiles showing a ~ 20% reduction in performance for edge impacts (Table 4-1)), and smaller tiles lead to a greater probability of impact on a tile edge or quad/tri point there is a statistical reduction in the performance of the armour. This suggests that for single layered tiled armours, larger tiles should be chosen to reduce the likelihood of edge-on impacts in use in the field.

The damage pattern produced under impact is heavily dependent on the impact site. The first notable observation is the localisation of damage relative to monolithic targets (Figure 4-16). For example, comparing both offset and square 10 mm tiled targets with a monolithic target at 4 μs after impact shows significantly inhibited crack propagation. The monolithic tile shows radial cracks that have travelled 27 mm from the PoI whereas both the tiled systems have cracks that have terminated at tile boundaries at 15 mm from the centre of damage (Figure 4-15). At a later time of 7μs, the total radius of the damage zone for the both the tiled and monolithic ceramics is comparable at ~70 mm however the damaged volume of the monolithic tile is lower than that of the tiled equivalents. The damaged volumes are 3895 mm^3, 7112 mm^3 and 4533 mm^3 for the monolithic, offset tiled and square tiled targets respectively (Figure 4-16). The tiled systems result in greater localisation of damage but much greater damage volume with the damage zone due to the greater level of reflected tensile waves from the tile edges. This is not necessarily a negative with regards to performance although, when considering multi-hit performance, it must be kept in consideration as this may lead to lessened localised multi-hit performance while achieving greater multi-hit over the full surface area of the armour system.

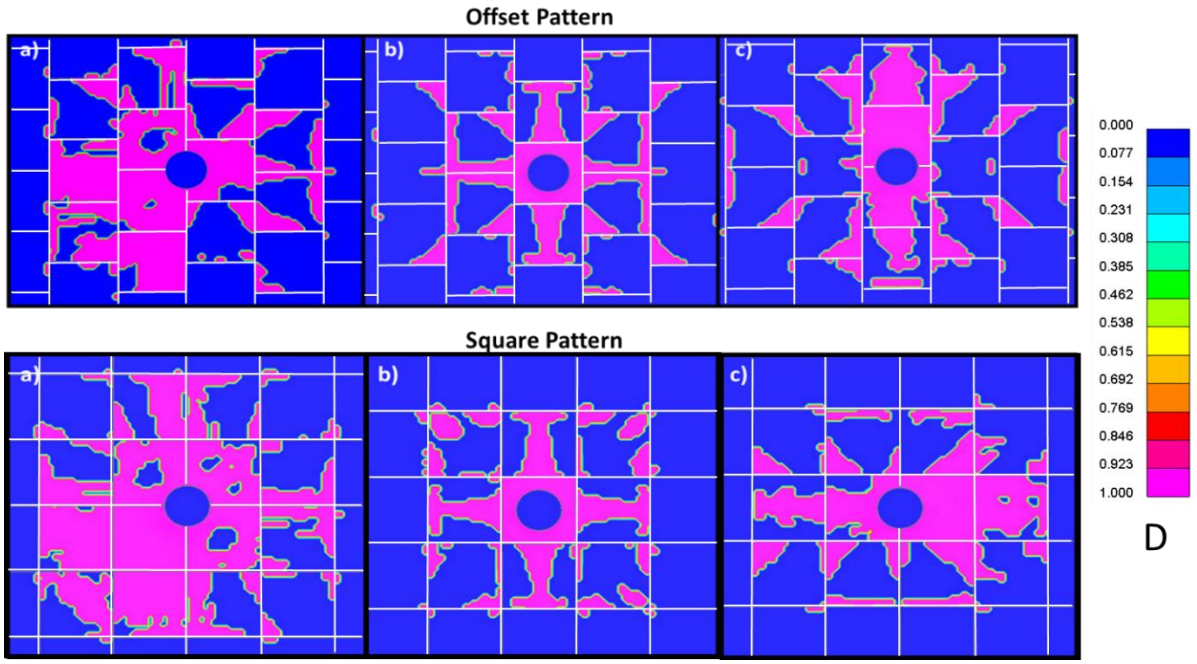

Figure 4-15: Contour plots for D, the damage variable, that illustrate the damage pattern produces by impacts on a 10 mm single-layer tile array of 7.5 mm through thickness at a) a triple-point b) a tile centre and c) a tile edge. These images are captured at 4 microseconds after impact.

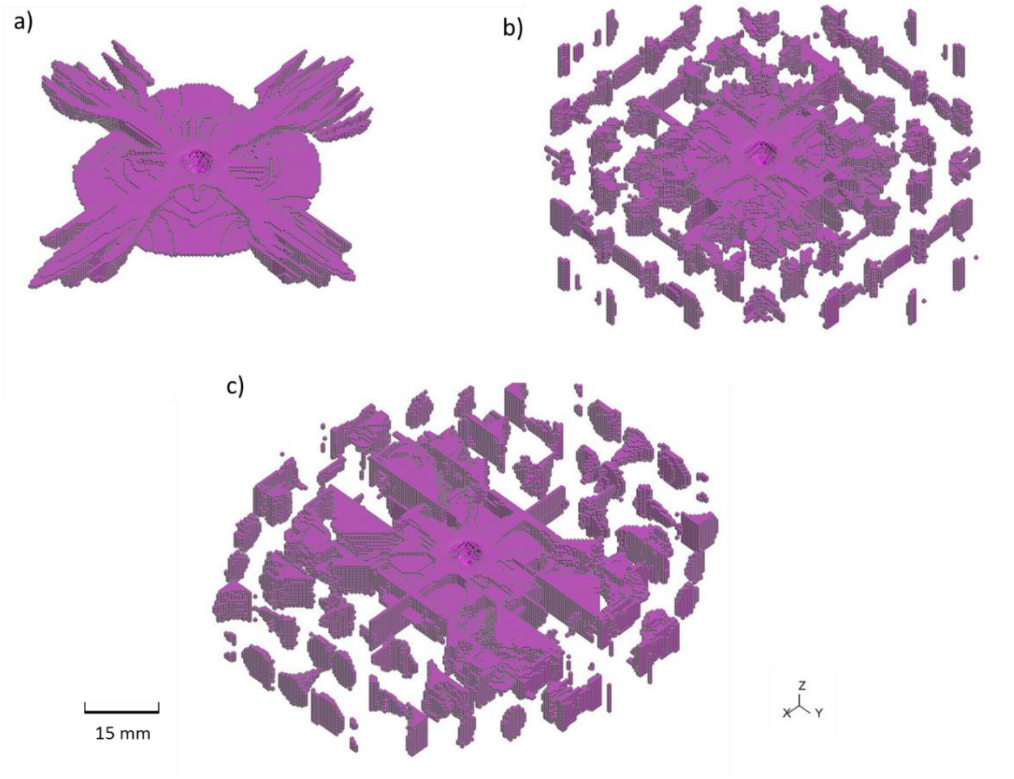

Figure 4-16: FE models showing the damaged volume 7 μs after impact for a) a monolithic tile, b) a square-patterned tile array of 10 mm tiles and c) an offset-patterned tile array of 10 mm tiles. The total volumes for each are 3895 mm², 4533 mm² and 7112 mm² respectively.

4.5.2 Three Layered Mosaic Armour

From the results of the layered tiles study (Figure 4-9), it was determined that a three-layered system would be the baseline for layered tiles. This allows for full topological interlocking of the top and bottom surfaces of at least the central layer whilst not incurring the further reduction in performance of additional layers beyond that criteria. A final study, prior to investigating novel tile geometries, was undertaken to determine an optimal tile size for flat, layered ceramic tiles. The preceding studies outlined in this chapter have led to a chosen total thickness of 7.5 mm and therefore an individual tile thickness of 2.5 mm. Tile-edge length for a single-layered tile as part of an array appears to have minimal effect on ballistic performance although there is a small improvement from increased tile size (Figure 4-14). The improvement in performance in this system from 10 mm to 100 mm tile size is a further reduction in projectile velocity of 65.3 m s^{-1}, i.e. a residual velocity of 283.3m s^{-1} at 10 mm compared to 218.0 m s^{-1} at 100 mm. However, all tiles in the single layer array regardless of tile size (down to the 10 mm edge length studied) still outperform a monolithic tile just 0.5 mm thinner (a 7 mm monolithic target has a residual velocity of 291.6 m s^{-1}). This is to emphasise that tile thickness, for single-layered targets, is the single most important factor in ballistic performance provided that sufficient lateral mass is available around the POI to act as an inertial constraint and allow the build-up of pressure during penetration.

The introduction of layers and boundary interfaces in the through-thickness profile of the ceramic reduces performance but, as noted, is necessary to incorporate a topologically interlocking architecture. The purpose of this compromise is to localise the damage zone and therefore possibly provide greater multi-hit performance. The armour design must therefore be optimised around that requirement to maximise the compromised single shot ballistic performance.

The two three-layered tile layouts investigated have been labelled "square" and "offset". In the square design, all tiles are fully aligned in their rows and columns, each layer is directly on top of the other so that any tile interface aligns with the neighbouring tiles and continuing to the armour edges and to the upper and lower tile surfaces. The offset designs are, within layers, aligned in their columns but offset by half a tile-length with their neighbouring columns. The lower layer is offset to the middle layer by half a tile-length in the x-direction and a quarter tile-length in the y-direction to prevent any interfaces from being unobstructed from the top to the bottom surface (Figure 4-17). The tile arrays for both the square and offset arrangements have a minimum upper surface that is 250 mm x 250 mm in area. In the cases that this minimum size is not exactly divisible by the tile edge lengths, and in all offset cases, tiles are added to ensure the array covers this minimum size and there is some amount of tile surface that overhangs this central surface area. The results

in Figure 4-6 show that above a certain threshold size (~100-120mm) there is minimal effect of increasing the target surface area on ballistic performance, i.e. beyond this size the target acts as a quasi infinite tile array for the time scale of the ballistic interaction, and therefore this extra ceramic material is not considered to have a significant effect on the results although would be trimmed in a final design.

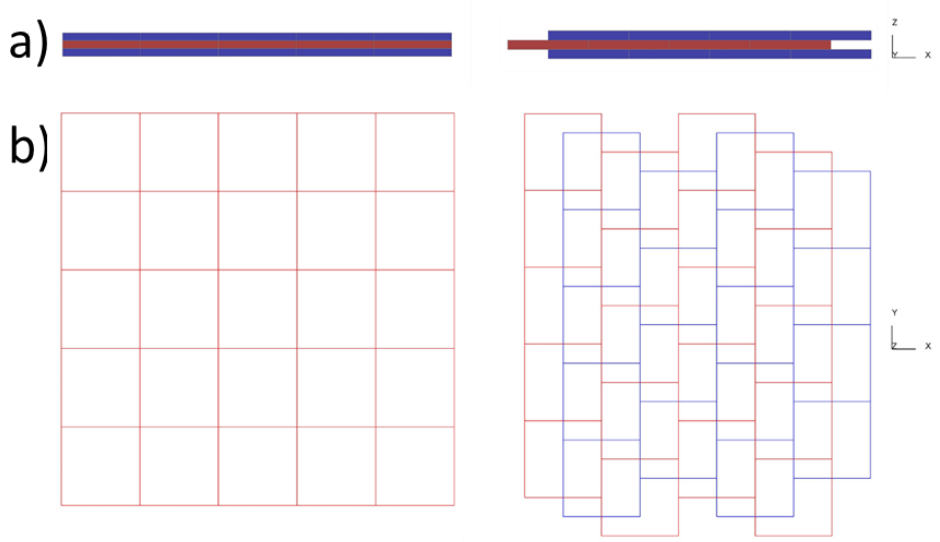

Figure 4-17: A representative schematic of the square and offset tile arrays (a) in profile and (b) in top-down perspectives.

As in the single-layer designs, there is minimal clear effect on performance of changing tile edge length in a mosaic system (Figure 4-18). The residual velocity at quad and triple points, i.e. tile-corner impacts for square and offset designs respectively, shows a particularly flat trend line with all results clustered around 230 m s^{-1}. The offset design performs slightly better than the square designs for impacts at tile corners, quad- and tri-points, although this difference is marginal with the 50 x 50 mm tile sets performing nearly identically at these points (427.5 m s^{-1} vs 427.6 m s^{-1} for square and offset respectively). These are notably weaker points in the design, and it would be expected that an offset design would perform better given that the offset tiling pattern ensures that beneath each triple-point is some non-interfacial tile material, compared to the square pattern in which quad-points are stacked precisely on top of each other. This difference being so small suggests that the performance of the upper tile is the pre-dominant factor in ballistic performance.

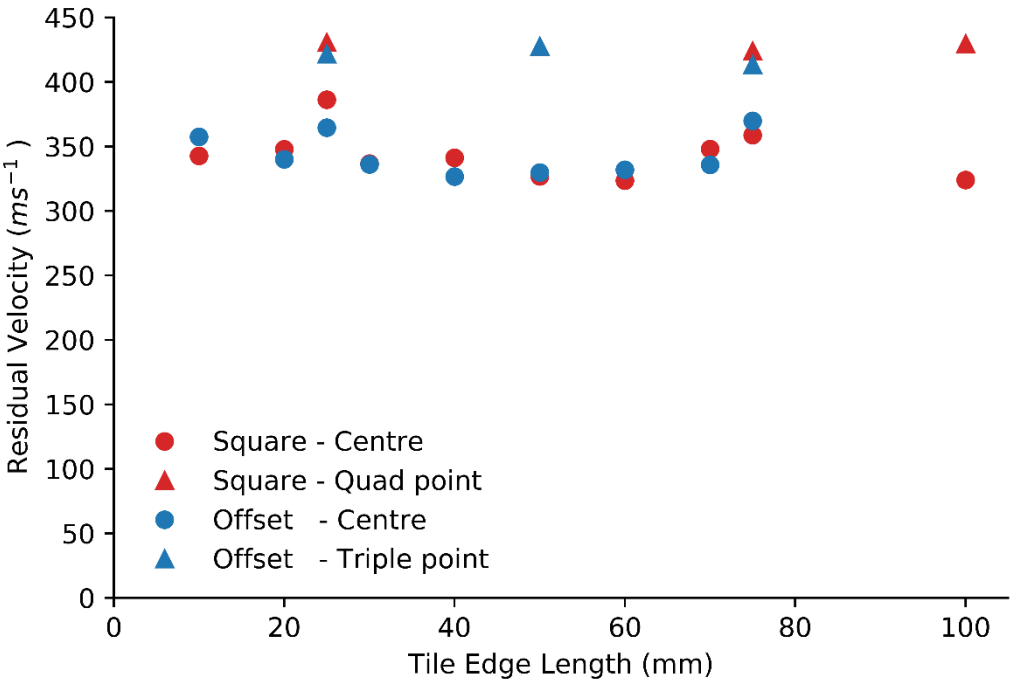

Figure 4-18: A comparison of the residual velocities after impact of an 875 m s^{-1} AP M2 projectile impacting several layered tile arrays arranged in both square and offset patterns. Quad- and triple-point impacts exhibit similar reduced ballistic performance independent of tile edge length.

Given the lack of clear trend in performance with edge length, two representative square tile sizes were chosen for inclusion in the novel geometry designs: 40 mm and 20 mm edge lengths. The 40 mm edge length was chosen as it provided the best performance in the limited layered mosaic study and 20 mm was chosen as a typical size for similar topologically interlocking designs in the literature [85,87]. To allow for greater interlocking in those designs, an offset tile pattern was chosen over a square design. A final study was undertaken to determine if the aspect ratio of the tiles has an effect on ballistic performance (Table 4-2). These results led to the addition of a third representative tile-edge length of 30 x 60 mm, added to the list of those already chosen for inclusion in later designs.

Table 4-2: The residual velocity for non-square tiles for a range of aspect ratios.

Tile Edge Length (mm)	*Residual Velocity (m s^{-1})*	
	Square	*Offset*
5x15	323.9	388.7
8x12	351.6	380.3
10x15	365.2	342.1
10x20	374.2	350.6
10x30	346.5	343.8
15x20	373.0	352.4
15x30	323.9	358.3
15x45	358.7	355.7
20x30	354.0	341.1
20x40	377.4	349.9
20x60	350.1	350.4
25x50	345.1	353.1
25x75	363.5	361.9
30x45	367.8	339.4
30x60	323.4	330.8
35x70	358.7	337.0
40x60	341.1	342.6
40x80	343.3	346.0
45x50	325.4	348.0
50x75	348.2	340.0

4.6 SUMMARY

The parametric studies presented in this chapter have created a baseline monolithic ceramic armour and a greater understanding of the influences of the parameters relevant to a flat tile design. The results of these studies will be used to direct the basic design of more complex novel bio-mimetic architectures. The parameters and their associated values relevant to the computationally explored prototypes in the following chapters are total-thickness (7.5 mm), number of layers (3), tile pattern (offset mosaic) and tile edge length (40 x 40 mm, 20 x 20 mm and 30 x 60 mm).

The baseline armour, a 7.5 mm thick 250 x 250 mm monolithic ceramic tile, displayed a residual velocity of 209.6 m s $^{-1}$. This provides a standard of performance for future tiled armour designs to be compared against. It is clear from the results within this chapter that the introduction of interfaces in the through-thickness of an armour reduces performance, but this is necessary to the development of topologically interlocking materials. The challenge in the design of novel armour

system is to retain a single shot performance as close as possible to that of the monolithic ceramic tile of an equivalent areal-density whilst also exhibiting multi-hit capability.

CHAPTER 5 – A NOVEL ARMOUR DESIGN

5.1 INTRODUCTION

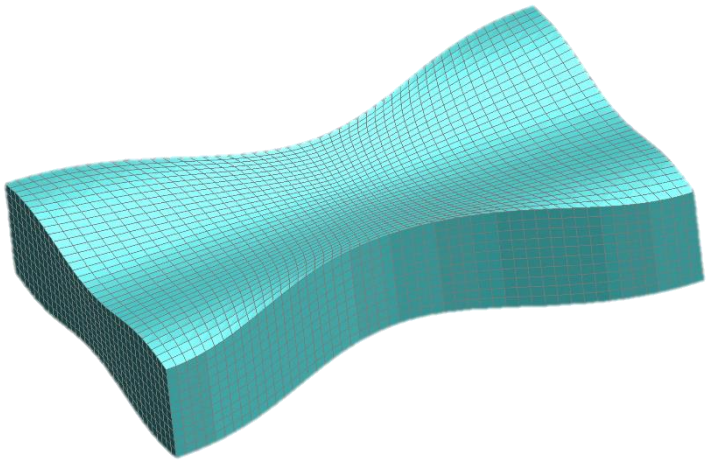

Figure 5-1: A single tile displaying some novel nacre-inspired design features

The previous chapter examined the design space for straight-edged tiles, including the effects of thickness, number of layers, impact location and tile edge length. The purpose of these studies was to lead into the design of a tiled system that can, by incorporating biologically inspired architecture, overcome the limitations of a monolithic armour. The most notable of which is limited multi-hit performance due to uninhibited crack growth creating a large damage zone that subsequently reduces ballistic performance after an initial impact [111,112]. The introduction of tiles is an obvious way to localise impact damage but is accompanied by an attendant localisation of the momentum from the projectile onto the user of the armour, resulting in greater propensity for behind-armour blunt force trauma [56]. Multi-layered tiled armours with a staggered overlapping layout could mitigate this momentum concentration and the inclusion of biologically inspired architecture could further increase both ballistic performance and momentum dissipation sufficiently to offset the reductions in those areas in the pursuit of multi-hit capability.

This chapter introduces a novel tile geometry based on the nanoscale lamellae architecture of nacre [113]. This new design introduces sinusoidally curved edges and the subsequent interlocking that can occur between adjacent tiles as a result of this shape, potentially allowing for greater momentum dissipation as well as minimisation of the damage zone (Figure 5-1). In this chapter, the ballistic performance against a single shot will be optimised as a minimum level of performance is required before multi-hit capability becomes a viable concept.

It cannot be assumed that design principles that apply at one length scale will continue to function well at another, e.g. expanding the nanoscale structure of nacre to a mesoscale tile armour, or that design analogies hold over different impact environments, e.g. low velocity collisions with sea debris compared to ballistic events. For this reason, the design space must be explored in each of its individual aspects to see how and if the expected toughening mechanisms and damage behaviours are occurring.

The process of developing the models used during this project was iterative and, in many cases, earlier models were repeated after later testing showed either direct issues with the formulation of the model or a need to expand their scope to properly inform the design choices at later stages. In some cases, this has led to residual velocities from one data set being incomparable to a later set and therefore most parametric studies are best construed as showing trends within only the data set discussed in that particular study rather than showing absolute results that are cross-comparable throughout. This is especially true given the sensitivity of FEA modelling of dynamic events to changes in the set-up of the model, such as the use of different element formulations or non-local material formulations.

5.2 DEVELOPMENT FROM EXISTING DESIGNS

Nacre itself consists of approximately hexagonal platelets with significant friction-based interlocking occurring between them to resist sliding during impact [114]. Previous designs based on nacre's platelet structure have therefore used an idealised tessellating hexagonal shape with a varying thickness to recreate this topological interlocking (Figure 5-2). The interlocking in these designs and in nacre itself oppose sliding in the plane perpendicular to the direction of a projectile impact. Other designs have been employed that use a trapezoidal shape to also induce interlocking to oppose movement in the direction of impact (Figure 2-24, [85]).

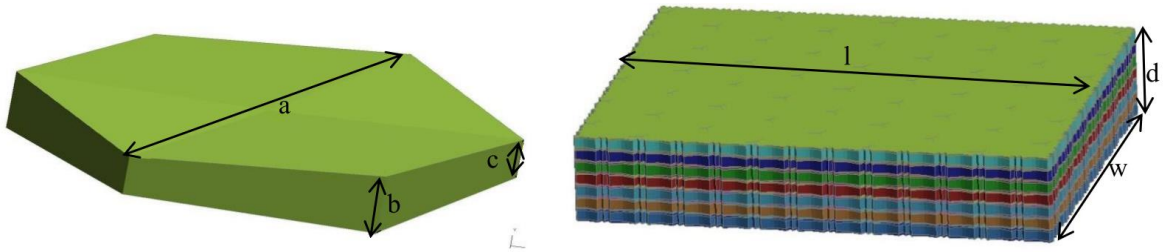

Figure 5-2: An existing hexagon-based topologically interlocking armour design showing the individual platelets (left) with dimensions a = 20 mm, b = 3 mm and c = 2 mm, and the platelets in the context of a full armour system of dimensions l = 127 mm, w = 100 m and d = 20 mm [115].

Building on this design, it was hypothesised that greater interlocking could be induced if the hexagonal tile was inverted, that is if the individual tile was cleaved in half between two corners and joined at the interface with a neighbouring tile (Figure 5-3). Starting with a flat hexagon this would tesselate easily but the introduction of any form of "waviness" requires careful consideration to ensure continued tessellation. This results in a "bow-tie" shape. The early base designs had dimensions of 20 mm x 30 mm and varied in thickness along the major axis of the tile from 4 mm to 3 mm. These dimensions were eventually changed to match those chosen in the previous chapter based on the results of further parametric studies. This required two different tile shapes in order to tesselate and have a continuous thickness along the surface of each layer in the tiled array: one shape that had a minimum thickness at the centre cross-section of the tile and reached a maximum at the tile edges, another with the opposite profile. This ensures that the rows, that are offset from neighbouring rows by half a tile -length, fit together with the variation in thickness.

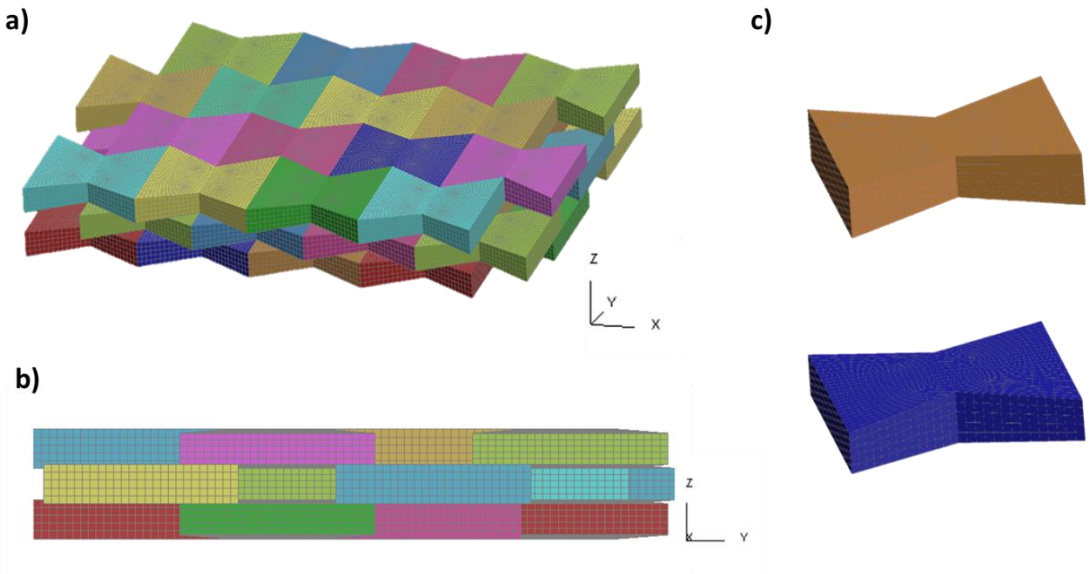

Figure 5-3: a) Early stage tile design showing the tiles in both a mosaic tile array and b) shown in cross-section. c) The tessellation requires two tile shapes in order for the tile thickness to be continuous across the surface of each layer.

It is clear that the geometric discontinuity in the centre of the bow-tie tile will lead to stress concentrations and earlier failure. The curve was therefore smoothed, and the edge profile replaced with a sinusoidal curve (Figure 5-4). The curve describing the through-thickness profile was also changed to a sinusoid as this both removed the surface discontinuity and allowed for a new tessellation pattern that requires only one tile shape, a feature that would allow for reduced costs in manufacture due to the need for only a single type of die during casting. During this sinusoidal

redesign, the variation in through thickness was also changed to align with the minor axis of the tile to avoid having the minimum tile width at the centre of the tile coincide with the minimum tile thickness. This could also have been avoided in the major-axis case by instead having the through-thickness increase from a minimum at the tile edges to a maximum at the centre, which will be explored using a "negative" value for A1 amplitude.

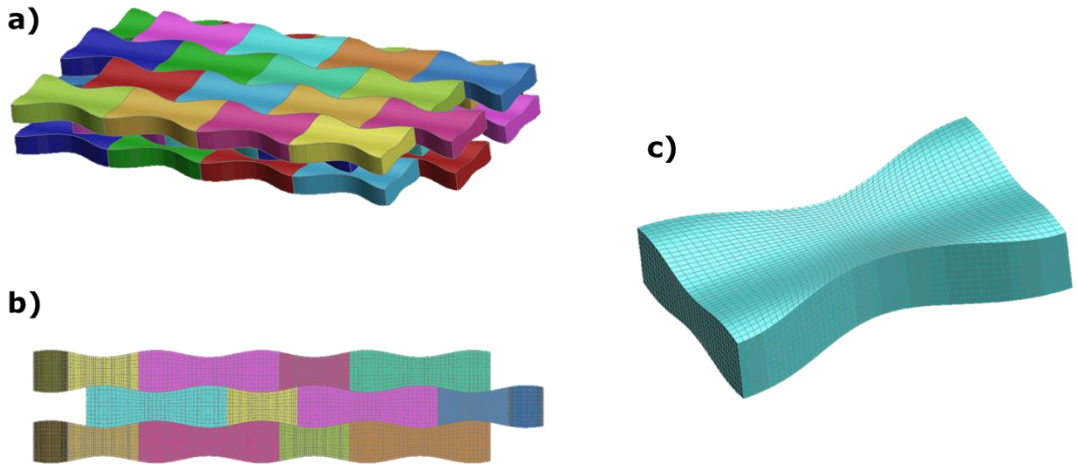

Figure 5-4: a) The sinusoidal bow-tie design shown in a tile array. b) The tile array shown in cross section looking along the major axis. c) A single self-tessellating sinusoidal tile.

In describing the geometry of these tiles there are five variables: width, length, thickness, A1 amplitude and A2 amplitude. A1 and A2 are the amplitudes of the sin-waves that describe the curved aspects of the tile surface (Figure 5-4). These will be described in greater detail in the later sections. The upper and lower exterior surfaces of the plates, i.e. those surfaces not in contact with other tile faces, are also flattened in the final design so as to maintain a constant total through-thickness and, therefore, areal-density (Figure 5-5).

There is the potential to introduce some form of edge chamfer or change in the orientation of the lateral surfaces of the tile to allow for further through-thickness interlocking in the manner introduced in biomimetic designs by Mirkahlaf [85]. Discussion of this geometric option is included later as, after an initial study into edge chamfers showed significant hour-glassing due to the element shape required, the inclusion of such a chamfer was abandoned.

In nacre, an important facet of the material is the inclusion of organic polymers between layers that add both cohesion between the layers and ductility during pre-interlock sliding. The effect of the inclusion of cohesive interlayers will be explored in the next chapter. The studies presented immediately following are focused purely on the effect of tile geometry on performance and focus

on finding any effect of changing the two variables A1 and A2 for the three tile sizes chosen in the previous chapter: 40 mm x 40 mm, 20 mm x 20 mm and 30 mm x 60 mm. Each tile is 2.5 mm in thickness and the total system is three-layered. A further surface feature, A3, is also introduced and explored.

5.3 A1 SURFACE VARIATION

A1 defines the maximum upper and lower surface deviation (Δz) and the upper curve is defined by:

$$\Delta z_{upper} = A1 \sin\left(\frac{2\pi}{W} x\right) \quad (5\text{-}1)$$

in which W is the tile width along the minor axis (oriented in the x-direction). Δz_{lower} is -Δz_{upper} as the two surfaces reflections with a plane of symmetry bisecting the tile in the xy-plane. Both the upper and lower curvature are only present in the middle of the three layers in the tile array. As noted, the externally facing upper and lower surfaces of the array are flat so as to maintain a constant total through thickness, this also serves to provide a more consistent ballistic performance for impact locations across the surface of the armour (Figure 5-5).

As in previous studies, the impactor is a simplified model of an AP M2 7.62 mm round with a velocity of 875 m s^{-1} and the armour systems are backed by a 20 mm thick polycarbonate plate. In this section, the term "A1" is used to refer to both the specific value for the amplitude of the surface feature described in Equation *(5-1)* and that surface feature itself.

For all three variables, a necessary criterion of the failure mechanics of this tiled armour design if interlocking is to affect ballistic performance is that the interlocking between tiles occurs over the timescale of a ballistic impact, i.e. $\lesssim 60\ \mu s$. The impact in these models is at the centre of the surface tile that is closest to the centre of the tile-array *en bloc* i.e. at the location indicated in Figure 5-5.

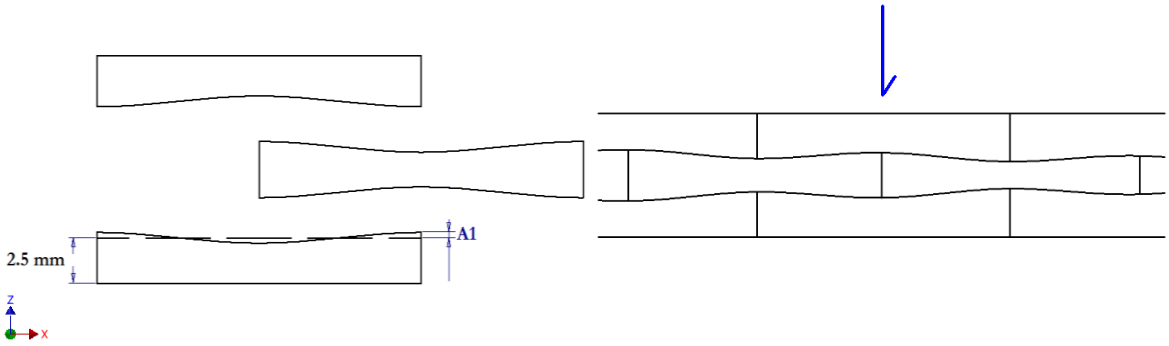

Figure 5-5: A representative schematic showing a cross-section of a the three tile orientations and geometries with non-zero A1 and these tiles as part of a tiled-system with the "centre" impact location indicated. Note that in the tile array the tiles are also offset by half a tile length in the direction perpendicular to the cross-sectional view with adjacent tiles both in-plane and between layers.

The results from this study suggest that the inclusion of A1, and the consequent change in through-thickness profile, causes a reduction in ballistic performance (Figure 5-5). For all three tile edge lengths, the general trend is a reduction in performance with increased amplitude of A1. For each differently sized tile array, the velocity of the projectile is reduced to by approximately 535 m s^{-1} ($\pm$5 m s^{-1}) for the flat surfaced tiles whereas a reduction of only 480 m s^{-1} ($\pm$5 m s^{-1}) is achieved for tiles with the maximum studied A1 amplitude of 0.5 mm. Only the 30 mm x 60 mm tile array exhibits a residual velocity lower than the baseline for any value of A1, with A1 = 0.1 mm reducing velocity by a further 19.8 m s^{-1} over the baseline. This suggests that low values of A1 might allow for frictional interlocking without incurring the significant reduction in performance that occurs at higher values.

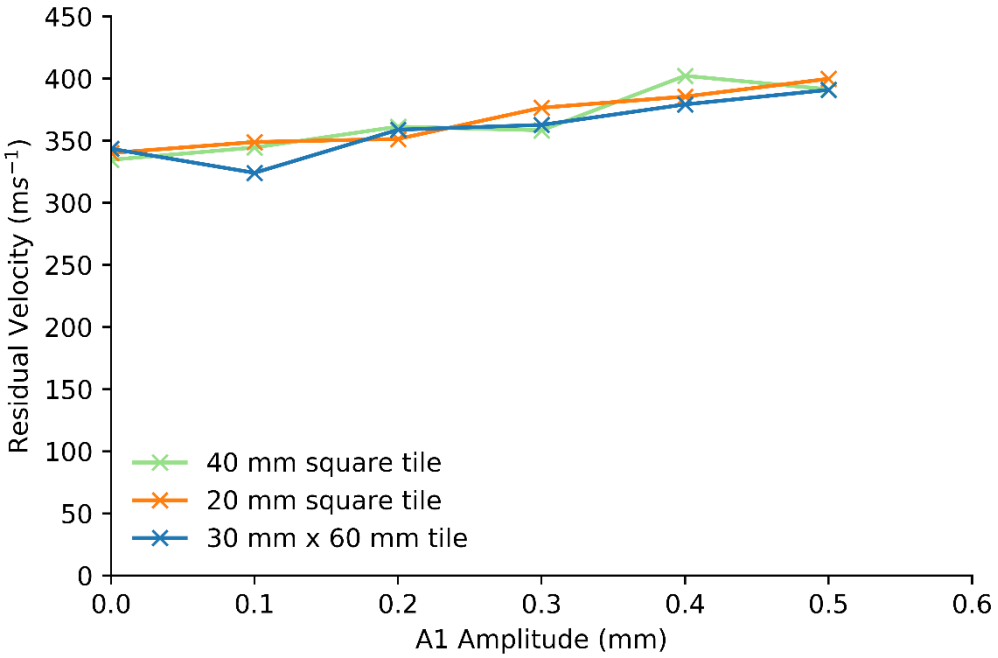

Figure 5-6: The effect of varying A1, the amplitude of the interlayer surfaces, on residual velocity for centred impacts.

It is likely that it is the change in through-thickness profile of the tile layers beneath the PoI that is the dominant factor in the observed trend. For the chosen PoI, i.e. the centre of an upper layer tile, increasing the amplitude leads to a thinner top and bottom layer while increasing the central layer. However, the central layer is impacted along a tile edge which is known to reduce performance by as much as ~20% for fully confined tiles (Table 4-1). Therefore, for centred impacts, the inclusion of A1 impairs the performance of the tiles struck in the optimal location for ballistic performance while increasing the dependence of the armour system on tiles impacted in a compromised location. The only exception to the above trend is for the 30 x 60 mm tile with an A1 of 0.1 mm for which the residual velocity is 20 m s^{-1} below that of the baseline (A1 = 0 mm) tile system.

This negative trend could be explained in terms of the optimisation problem discussed in research by Ben-Dor et al on the optimal arrangement of layers of differing densities and ballistic performance [60]. For any given layered system, the optimal arrangement of layers is to place the layer with the best ballistic performance (in terms of whichever aspect of ballistic performance that is being optimised) as the first layer that will be impacted by the incoming projectile. For a series of tiles with an A1 of 0, the top and bottom layers are identical and the middle layer, as it is being impacted on a tile edge, will have the lowest performance. The effect of increasing A1 therefore is to lower the ballistic performance of the top layer (and also the bottom layer) and

increasing the thickness of the tile at the lowest performing point, i.e. along a tile edge. As the total thickness (and therefore areal-density) of the system is constant, this change in through-thickness leads to an increase in areal thickness of material around the tile-edge, an area that has a lower ballistic performance per unit areal-density compared to centrally located ceramic material which is being reduced (Figure 5-9). The result of this exchange of areal-densities outweighs any influence that interlocking of adjacent tiles would give to ballistic performance.

Consequently, a series of models featuring an inverted surface profile were created, i.e. the tile being thickest at the centre and reducing to a minimum at the edges, still maintaining a consistent thickness at any point in x along the y-direction (Figure 5-7). The results for these tests are shown in Figure 5-8, note that the inverted profile is indicated with a negative value for A1 in order to distinguish the profile from the earlier described geometry. The interlocking observed in nacreous platelets will not occur in the same manner for such an interface profile, i.e. there is no resistance to tension via tile interlocking if applied from the edges of the system. However, there will still be resistance to movement in the x-direction due to friction and a normal contact force due to the irregularity of the interface profile.

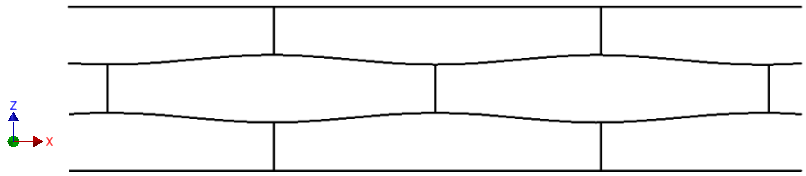

Figure 5-7: A representative cross-section of a tile-system with a negative value for A1.

For impacts on the centre of an upper surface tile, the inclusion of a surface profile with a negative A1 amplitude improves the ballistic performance (Figure 5-8). There is a clear performance increase with all three tile sizes showing improvements over baseline(A1=0) for an A1 amplitude of -0.1 mm. At this amplitude, the 40 mm tile improves by 4.5% and the 30 x 60 mm tile improves by 5.6% in terms of ballistic performance as measured by the reduction in projectile velocity. The 20 mm shows a 2.4% improvement. Each size of tile shows a different optimal value for A1, the best performance for the 40 mm tile is a surface profile with A1 = -0.1 mm. The 20 mm tile shows optimal performance with A1 = -0.2, reducing projectile velocity by 5% more than baseline and the 30 x 60 mm has an optimal performance at A1 = -0.3 with a 7.7% increase. The single best performing tile system over the combinations of A1 and tile edge length studied is the 30 x 60 mm tile with an A1 of -0.3, reducing the projectile velocity from 875 m s^{-1} down to 302.6 m s^{-1}.

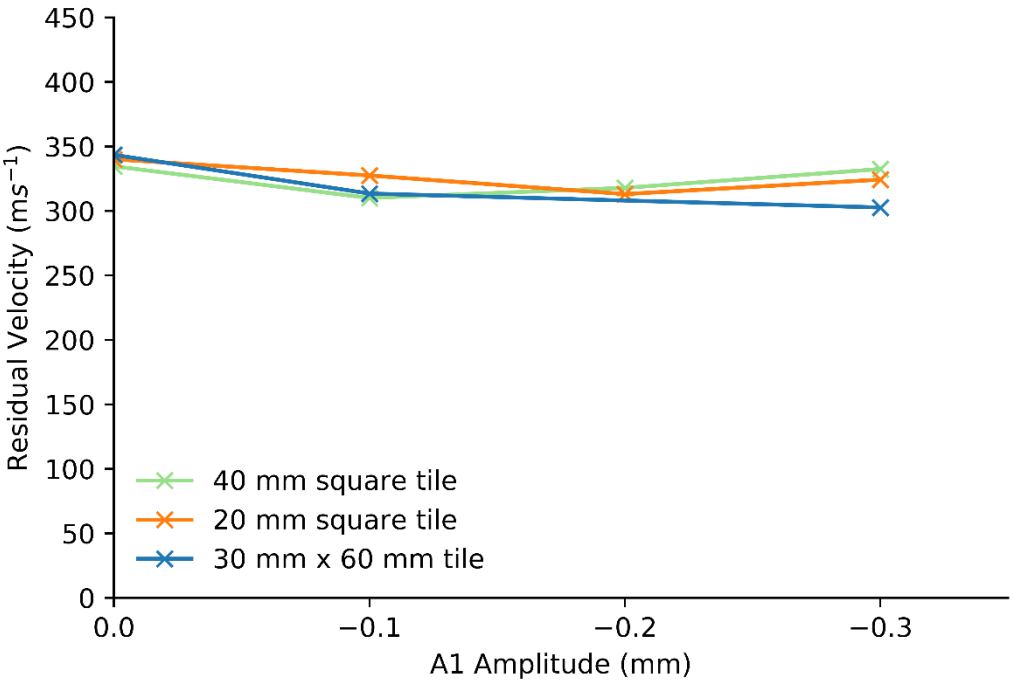

Figure 5-8: The effect on residual velocity of the inclusion of a surface profile with a negative value of A1 for tiles impacted at the centre of the tile system.

There is a very slight reduction in back-face deflection due to the change in surface profile associated with a non-zero A1 amplitude (Table 5-1). For the 40 mm tile set, the post-impact displacement of the back-surface of the polycarbonate backing is 2.27 mm. For increasing A1, the trend is a reduction in back-face deflection with an A1 of 0.4 mm showing a deflection of 2.02 mm. This could be a result of either interlocking causing momentum dissipation or the lower observed ballistic performance and the resultant reduction in momentum extracted from the projectile. The higher polycarbonate back-face deflection of the negative A1 amplitude tile sets, that had higher ballistic performance than the baseline set, suggest that it is a result of the difference in ballistic performance rather than an observed topological interlocking. The -0.3 mm A1 model does have marginally higher ballistic performance than the baseline (332.4 m s^{-1} vs 334.5 m s^{-1}) whilst also having a marginally lower backing deflection suggesting that interlocking may be inducing some momentum dissipation over the model. At high velocities, the compression shock waves induce much higher pressures across the model elements than any observed interlocking might and, as such, the local tile surface pressures cannot be observed for evidence of interlocking. In later models with inclusion of cohesive elements with more interrogatable output variables, interlocking may be discernible.

Table 5-1: Displacement of the lower/back surface of the polycarbonate backing at 50 μs after impact for the 40 mm tile length armour system for a range of A1 amplitudes.

A1 Amplitude (mm)	***0***	***0.1***	***0.2***	***0.3***	***0.4***	***-0.1***	***-0.2***	***-0.3***
Backing Deflection (mm)	2.27	2.16	2.17	2.16	2.02	2.39	2.38	2.24

After observing the results from central impacts on tiled systems with non-zero A1 amplitude, the study was expanded to observe the trend for a range of impact sites as the through-thickness profile of the armour is significantly different across the length of a given tile. To investigate this, for each centrally impacted value of A1 a model was impacted at an edge of the same tile i.e. keeping the same y-value but shifting W/2 in x and also at a point mid-way between this site and the centre; these impact sites will be referred to as edge and mid-point respectively (Figure 5-9). As shown in the previous chapter, ballistic performance at the edge is lower than that at the centre of a tile, however a lessening of this reduction in performance would be an advantage in the performance of a system as a whole as impact location in practice cannot be predicted or guided to the optimally performing areas of an armour system.

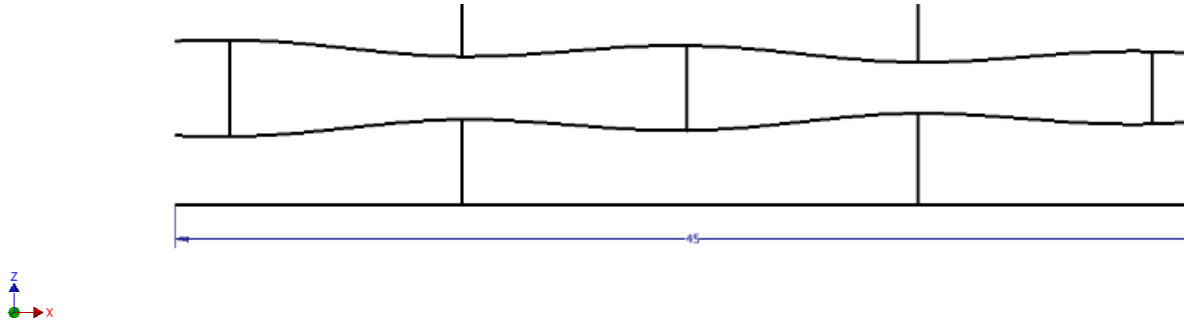

Figure 5-9: A representative schematic showing the site for the centre, mid and edge impact locations (blue, red and green respectively) in cross section for a tile system with a non-zero A1. Note that this cross-section is cut through the mid-point of a tile and that the impact represented by the blue arrow will hit the dead centre of the upper tile.

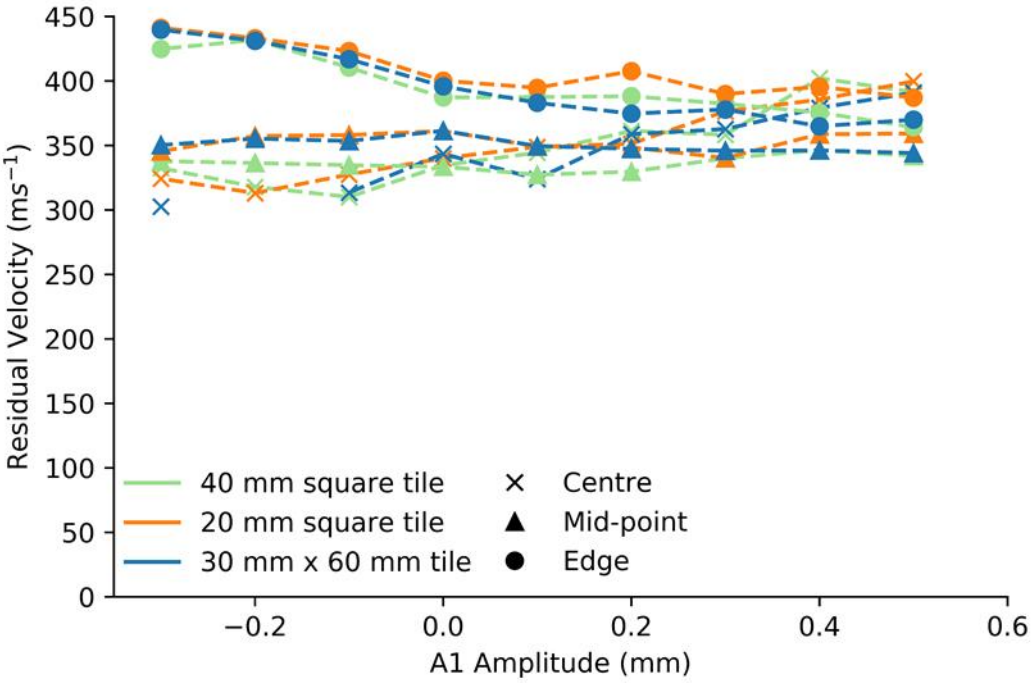

Figure 5-10: The effect of varying A1 amplitude for a range of impact locations on a range of tile edge length.

For the baseline tile sets, i.e. those with flat surface profiles, optimal performance occurs at the centre impact site, as expected, and decreases towards the edge with edge impacts performing on average 10.4% worse than centred impacts. As A1 amplitude is increased positively, the performance of the tiles impacted centrally decreases approximately linearly, in terms of increased residual velocity this line has a gradient of 130 ms^{-1}/mm. Edge performance, however, improves with increased A1 although by a much smaller amount compared to the loss in performance at the centre. As discussed previously in the context of the through-thickness profile at the centre, this

is a result of the increased thickness of the top-layer of the armour. This effect leads to an inversion of performance across all tile edge lengths such that, for A1≥ 0.3, ballistic performance at the tile edge is greater than that at the centre.

For negative amplitudes of A1, the trade-off in performance at the tile edge is much greater. Although centred performance increases above baseline, tiles impacted at the edge perform poorly. All tiles sets exhibited greater performance for centred impacts, with the greatest improvement in the 30 x 60 mm tile set with an A1 of –0.3 mm reducing residual velocity to 302.6 m s^{-1} down from 343.4 m s^{-1} for the equivalent size baseline set. The location dependence of the ballistic resistance is, however, increased for negative values of A1 due to the reduction in thickness of the first layer away from the centre where the ballistic performance is concurrently compromised by the proximity to the tile edge. This inhibits the utility of such an armour however it does suggest that tiles with an increased upper layer thickness offset by thinner lower layers to maintain total thickness, could improve performance for a fixed areal-density. This would be an interesting area for future work.

The lateral spread of the post-impact damage pattern is not significantly affected by changes in through-thickness tile geometry and is solely dependent on the layout of the mosaic tiles (Figure 5-11). All impacts show strong cracks developing in line with the mesh direction. Diagonal cracks develop earlier in the A1= -0.3 mm tile set, possible due to thinning towards the tile edges. Where nearer tile edges interrupt crack propagation in 20 mm square tile sets earlier than in 30 x 60 mm tiles, the damage shifts and accumulates at tile corners. Further, damage away from the impact site caused by reflection of the compressive shockwave at lateral interfaces is visible in the 20 mm square tiles. This is because the interfaces causing the reflections are closer for smaller tiles resulting in greater damage volume earlier in the impact event. Within each layer the spread of damage is consistent across differing values of A1 with only minor differences in total damage volume due to the differing thicknesses of the lateral damage patterns (Figure 5-12). The damage caused by the reflected wave from the back surface can be seen in this figure and is also largely unaffected by changes in the through-thickness profile. This is likely due to the stresses caused by compressive shockwave for impacts at velocities of this magnitude being sufficiently high to still exceed the damage criteria for the ceramic.

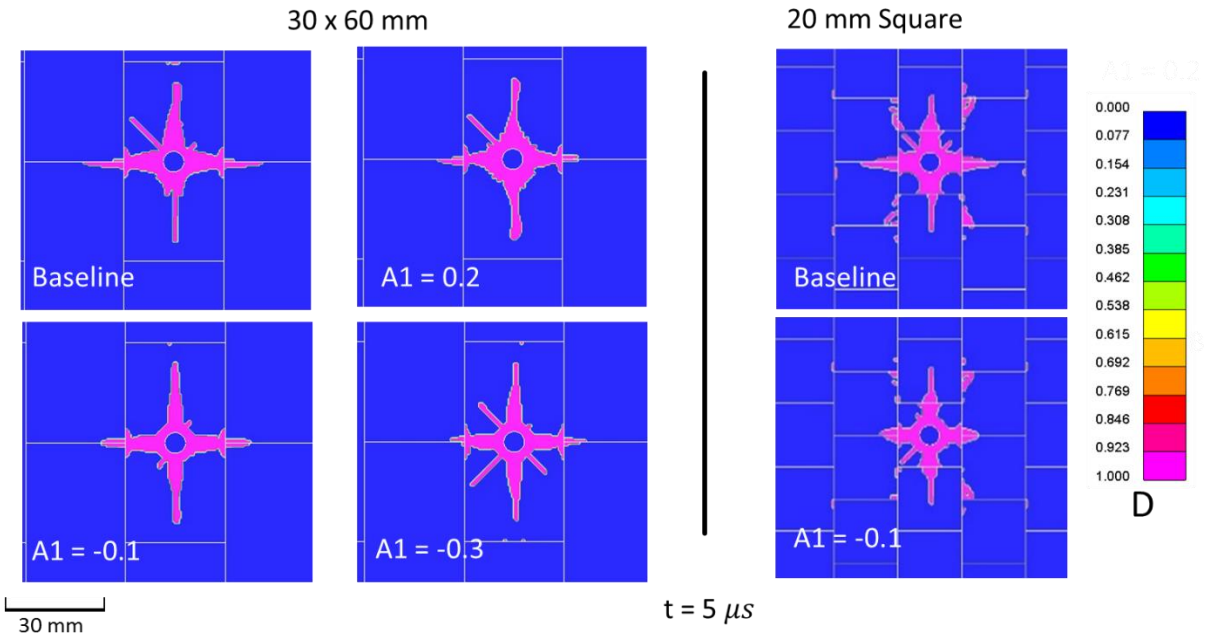

Figure 5-11: A top-down view of the damage (5 μs post-impact) on the upper surfaces of 30 x 60 mm and 20 mm square tile sets of differing A1 surface profiles (A1 shown in millimetres).

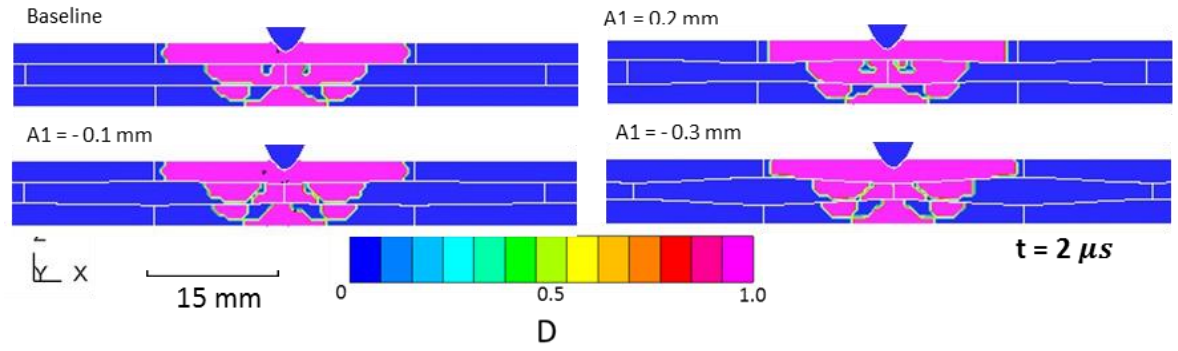

Figure 5-12: A cross section of tiles (30mm x 60mm) of varying A1 amplitude at the PoI. The lateral damage spread is constant across all layers independent of A1, however the tile surface profile affects the thickness of these lateral damage patterns and therefore total damage volume.

Observing the stress wave propagating from the impact site, it is detectably affected by the through thickness profile and is therefore likely the predominant factor explaining the difference in residual velocities for differing values of A1. The peak stresses (P_{MAX}), 2 μs after impact, in the ceramic material beneath the PoI for tiles with A1 values of -0.3mm, -0.1mm, 0 mm and 0.2 mm are 4.316 GPa, 4.942 GPa, 5.056 GPa and 5.118 GPa (Figure 5-13). This time stamp occurs during the initial dwell phase of the impact that lasts ~ 3 μs for this thickness of alumina and during which time ballistic performance is particularly sensitive to the dynamics of stress wave propagation [51].

These peak stresses occur at the upper surface of the second layer suggesting it is the result of the build-up of pressure as the impact shockwave crosses the boundary interface and propagates as a Hertzian cone. The observed "split" in the area of peak stress is due to the presence of a tile edge dividing the second layer at that point. The reduced peak stresses in Figure 5-13 correspond to reduced residual velocities for the same tiles (Figure 5-6, Figure 5-8). There are two contributing factors to the reduction in pressure with decreasing values of A1. The first is the consequent increase in thickness of the uppermost tile under the "centre" impact site. The first interlayer boundary is closer to the surface for the A1=0.2mm tile than the A1=-0.3 mm tile and, as such, there is less dissipation in pressure as the shockwave travels out from the PoI. Secondly, there is also a greater contact surface for the A1=-0.3 mm tile across this interface than for all higher values of A1. This spreads the area over which the pressure is applied and causes a wider "origin" for the shockwave as it is initiated in the second layer. Both factors act to reduce the peak pressures experienced by the ceramic material during the critical dwell phase of the impact event. This occurs as the material damage parameter goes to 1.0 throughout the material, as indicated in Figure 5-12 showing the same perspective and time stamp as Figure 5-13.

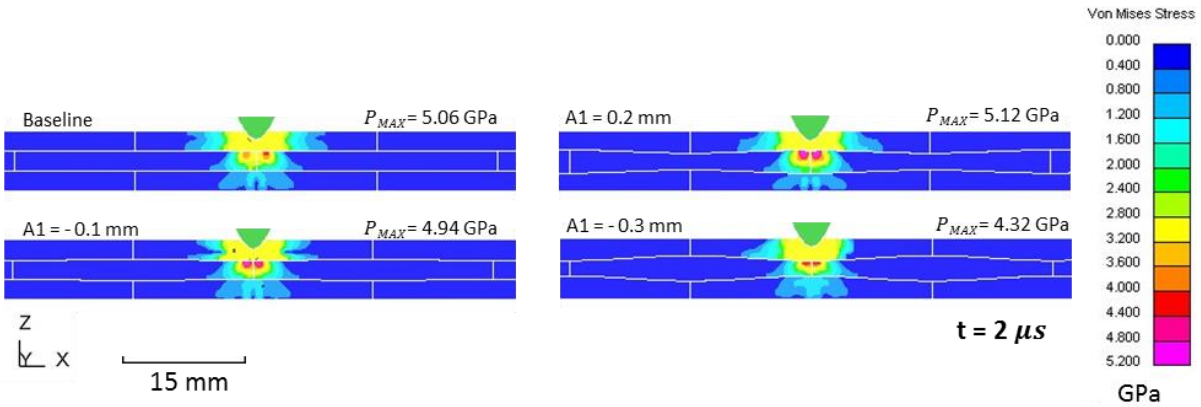

Figure 5-13: A contour plot showing the stresses in the ceramic cross-section beneath the PoI for a range of A1 values for 30mm x 60mm tiles.

5.4 A2 Lateral Surface Variation

A2 defines the maximum deviation on the "side" surfaces of the tile (Δx) and denotes a change in the total width of the tile at a given point along the y-direction (the major axis of the tile). The curve for the deviation on the right-side of the tile is given by:

$$\Delta x_{right} = A2 \sin\left(\frac{2\pi}{L} y\right) \qquad (5\text{-}2)$$

in which L is the length of the tile in the major axis (oriented in the y-direction). Δx_{left}, i.e. the shift in x on the left side of the tile as a function of distance in y, is a reflection of this line in a plane of symmetry, parallel to the yz-plane, bisecting the tile in x (Figure 5-14).

For both the 40 mm and 30 mm x 60 mm tiles, the inclusion of a small ($\leq$ 0.25 mm) non-zero A2 amplitude slightly improved ballistic performance (Figure 5-15). The greatest improvement occurring at 0.1 mm amplitude for both, with the 40 mm tile set lowering residual velocity a further 7.6 m s^{-1} (an improvement of ~1.4%) while, for the 30 mm x 60 mm tile, the change in lateral surface profile lowered the projectile velocity by a further 22.0 m s^{-1} (a 4% improvement) compared to the baseline tile sets.

Subsequent increases in the amplitude of A2 beyond 0.25 mm led to a reduction in performance and an increase in residual velocity across all tile sizes, with no improvements for any A2 amplitude observed in any of the 20 mm edge length tile sets. The reduction in performance is likely due to relief waves reflected from the nearest lateral surfaces arriving sooner with higher A2 as the tile sides are brought closer to the impact site and the resulting reduction in yield stress of the ceramic as the accumulated hydrostatic pressure is relaxed. By including A2 there is also an increase in the total length of the edges of each tile (in the x-y plane) which could lead to a greater cross-section of the impacted tile being subject to edge effects that are detrimental to ballistic performance.

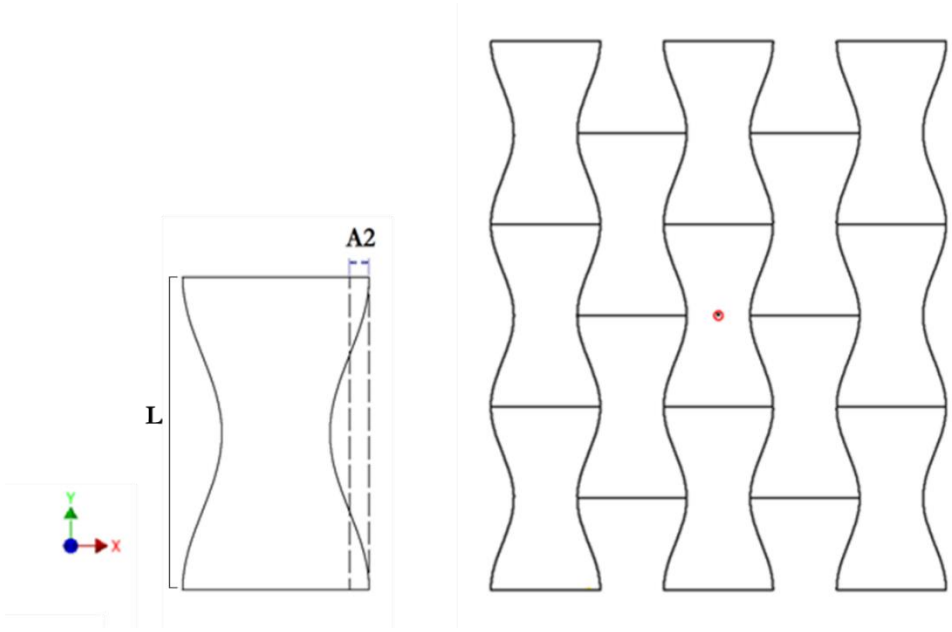

Figure 5-14: A representative schematic showing, in plan-view, (left) a single tile with a non-zero A2 amplitude and (right) an arrangement of tiles with a non-zero A2 amplitude, impact site indicated in red. Note that number of tiles in the x and y directions is dependent on tile edge length designed to fit, with overlap, over a 250 x 250 mm area.

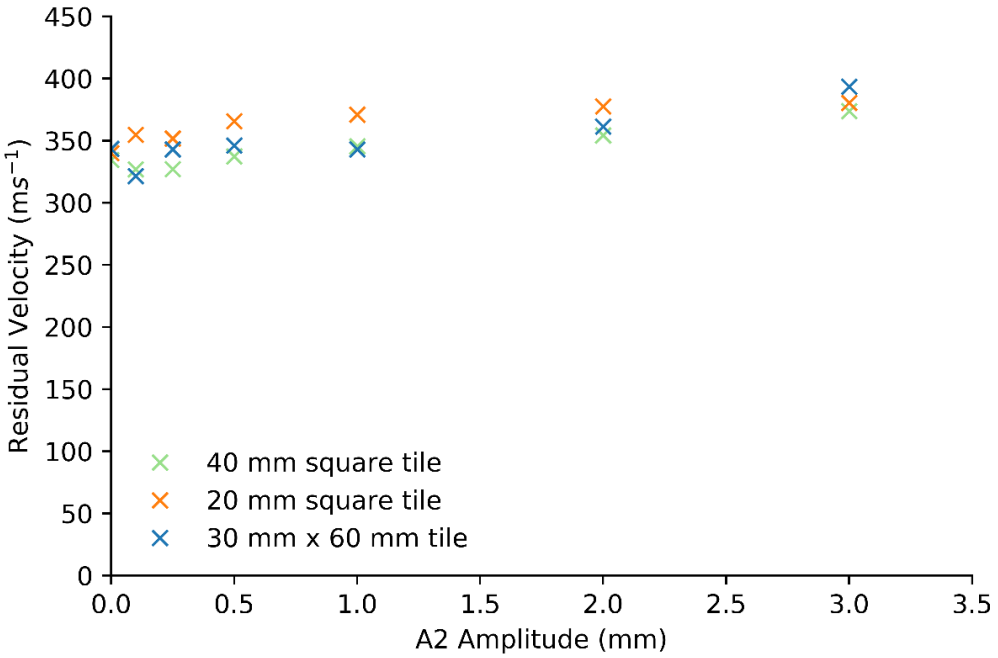

Figure 5-15: The change in residual velocity as a result of changing the amplitude of A2, the surface profile of the lateral sides initially parallel to the y-axis (with z being the direction of impact).

The improvement in ballistic performance over baseline for low values of A2 is a result of changes to the pressure waves after impact, this same explanation holds for the loss in performance at higher A2. Focussing on three 30 x 60 mm tile sets, (baseline, A1=0.25 mm and A1=3 mm), the underlying stress wave patterns appear to correlate with observed ballistic performance. Although the stress wave pattern looks similar for the initial 4 μs of the impact event, by 8 μs there is a noticeable divergence both in pattern and in peak stress between baseline, A1=0.25 mm and A1=3 mm tile sets (Figure 5-16). The peak surface stresses at this time also correlate with the residual velocities for each tile set with the highest peak stress observed for the A2 = 3 mm tile set which has the highest residual velocity of these three tile sets. Unlike changes in A1 amplitude, changes in the lateral interfaces of the tile caused by A2 cause noticeable changes to the pattern of damage accumulation in the model (Figure 5-17). The curved surfaces caused by higher A2 amplitudes introduce further crack diagonally away from the impact site, adding to those in the major axis of the tiles. At the same timestamp (8 μs), there is also greater damage volume in the impacted tile itself for higher values of A2 in comparison to flat sided tiles.

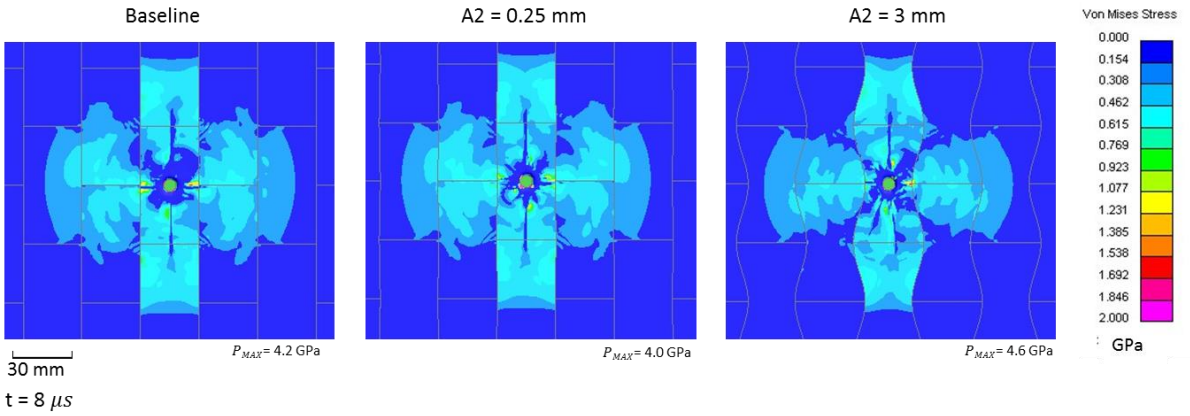

Figure 5-16: Stress wave patterns for three 30 x 60 mm tile sets of increasing A2 amplitude. The contour limits are gated below the maximum stress to increase the visibility of the surface stresses.

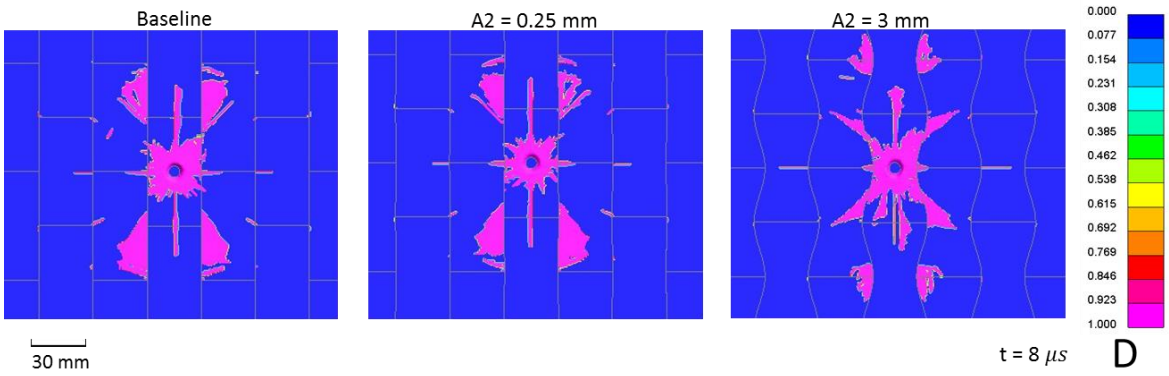

Figure 5-17: The damage patterns for three 30 x 60 mm tile sets of increasing A2 amplitude.

A consequence of the finite element mesh used in these models is that the element size is reduced around the impact site for increasing values of A2 as the total number of elements in the x-direction is kept constant while the distance across the mid-section of the tile is reduced by A2 (Figure 5-18). At the tile edges this effect is reversed, i.e. larger element sizes, as the effect of A2 is to broaden the tile at those points. As noted in earlier convergence studies, smaller element size leads to a higher residual velocity in ballistic impact models. This effect should be minimal as the approximate element size was chosen to mitigate the sensitivity of the mesh response to changes in element size, however without further work it cannot be excluded as a confounding factor. For this reason, the results of higher amplitude A2 meshes are not included in Figure 5-15 in cases where, as for A2 amplitudes above 3 mm, the change in element size exceeds 30%.

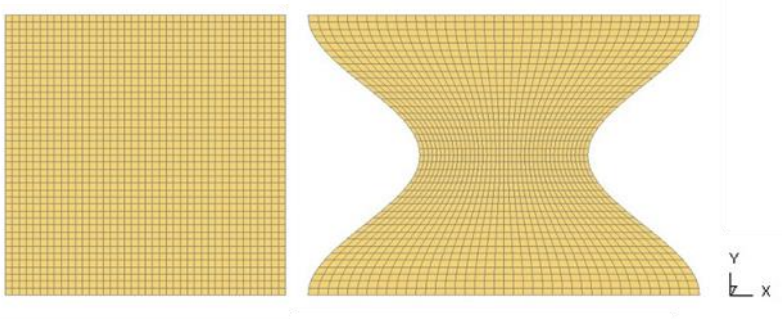

Figure 5-18: A comparison of the element sizes at the impact location of a 20 x 20 mm tile at the baseline (left) and with A2 = 4 mm (right).

5.5 A3 SURFACE VARIATION

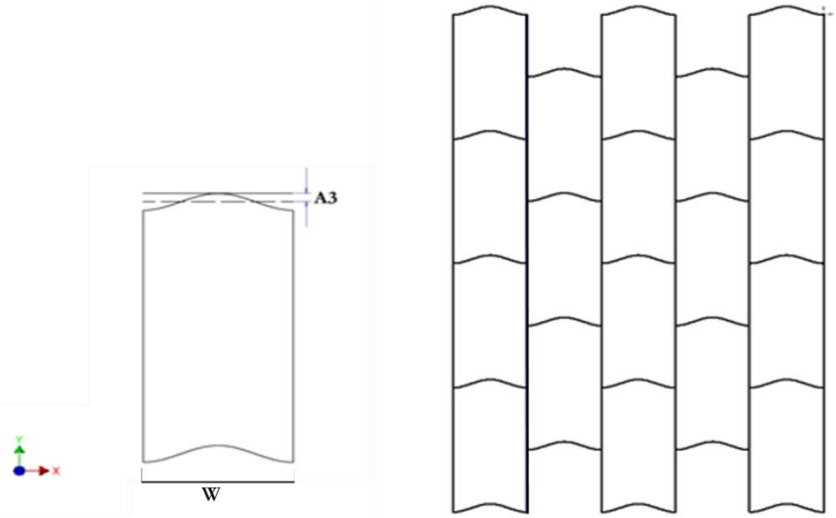

Figure 5-19: Top-down view of a representative tile with a non-zero A3 amplitude (right) and shown in-situ as part of a tile array.

Further to the two surface features described, a third design feature for the remaining flat lateral surfaces is proposed to maximise interlocking. The flat surfaces at the ends of the tile are given a profile shifted in the y-direction (i.e. the major axis) and described by the curve:

$$\Delta y = A3\left(1 - \cos\left(\frac{2\pi}{W}\, x\right)\right). \qquad (5\text{-}3)$$

The change in the geometry of the tile described by a change in the amplitude A3 are applied to the edges at the "front" and "back" of the tile, i.e. the surfaces parallel to the x-axis (Figure 5-19). This curve is applied to both these surfaces similarly and not symmetrically applied as for the other surface profiles, so as to maintain a single tile shape for tessellation.

In order to minimise the sensitivity of these results to the mesh, A3 was implemented into the meshing program to shift the y-coordinate of nodes at the front and back edges of the tile but for the shift to not occur for nodes at the centre of the tile (Figure 5-21). This ensures that the mesh at the impact site of the tiles, i.e. the centre, is not subject to change with A3 when moving from the baseline tiles to geometries with a non-zero A3. This was achieved by applying a coefficient of $1 - \sin\left(\frac{\pi y}{L}\right)$ to the application of Equation *(5-3)*, assuming that the tile front is located at y = 0 and the tile back is at y = L.

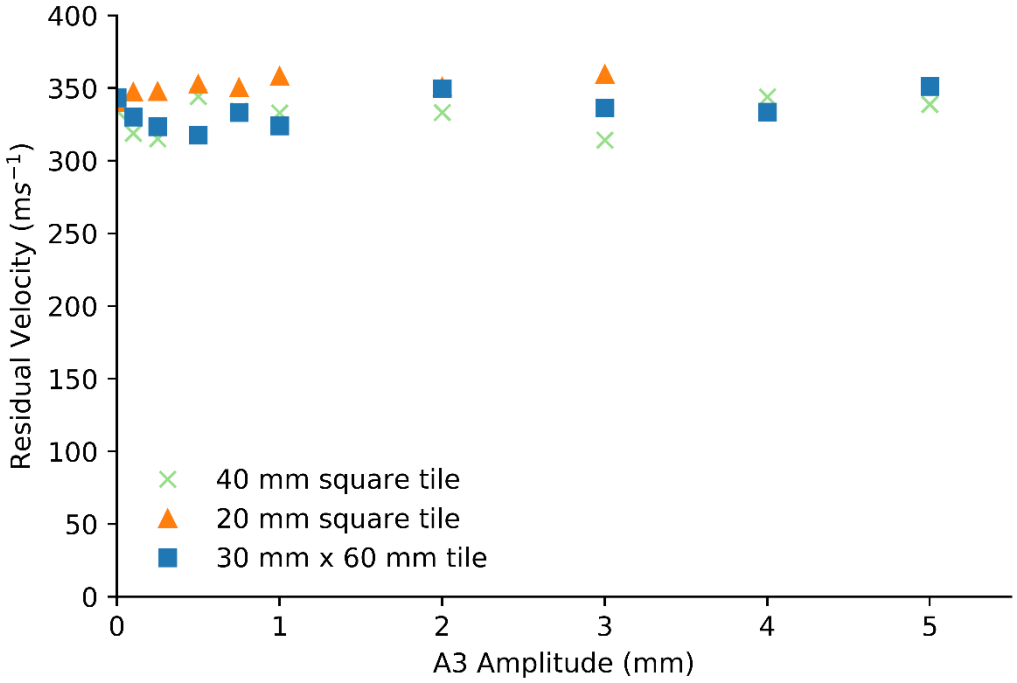

Figure 5-20: The change in residual velocity after a 875 m s $^{-1}$ impact as a result of changing the amplitude of A3, the surface profile of the front and back lateral sides initially parallel to the x-axis (with z being the direction of impact).

As in A2, only centred impacts were modelled for A3. As seen in A2, there are no observed amplitudes of A3 for which the 20 mm square tiles displayed an improvement over baseline. However, both the 40 mm square tiles and the 30 x 60 mm tiles showed improvements for smaller values of A3 and subsequent reductions in performance as the amplitude is increased. In the 40 mm tile sets, both 0.1 mm and 0.25 mm amplitudes showed improved performance with residual velocities of 319 m s^{-1} and 315.2 m s^{-1} respectively, in comparison to the baseline target of 334.5 m s^{-1}. Explanations for this behaviour mirror those posited for the trends observed with changing the A2 amplitude. For values of A3 greater than 0.25 mm, ballistic performance was slightly reduced although the overall trend is that it has near negligible effect.

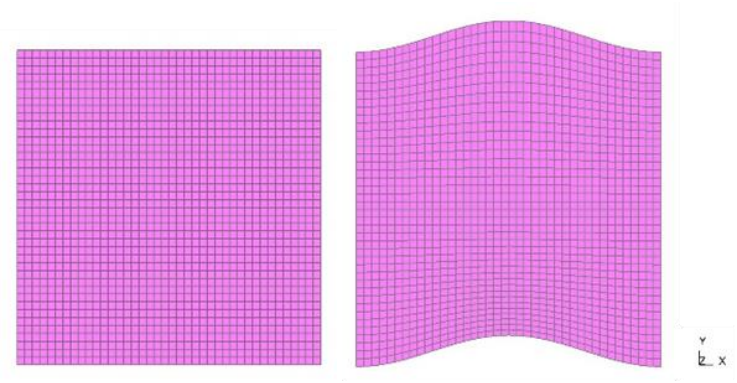

Figure 5-21: The mesh of a baseline tile (left) in comparison to the shifted mesh of a tile with an A3 of 1 mm (right), showing that the mesh at the centre of tile has cuboid elements undistorted by the y-shift introduced by A3.

5.6 OPTIMAL TILE GEOMETRY

A combination of the highest performing amplitudes for each feature in isolation may lead to a further optimised design. Based on the studies of the three geometric features proposed for the tile shape, a number of A1, A2 and A3 amplitudes were chosen for each tile size that exhibited improvements in performance over the baseline tile sets. For the 40 mm square tile sets the amplitudes that led to optimal performance in their respective studies were A1 = -0.1 mm, A2 = 0.25 mm and A3 = 0. 25 mm. For the 30 x 60 mm tile sets, two amplitudes of A1 were chosen representing the best performing positive and negative amplitudes. Therefore, the optimally performing amplitudes in isolation for this tile set are A1 = {-0.3,0.1} mm, A2 = 0.1 mm and A3 = 0.5 mm. For the 20 mm square tiles, the only improvement in performance occurred by the introduction of the A1 surface profile and all other geometric variations led to a reduction in performance. The 20 mm square tile, therefore, has an optimal geometry with A1 = -0.2 and A2=A3=0. These optimal amplitudes, having been observed in isolation, were then examined in all possible combinations, included zero amplitude variations of each option. The results, as well as the combinations of parametric options used, are presented in Table 5-2. When referring to specific tile sets within this series a naming convention of *(A1, A2, A3)* is used, e.g. the 40 mm Square tile (-0.1, 0.25, 0.5) tile set refers to a tile set with A1 = -0.1 mm, A2 = 0.25 mm and A3 = 0.5 mm.

Table 5-2: The residual velocity for tiles with optimised A1, A2 and A3 geometric surface profiles in combination.

	A1 (mm)	A2 (mm)	A3 (mm)	RESIDUAL VELOCITY (m s^{-1})
20 mm SQUARE TILES	0	0	0	340.0
	-0.2	0	0	313.0
40 mm SQUARE TILES	0	0	0	334.5
	0	0	0.25	327.1
	0	0.25	0	327.1
	0	0.25	0.25	320.7
	-0.1	0	0	310.0
	-0.1	0	0.25	320.1
	-0.1	0.25	0	310.5
	-0.1	0.25	0.25	326.2
30 X 60 mm TILES	0	0	0	343.4
	0	0	0.5	317.6
	0	0.1	0	321.4
	0	0.1	0.5	308.8
	0.1	0	0	324.0
	0.1	0	0.5	346.5
	0.1	0.1	0	334.8
	0.1	0.1	0.5	350.5
	-0.3	0	0	310
	-0.3	0	0.5	324.4
	-0.3	0.1	0	323.6
	-0.3	0.1	0.5	317.5

The optimally performing tile set is the 30 x 60 mm (0, 0.1, 0.5) tile set with a residual velocity of 308.8 m s^{-1}. This tile set outperforms all other three-layer tile systems of this thickness. Note that the comparative baselines for the 7.5 mm thick monolithic ceramic block that exhibits a residual velocity of 209.6 m s^{-1} and the three-layered 250 mm square tile system, i.e. a single large tile per layer, that has a residual velocity of 329.2 m s^{-1}. The performance of these incremental geometric improvements should be considered in the context of this baseline for ballistic performance, with the aim of achieving greater multi-hit performance with only a minimal reduction in single shot performance.

A small number of the geometric features that improved performance in isolation lead to an increase in residual velocity when combined. For example, the optimally performing tile set in this series, the 30 x 60 mm (0, 0.1, 0.5) set performed worse than baseline with the inclusion of an A1

of 0.1 mm into the geometry, leading to an increased residual velocity of 350.5 m s^{-1}. Observing the von Mises stress during impact, the (0.1, 0.1, 0.5) set is subject to a peak stress of 4 GPa whereas the equivalent tile geometry with A1 = 0 experiences a peak of only 3.56 GPa. The interactions between reflected shock waves leading to these stress peaks is highly dependent on the surface geometry of the reflecting interfaces and, further, they are unpredictable without numerical interrogation.

5.7 SUMMARY

For most values of A1, A2 and A3, there is no clear improvement in ballistic performance and, especially in the case of A1 and A2 there is considerable reduction in performance at higher values. All optimal geometries have sub-mm geometric variations that have approximately-square sides but with some slight deviation to allow for friction and topological interlocking between tiles as well as the disruption of reflected wave patterns. These possible mechanisms will be investigated with the inclusion of an interlayer cohesive layer that will serve to increase the effects of the first two possible mechanisms of performance improvement and aid in discerning the underlying behaviour leading to the ballistic improvements observed.

The next stage in development of this armour system is the addition of a cohesive layer between the tiles. The following tile sets from the above series of simulations chosen to represent the optimally performing geometries and to explore the effect of a cohesive layer on the performance of tile geometries of slightly different design (e.g. negative vs positive A1): 20 mm square tile sets (0, 0, 0) and (-0.2, 0, 0), 40 mm square tile sets (0, 0, 0), (-0.1, 0 ,0) and (-0.1, 0.25, 0) and 30 x 60 mm tile sets (0, 0, 0), (0, 0.1, 0.5), (-0.3, 0, 0) and (-0.3, 0.1 ,0.5).

CHAPTER 6 – COHESIVE INTERLAYERS

6.1 INTRODUCTION

Having studied the effects of varying the geometry of these tiled systems to mimic some facets of the topologically interlocking design of nacre, the design space of this armour system is further expanded to explore the effect of the inclusion of a cohesive interlayer in combination with these geometric aspects. Nacre is ~95 vol% aragonite (calcium carbonate) and ~5 vol% is composed of a ductile interlayer organic polymer (Figure 6-1) [116]. This ductile layer acts as an adhesive between the platelets increasing the tensile strength of the nacre and allowing for the visco-plasticity exhibited during the application of tensile stress [117]. To mimic this in the current armour design, a cohesive interlayer of epoxy resin is added between the layers of ceramic tiles for the set of optimal tile geometries identified in Chapter 5. These geometries are the 20 mm square tile sets with A1, A2 and A3 amplitudes of (0, 0, 0) and (-0.2, 0, 0), the 40 mm square tile sets with amplitudes of (0, 0, 0), (-0.1, 0 ,0) and (-0.1, 0.25, 0) and the 30 x 60 mm tile sets with amplitudes of (0, 0, 0), (0, 0.1, 0.5), (-0.3, 0, 0) and (-0.3, 0.1 ,0.5) [using a naming convention of (*A1,A2,A3*) with each amplitude given in millimetres]. In addition, a further 30 x 60 mm tile set with amplitudes of (0.1, 0, 0) is included to represent a set with a positive A1 aspect. All tile sets are, as in Chapter 5, three-layered. A three-layered 250 mm square tile set with no off-set and flat surfaces, i.e. a single tile per layer, is also included as a baseline for comparison.

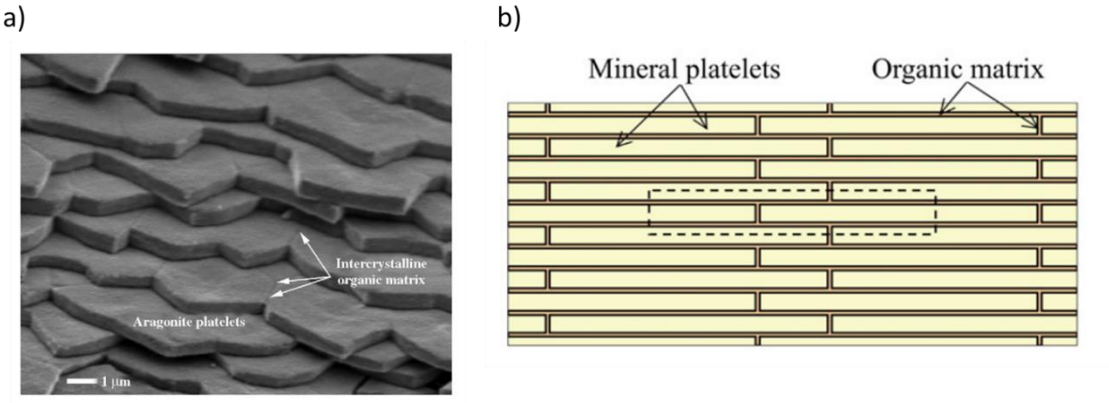

Figure 6-1: a) An SEM image of the microstructure of nacre showing the platelet configuration and location of the organic polymer matrix [Adapted from [118]***]. b) A representative schematic showing the platelet and cohesive matrix structure in cross-section [Adapted from*** [119]***].***

6.2 COHESIVE MATERIAL MODEL AND MESH

These models build on those described previously and feature a simplified 7.62 mm AP M2 projectile model impacting on a 250 x 250 mm area of ceramic tiles in three 2.5 mm thick layers

and backed by a 20 mm thick polycarbonate backing (Figure 3-14). The 0.001 mm gaps between the layers, previously empty, are now filled with a thin layer of cohesive elements (Figure 6-2). The material properties for the polycarbonate backing, steel alloy projectile and alumina ceramic tiles are as presented in Table 3-3 and Table 3-6.

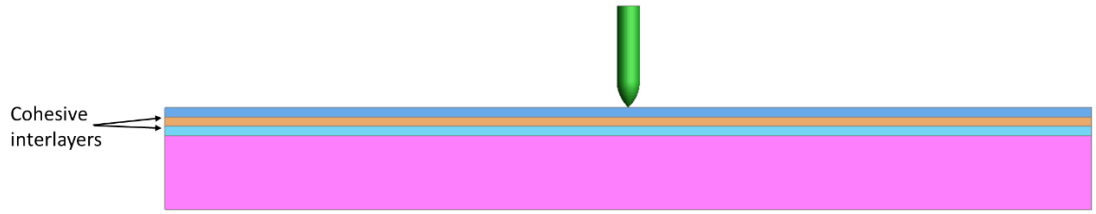

Figure 6-2: The location of the cohesive interlayers inserted between layers of ceramic tiles.

The cohesive interlayers are meshed as 8-node cohesive interface elements and are a single element in through-thickness. In-plane, these elements have sides 0.5 mm in length, a similar mesh density as the surrounding tile mesh. Through-thickness, they are 0.001 mm thick (i.e. the gap between ceramic layers). The contact between cohesive and ceramic uses *CONTACT_TIED_NODES_TO_SURFACE, tying the nodes of the cohesive element with a segment-set coated on the nearest ceramic upper or lower surfaces. No contact is implemented between the projectile and the cohesive layers. The mesh is 250 mm x 250 mm in the x-y plane with variations in z to match the interlayer surface profiles. Due to the offset of tiles, this leads to some cohesive elements that are not attached to ceramic elements and vice-versa at the boundary of the armour system (Figure 6-3). However, this is sufficiently distant from the PoI as to have minimal effect on the observed impact behaviour. The interlayer is deformed to match the contours induced by a non-zero A1 amplitude.

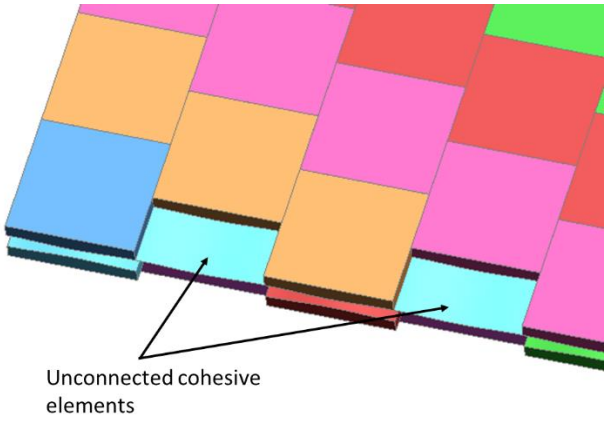

Figure 6-3: Some cohesive elements are unconnected to ceramic tiles at the boundary due to the layout of the tiles.

The cohesive elements use LS-DYNA's element formulation type 19, a 4 integration-point cohesive element. This formulation creates a mid-surface in the cohesive element defined by four integration points midway between each of the nodal pairs 1-5, 2-6, 3-7 and 4-8 as labelled in Figure 6-4. This surface defines the local co-ordinate system of the cohesive for the mode I and mode II material responses.

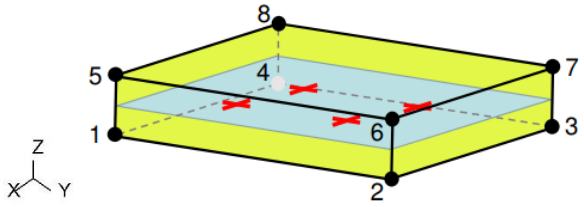

Figure 6-4: The node numbering of a cohesive element showing a mid-surface created based on the nodal connectivity of a solid element [Adapted from [120]***].***

The material model used for the cohesive is a user-defined mixed-mode delamination model developed at the University of Bristol referred to as Bristol's Cohesive Zone Model [121]. This model uses a strength-based damage criterion to determine the point at which mixed-mode crack initiation occurs and was chosen as it has been well validated experimentally [121,122]. The overall response is determined by a bi-linear traction separation law (Figure 6-5). Using the co-ordinate system illustrated in Figure 6-4, the positive nodal displacement in z, $\delta_{z,}$ defines the normal opening displacement, δ_I, and the displacement in the resultant shear direction is

$$\delta_{II} = \sqrt{\delta_x^2 + \delta_y^2}. \qquad (6\text{-}1)$$

The mixed-mode relative displacement is derived from these displacements and defined as

$$\delta_m = \sqrt{\delta_I^2 + \delta_{II}^2}. \tag{6-2}$$

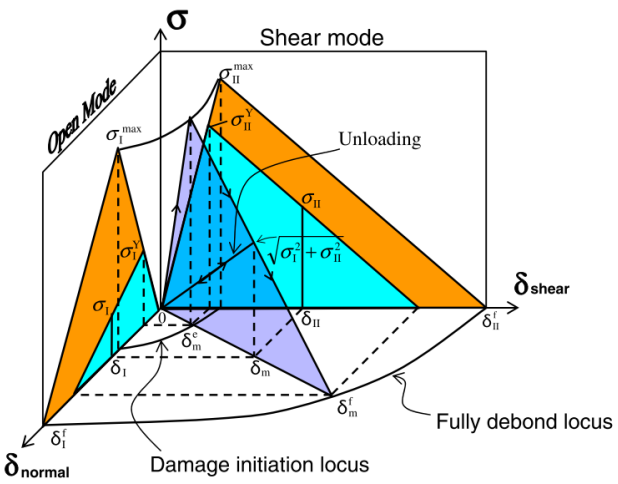

Figure 6-5: The bi-linear traction separation curves for open, shear and mixed mode behaviours [Adapted from [121]***].***

Mixed-mode damage initiation and the on-set of softening is defined in terms of a multi-axial stress state and follows the condition

$$\sqrt{\left(\frac{\max(\sigma_I,0)}{{\sigma_I}^Y}\right)^2 + \left(\frac{\sigma_{II}}{{\sigma_{II}}^Y}\right)} = 1. \tag{6-3}$$

Note that the mode I component of the damage initiation criteria assumes that compressive stress in the normal (z) direction does not affect the onset of softening. ${\sigma_I}^Y$ and ${\sigma_{II}}^Y$ are the interlaminar tensile and shear strength respectively. The corresponding mixed-mode relative displacement at damage initiation, δ_m^e, is determined by the tensile and shear stiffnesses of the interface, E_I and E_{II} respectively.

$$\delta_m^e = \frac{1}{\sqrt{(E_I \cos I/\sigma_I^{max})^2} + \sqrt{(E_{II} \cos II/\sigma_{II}^{max})^2}} \tag{6-4}$$

Where the directional cosines, cos I and cos II, are

$$\cos I = \frac{\delta_I}{\delta_m} \tag{6-5}$$

and

$$\cos II = \frac{\delta_{II}}{\delta_m}. \tag{6-6}$$

The critical energy release rates for pure mode I and mode II loading are G_{IC} and G_{IIC} respectively and are determined experimentally. For mixed-mode conditions, the failure criterion for full debonding of the interface follows a power-law defined by

$$\left(\frac{G_I}{G_{IC}}\right)^{\alpha} + \left(\frac{G_{II}}{G_{IIC}}\right)^{\alpha} = 1. \tag{6-7}$$

where is a characteristic constant. Finally, a mixed-mode damage parameter, D_s, is introduced and defined as

$$D_s = \frac{\delta_m - \delta_m^e}{\delta_m^f - \delta_m^e}. \tag{6-8}$$

where δ_m^f is the displacement at full cohesive failure. From this, a history variable, d_t, is introduced defined as

$$d_t = \max(d_{1-\delta t}, D_t) \tag{6-9}$$

In which the subscript t refers to the value of that parameter at a given time-step and 1-δt refers to the prior time step. In this manner, damage is accumulated in the cohesive element. This increases from 0 to 1, with 0 indicating purely elastic behaviour, 0-1 indicating degradation and a jump to 3 indicating cohesive element failure. A failure flag can be set to delete cohesive elements that reach a fully de-bonded state, i.e. $d_t \geq 1$.

This damage parameter,d_t, is used to calculate the normal and shear interface stresses using a loading level factor

$$\delta_{ratio} = \frac{\delta_m}{\delta_m^e + d(\delta_m^f - \delta_m^e)}. \tag{6-10}$$

The normal tensile interface stress is then calculated as

$$\sigma_I = \ (1 - d_t)\delta_{ratio}\sigma_I^Y \ \text{ for } \ \delta_I \geq 0 \tag{6-11}$$

and the resultant shear stress as

$$\sigma_{II} = \ (1 - d_t)\delta_{ratio}\sigma_{II}^Y \tag{6-12}$$

where σ_I^Y and σ_{II}^Y are the experimentally determined yield stresses in mode I and mode II respectively, note that these stresses both have minimum values of 0. The cohesive layer is modelled as zero (or near-zero) thickness and so only the traction-separation behaviour is considered in this material model; behaviour such as stress-wave response or reflection are not

modelled. The material properties used are those of the standard epoxy resin given in the original paper describing this cohesive material model (Table 6-1) [121]. This was chosen as the material properties are well validated against experiments. Adhesion between ceramics and epoxy resins is usually poorer than between laminates and epoxy but recent research into improving the surface preparation of the ceramic have shown that the adhesion can be sufficiently improved such that the mode of failure in the ceramic-epoxy interface is cohesive, rather than adhesive [93]. As such, it is a reasonable if optimistic assumption to use this material model as described in which cohesive failure is the only available failure mode.

Table 6-1: Material properties for a typical epoxy resin [121]**.**

Parameter	Notation	Epoxy resin
Density	ρ	1250 kg / m^3
Mode I Fracture Toughness	G_{IC}	0.21N /mm
Mode II Fracture Toughness	G_{IIC}	1.0 N / mm
Mode I Strength	σ_I^Y	60 MPa
Mode II Strength	σ_{II}^Y	90 MPa
Mode I Stiffness	E_I	1 x 10^5 MPa
Mode II Stiffness	E_{II}	1 x 10^5 MPa
Power law exponent	α	1.7

A necessary condition to allow for stable crack growth is that the mesh is sufficiently fine such that, in the cohesive zone ahead of the crack tip there are a minimum of three elements. A preliminary test model was run to determine if this criterion was met with the existing mesh density, i.e. in-plane mesh density matching that of the pre-existing ceramic tiled mesh of ~0.5 mm element length. A preliminary model was run of a ceramic tile set consisting of three stacked 250 x 250 mm tiles, each of 2.5 mm thickness, with 0.001 mm thick cohesive elements between each layer. The results (Figure 6-6) show that this mesh density is sufficient to meet the necessary conditions.

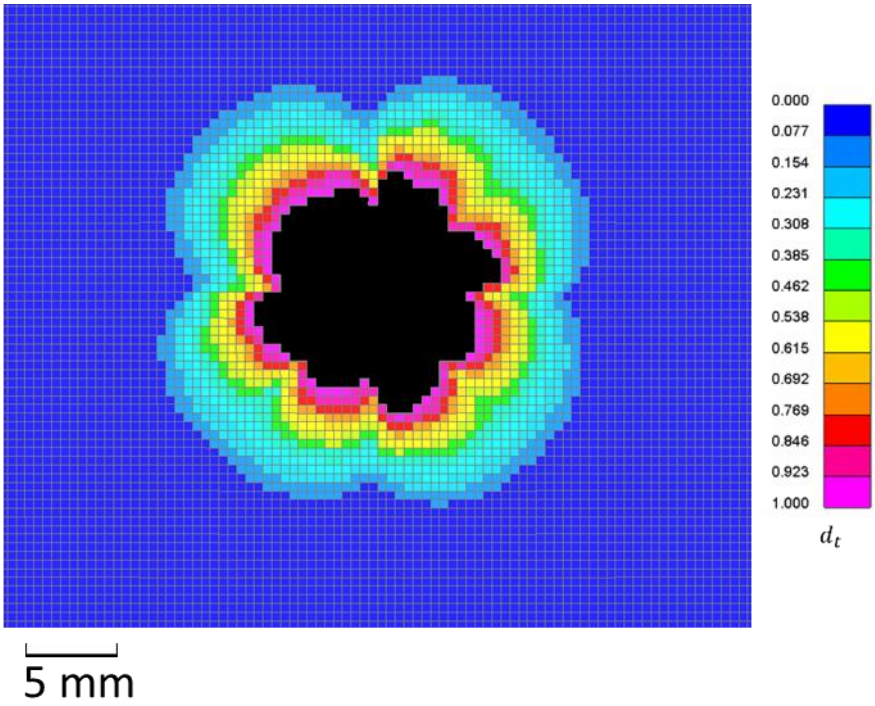

Figure 6-6: A close-up of the hole in the upper cohesive layer beneath the PoI at 3 µs after impact. This was part of a preliminary test model to determine if the cohesive elements were function and that the mesh density was sufficient that there were at least three elements with the fracture process zone.

In the original formulation of the cohesive material model, the true material density is not used [121]. In order to maintain reasonable limits on computation time, the material density was scaled up by a factor of 10^5 to reduce the model time step that is significantly increased due to the thin through-thickness of the cohesive and consequently small element edge length. For quasi-static simulations of tensile strength tests this is an appropriate compromise, however for impact testing in which mass and kinetic energy are more significant concerns this is not acceptable. A further preliminary study was performed using the true material density (Table 6-1) and a series of models with increasing cohesive density. The density was increased until the time-step was being predominantly controlled by the ceramic element size in order to find a value for the density closest to the true value while still maintaining acceptable computation times. The lowest cohesive density for which the ceramic element length was the dominant factor in determining the simulation time-step was a factor of 4 greater than the true value, i.e. 5000 kg/m^3. As the cohesive accounts for less than 0.02% of the total mass of the model (not included backing) this has been considered an acceptable compromise between accuracy of simulation conditions and the limitations of available computational resources.

6.3 RESULTS

Figure 6-7 shows the ballistic results for the chosen array of tile-sets both with and without a cohesive interlayer. A monolithic 250 mm square tile is included for comparison, as is a three-layered 250 mm square tiled system. The inclusion of cohesive layers into the 250 mm three-layered system shows a considerable improvement in performance, reducing the performance gap between the layered system and the monolithic equivalent, mitigating the performance reducing effect of the introduction of through-thickness interlayers.

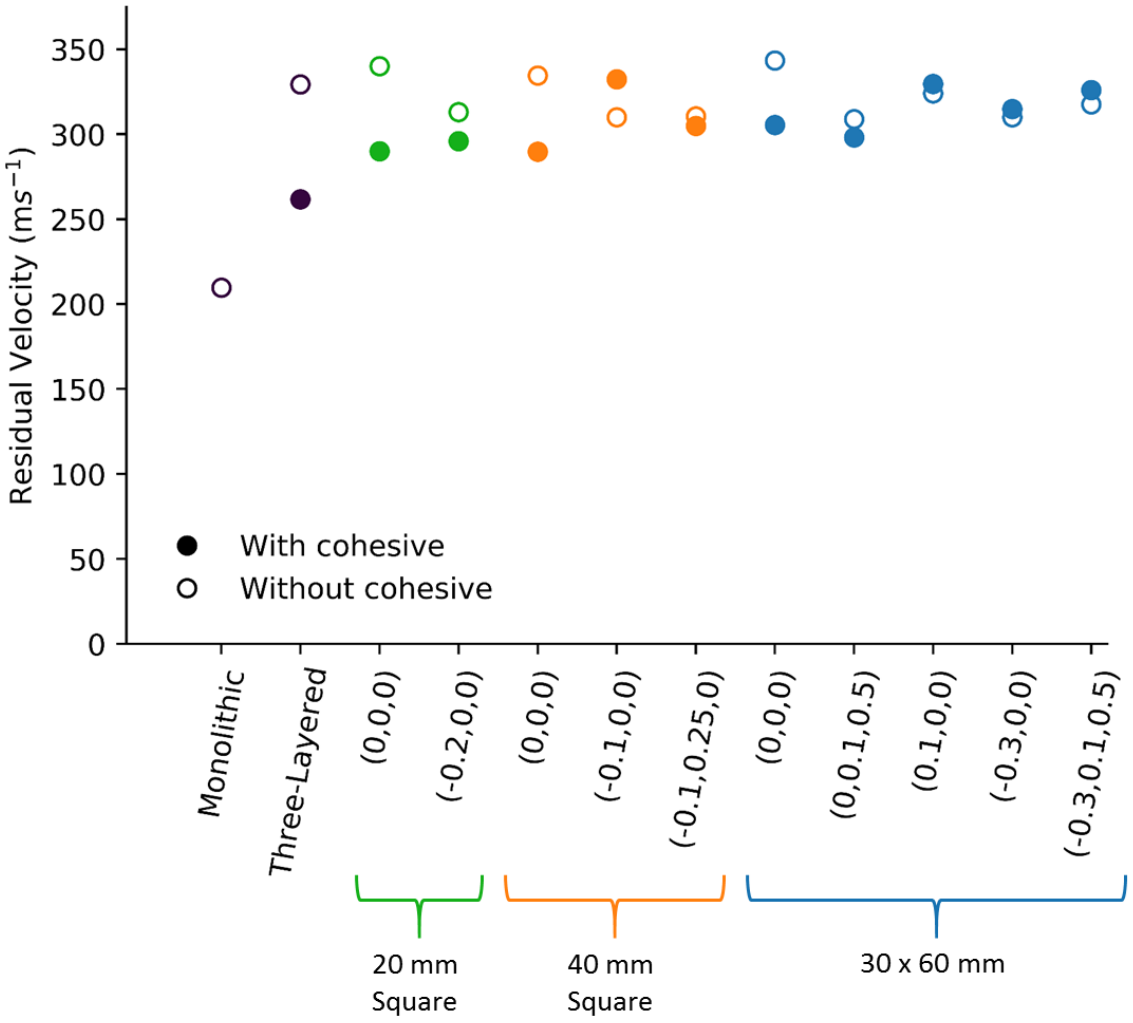

Figure 6-7: The residual velocity for tile-sets with and without a cohesive inter-layer in comparison to a monolithic and a 250 mm square three-layered tile baseline. The notation for the tile-set geometric amplitudes is of the form "(A1,A2,A3)" in mm.

The 7.5 mm thick monolithic tile reduces the projectile velocity, initially impacting at 875 m s^{-1}, down to 209.6 m s^{-1}. As explored in Chapter 4, dividing the monolithic ceramic into layers significantly reduces performance; for the case of the three-layered system the residual velocity increases to 329.2 m s^{-1}. Inserting a cohesive layer into the gaps between layers lowers the residual

velocity down to 261.6 m s^{-1}, significantly reducing the gap between a three-layered and a monolithic ceramic target. The extra kinetic energy absorbed by the three-layered ceramic with cohesive compared to the non-cohesive system is a result of the increased load transfer between tiles which consequently incur greater accumulation of plastic strain, and therefore damage (Figure 6-8b and Figure 6-8c). Full damage (D=1) is defined as a plastic strain of 0.01, these elements then exist in a damaged state until deleted at a strain of 1.5.

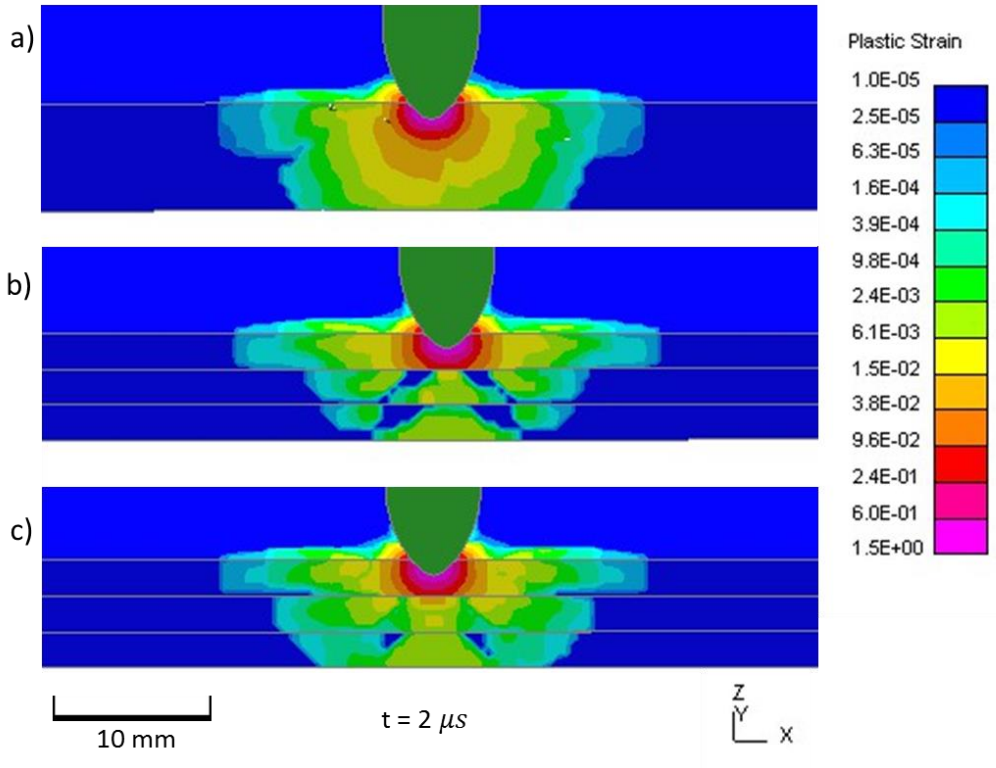

Figure 6-8: Cross-sections of contour plots (logarithmic scale) showing the difference in plastic strain at 2 μs after impact for a) a monolithic 250 mm tile, b) a three-layered 250 mm square tiled system and c) a three-layered 250 mm tiled system with cohesive interlayers.

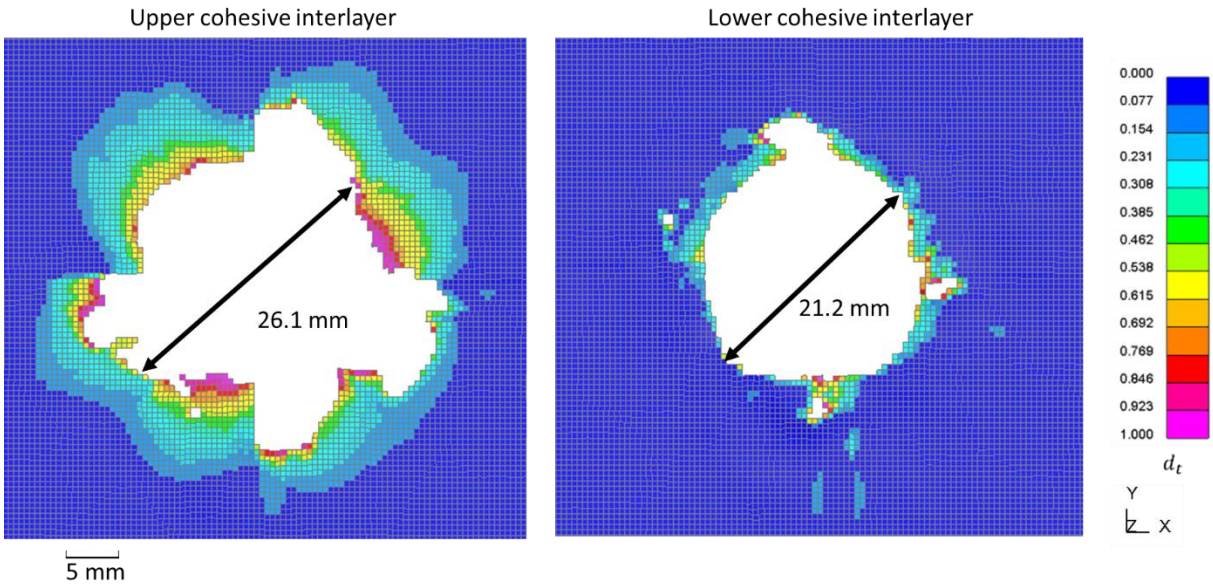

Figure 6-9: The upper and lower cohesive layers in a three-layered 250 mm square tile model after impact (t = 70 μs).

It may be expected from the 250 mm tiled cohesive model that the inclusion of cohesive interlayers would improve ballistic performance for all of the tiled sets made up of arrays of smaller tiles, yet this is not the case (Figure 6-7). The only type of geometry for which performance is consistently improved across all three tile sizes are the flat tiles, i.e. with A1=A2=A3=0, for which residual velocity was reduced by 50 m s^{-1}, 45 m s^{-1} and 38 m s^{-1} for the 20 mm Square, 40 mm Square and 30 x 60 mm tiles respectively. As in the larger tiles, the cohesive interlayer serves to increase the load transfer between layers, particularly in the initial 1 to 5 μs after impact (Figure 6-10). This leads to a greater spread of the compressive shockwave from the PoI through the layers, reducing the interlayer disruption and producing a wave pattern comparatively similar to that of a monolithic ceramic (Figure 6-8c). In Figure 6-10, both 20 mm square tile sets and the (0,0,0) 30 x 60 mm tile set show increased performance with the inclusion of a cohesive interlayer, while the (-0.3,0.1,0.5) 30 x 60 mm tile set has impaired performance when a cohesive interlayer is added. All tile-sets show no change in the shockwave propagation on the upper tile between the baseline (no cohesive) and cohesive variants, in these instances the extent of the shockwave is bounded by the tile edges which slow down the lateral progression.

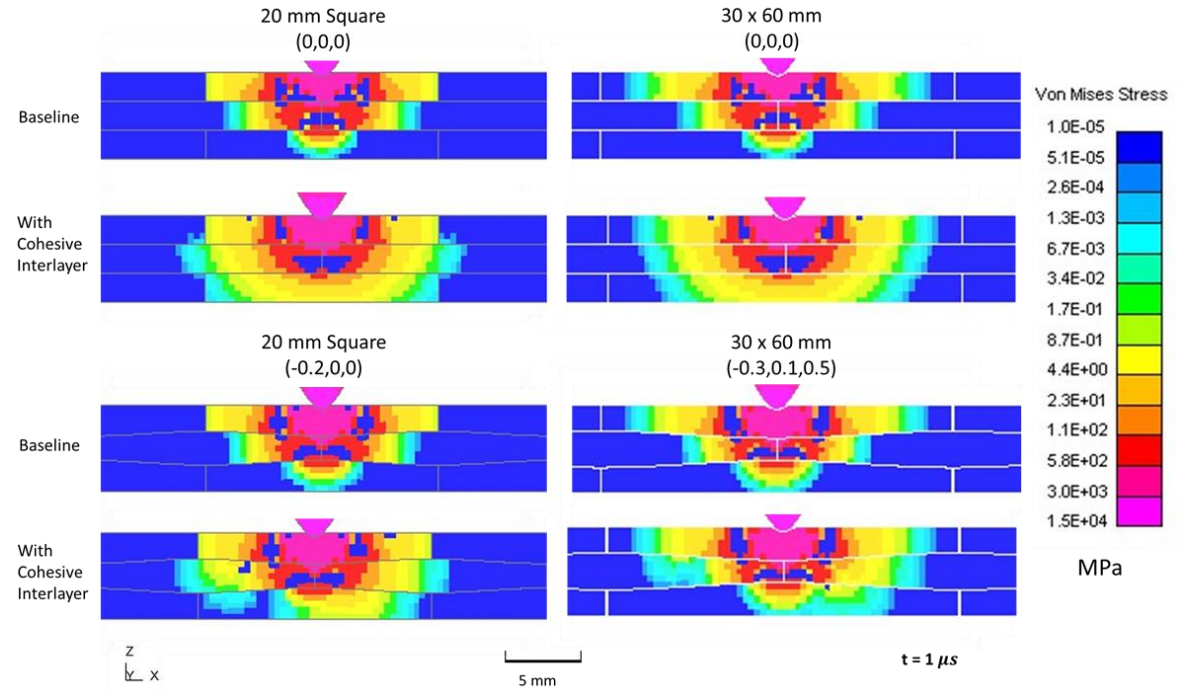

Figure 6-10: A cross-section of ceramic tiles 1 μs after impact showing the spread of the impact shockwave with and without cohesive interlayers (log scale contour levels). Of the four sets, all show improvement in ballistic performance with the addition of a cohesive layer except for the (-0.3,0.1,0.5) 30 x 60 mm tile set.

The addition of A1 surface features to otherwise similar tile geometries with A1 = 0 serves to reduce performance in all studied tile-systems with cohesive interlayers. This is in contrast to earlier simulations, without cohesive elements, in which negative values of A1 showed considerable improvements in ballistic performance for centred impacts, noting that all impacts in this chapter are also centred impacts. For example, comparing two 20 mm square tile sets with cohesive interlayers, (0,0,0) and (-0.2,0,0), the only difference is the inclusion of a non-zero A1 amplitude. Without cohesive, this change in geometry from flat to curved interlayer surfaces improves ballistic performance by 27 m s^{-1}. However, while both are improved by the inclusion of a cohesive, the non-zero A1 tile geometry shows much less improvement in performance to the point that the flat tile-set now outperforms it (290.0 m s^{-1} vs 295.9 m s^{-1}).

The presence of a cohesive layer hinders the lateral spread of the impact pressure wave for flat interlayer surfaces but this effect is much smaller for simulations on tile sets with non-flat interlayer surfaces (Figure 6-11). This appears to be a result of greater confinement of the pressure wave in the through-thickness direction, this is evidenced by the greater volume of comminuted material in the lower layers of the ceramic in comparison to models without cohesive interlayers. The consequence of which is greater energy absorption through fracture of the ceramic, further reducing the velocity of the projectile at the expense of a larger damage zone.

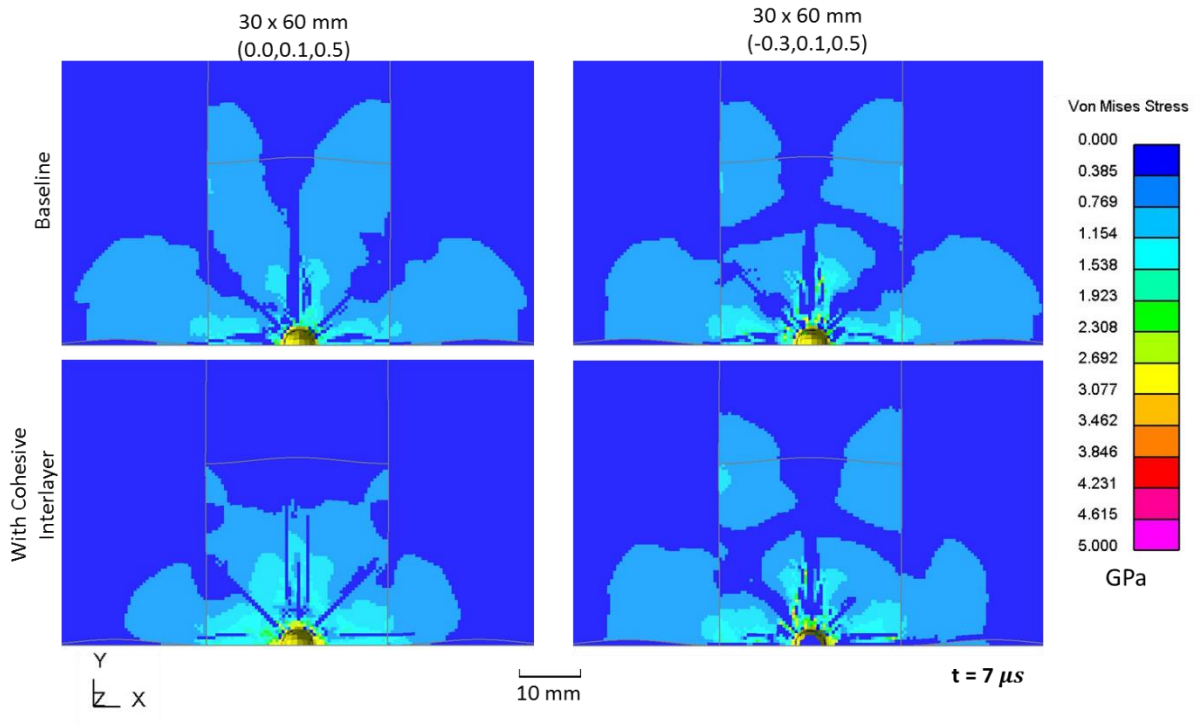

Figure 6-11: Contour plots bisected at the point of impact showing the effect of a cohesive interlayer on the propagation of stress waves within the tile set. The through-thickness profiles of these tile sets can be seen in Figure 6-10.

6.4 VARYING COHESIVE MATERIAL PROPERTIES

In order to explore the mechanisms at work that change the performance of the tiled armour when a cohesive interlayer is added, the effect of independently varying both the fracture toughness and the yield strength of the cohesive was investigated. It is often the case in real materials that fracture toughness and yield strength are negatively correlated, simulation provides an opportunity to explore optimal material properties without this practical limitation [123]. The cohesive material properties used and scaled in these parametric studies are based on experiments conducted on an epoxy used in the production of composite laminates. Experiments by Harris et al [93] have shown that the adhesive bond strength of a standard epoxy adhesive to alumina is weaker than those found when binding with composites. It was also found that the adhesive properties could be improved by up to 16% by increasing the surface roughness of the ceramic via laser ablation prior to application of the epoxy. This was shown to improve adhesion sufficiently to change the locus of failure from interfacial to cohesive failure. In the simulations described in this chapter the interfacial adhesion is modelled as perfect (i.e. using tied contact) and so failure is limited to a cohesive failure mode only. An additional data set is added to the parametric studies using the yield

strengths obtained from experimental alumina-epoxy joint tensile and shear tests: σ_I^Y = 36 MPa and σ_{II}^Y = 32 MPa.

6.4.1 Effect of Changing Fracture Toughness

Fracture toughness is a measure of a materials resistance to crack growth and determines the amount of energy the cohesive layer itself will absorb during failure. The material model for the cohesive, Bristol's Cohesive Zone Model, characterises the critical energy release rate into two parameters for both mode I, G_{IC}, and mode II, G_{IIC}, fracture toughness. The baseline parameters taken from Jiang [121] are G_{IC} = 0.21 N/mm and G_{IIC} = 1.0 N/mm. In this parametric study these are scaled in unison and the ratio between them kept constant; the results are presented in terms of a normalised value relative to the initial values, G_c^*. G_C^* is varied from 0.25 up to 5.

Three tile sets were chosen for this parametric study: the 250 mm square three-layered tile set, the (-0.2,0,0) 20 mm square tile set and the (-0.3,0.1,0.5) 30 x 60 mm tile set. The latter two geometries are chosen to represent tile sets for which the addition of cohesive interlayers, with material properties from literature, improves ballistic performance and for which performance is degraded respectively.

As greater fracture toughness leads to greater energy absorption during crack growth in the cohesive interlayer, it is expected that this would also increase ballistic performance. However, there is no clear trend when varying normalised fracture toughness across the three tile systems studied (Figure 6-12). While there is negligible effect on residual velocity, there is a significant decrease in the area of failed cohesive elements around the PoI after impact for higher fracture toughness values (Figure 6-13). This trend is consistent across all values of G_C^*. However, multiplying the failure area by the normalised fracture toughness to give a comparative correlation for energy absorbed gives numbers of the same order of magnitude but with a 50% variance suggesting that the interaction with the surrounding ceramic is not simply linear with fracture toughness but has many confounding factors. The limitation of the growth of the cohesive failure area may lead to greater performance over multiple shots but does not appear to improve single shot ballistic performance.

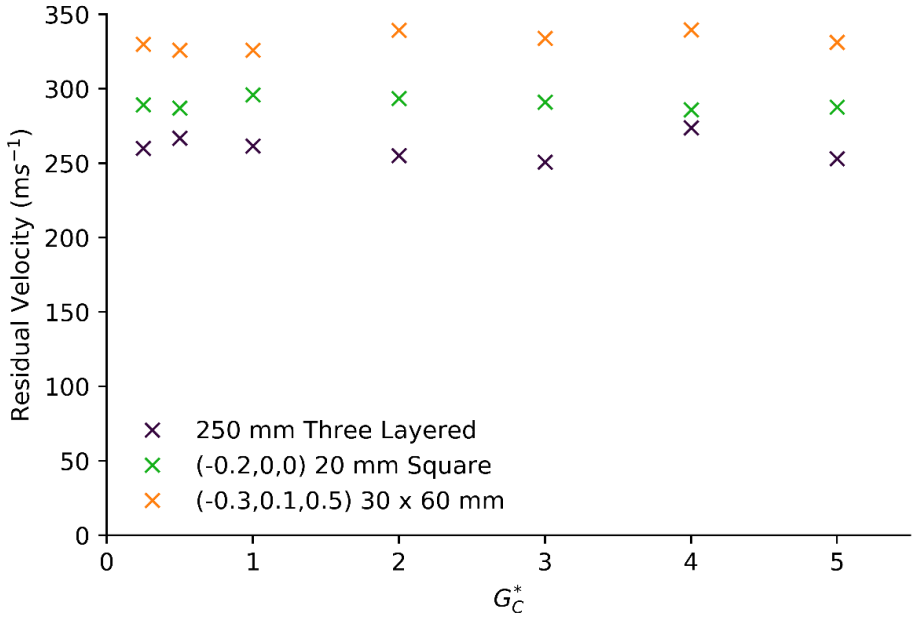

Figure 6-12: The effect of varying normalised fracture toughness, G_C^*, on residual velocity.

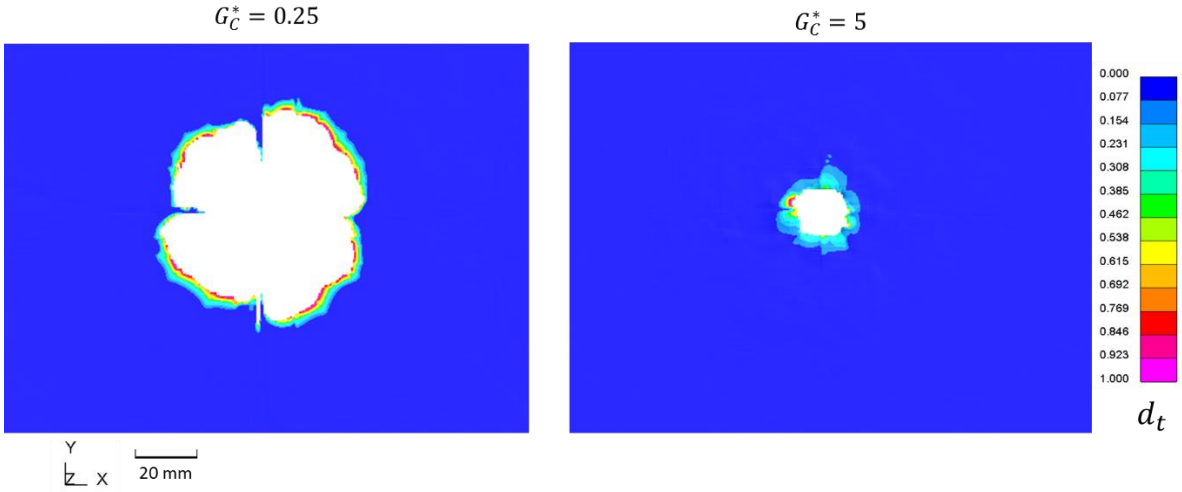

Figure 6-13: A comparison of the after-impact cohesive layers for two different normalised fracture toughness values showing the difference in the total area of failed cohesive elements.

6.4.2 Effect of Changing Yield Strength

The tensile and shear yield strengths of the cohesive interlayer are taken from Jiang [121] and initially set to 60 MPa and 90 MPa respectively. The ratio between these yield stresses is maintained and the yield stress is varied according to a new parameter, σ^{Y*}, the normalised yield stress. The exception to this maintenance of the σ_I and σ_{II} ratio is the use of yield stress parameters taken from Harris [124] in which σ_I^Y = 36 MPa and σ_{II}^Y = 32 MPa; this data point is plotted at σ^{Y*} = 0.55 on Figure 6-14. All other material properties for the cohesive elements are as shown in Table 6-1.

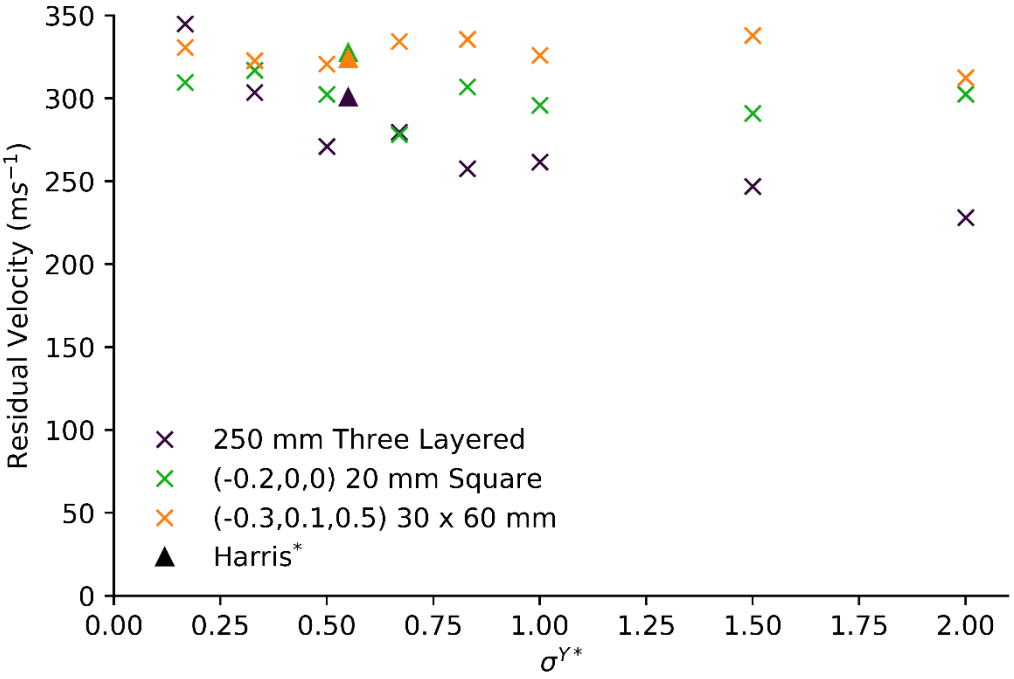

Figure 6-14: The effect of varying normalised yield strength, σ^{Y*}, on residual velocity. "Harris*" refers to material properties taken from Harris [124]***.***

For the 250 mm three-layered, the trend of residual velocity with respect to normalised yield strength is negative with a linear line-of-best-fit gradient of -50.1 m s^{-1}. Reducing the yield strength to σ^{Y*}= 0.25 increases residual velocity to above that of the same system without a cohesive interlayer. This shows that the effects described earlier in tile systems for which the baseline cohesive material parameters reduce performance compared to non-cohesive systems are occurring for those that improve in similar conditions but are compensated by some other mechanism mediated by the yield strength of the cohesive elements. This may be due to the interlayer increasing the spread of the incoming pressure wave across layers causing a greater volume of damaged ceramic but the cohesive interlayer then providing greater lateral confinement of the ceramic to resist the projectile during penetration. The yield stresses of the epoxy are much lower than that of the impact stress wave and so the epoxy would not be expected to significantly absorb those stresses directly even at σ^{Y*} = 2, i.e. the maximum shockwave pressure is 5 GPa, fifty times greater than the yield stresses of the epoxy.

Comparing the post-impact cohesive layers for two (-0.2,0,0) 20 mm square tile sets with σ^{Y*} of 0.33 and 1.5, it can be seen that there is a much greater number of fully failed elements for the cohesive interlayer with a higher yield stress in the in-plane direction for which interlocking does

not occur, i.e. the y-direction (Figure 6-15). The failure pattern is considerably different than to that of the cohesive layers in flat interlayer tile sets, such as that shown in Figure 6-9 for the three-layered 250 x 250 mm tile set. As there is no contact implemented between the projectile and the cohesive elements, cohesive failure only occurs due to relative displacement of the ceramic elements across the interlayer. The "waviness" of the interlayer surface for tiles with non-zero A1, in this figure A1 = -0.2, causes some ceramic tiles to lock together and not experience relative displacement while the impact shockwave causes non-interlocking sections of the tiles to move. Cohesive elements only fail in tension and do not fail in compression.

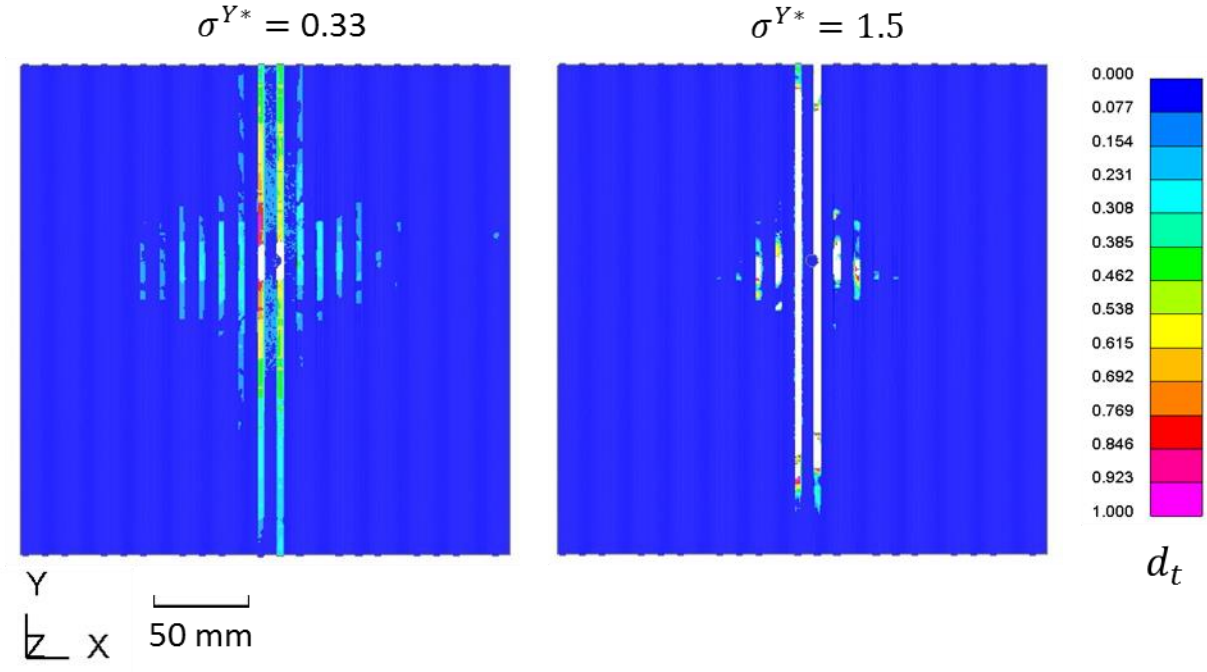

Figure 6-15: The full upper cohesive interlayer for two (-0.2,0,0) 20 mm square tile sets of different yield strengths shown after impact. The white areas indicate elements that have been deleted from the model after reaching a cohesive failure criterion of $d_t = 1$, i.e. peak plastic strain.

When yield stress is increased, the peak displacement must be reduced if fracture toughness is to be kept constant as G_C is proportional to the area under the traction-displacement curve (Figure 6-5). It can be seen in Figure 6-15 that the area that has undergone any plastic-strain at all (i.e. for which dt ≠ 0) is greater for the lower yield stress cohesive interlayer although failure has yet to occur for much of this damaged cohesive and so the higher yield stress comparison has a greater absolute number of failed elements. This could account for the greater ballistic performance as the higher yield stress allows for greater absorption of energy through cohesive failure earlier in the impact event. The cohesive elements appear to "unzip" when channelled in the y-direction by the

shape of the interlayer surface, this may inhibit multi-hit performance for impacts in line with this cohesive failure.

Also visible in these models is evidence of interlocking occurring between the tiles beyond the immediate vicinity of the PoI, shown by the lines of plastic strain repeated regularly over the length scale of the tile width in the x-direction (Figure 6-15). This was not previously able to be visualised without cohesive elements in Chapter 5 due to the intensity of the stresses of the compressive shockwave masking any further contact pressure between tiles due to interlocking as a response to lateral movement. It may be the case that it is only in the presence of a cohesive layer that this interlocking is able to occur at all as without the presence of the cohesive there is nothing acting to confine the tiles from moving out-of-plane, which may alleviate any interlocking that would otherwise occur.

Some form of overwrap applying a confining pressure would therefore be useful in inducing further interlocking now that it has been confirmed that it does occur over the timescale of a ballistic impact. Future work would explore this and also explore the effect of including cohesive elements to bind the tiles in-plane which is likely to improve the performance of interlocking occurring as a result of features A2 and A3.

The macro-scale stress-strain behaviour of nacre has been observed as that of a strain-hardening material (Figure 2-22). This hardening behaviour allows for the more damage-tolerant failure mode of tile pullout, as opposed to brittle tile cracking, to occur preferentially [125]. The strain hardening under tensile loading ensures that neighbouring tiles begin to slide and allows for the functional properties of nacre to delocalise the accumulated damage, leading to increased strain to failure and greater energy absorption [70]. As the cohesive material model used in this section, models the interlayer as an epoxy-like material under a strain softening law, this macro behaviour may be inhibited and instead, once damage begins in one area of the interface, the failure will localise to those cohesive elements that are softening and are thus the "weakest links" in the interlaminar chain [126].The cohesive model used does provide an appropriate model of the expected local energy absorption behaviour for an interlayer and provides additional ductility to the system, however it may fail to provide a good match of the quasi-static response of organic bio-polymers under tension and as such it is of interest to expand the cohesive behaviours explored in future work to include strain hardening. The primary role of the interlayer in high-velocity ballistic events appears to be that of impedance matching to mediate stress wave transmission between ceramic layers and reduce early failure due to reflected waves.

The interlayers within the models in this work are much smaller than work showing the benefits of strain-hardening behaviour in nacre-like glass and carbon fibre systems [125]. In this work, the platelets are modelled as flat and topological locking does not occur, therefore the macro strain-hardening behaviour must be mediated exclusively through an interlayer matrix. When tiles are designed for topological interlocking, neighbouring tiles around the PoI are brought into the macro stress-strain response of the armour via contact friction and compressive locking, as can be seen by the failure of the cohesive interlayers outward from the impact site (Figure 6-15). However, given the spread of the damage zone throughout the ceramics during a ballistic impact is due to stress waves from impact and not through tensile failure due to the flexural response of the armour, it may be the case that the benefits of a strain-hardening interlayer may have minimal effect on ballistic performance. It could, however, benefit the momentum dissipation of a tile armour system which would serve to prevent behind-armour blunt force trauma. Therefore, in future work it would be of interest to investigate the use of a strain-hardening interlayer to maximise delocalisation of the momentum and energy absorption properties of the armour.

6.5 SUMMARY

There is evidence to suggest that the inclusion of a cohesive interlayer aids in the interlocking behaviour of ceramic tiles as well as improving ballistic performance for tile geometries with flat interlayer surfaces. However, for some geometries of the interlayer surfaces the ballistic performance is impeded by the inclusion of a cohesive interlayer due to the change in impedance across the interface affecting stress-wave reflections and transmissions. Over all simulations, the greatest ballistic performance was achieved with the inclusion of cohesive layers as opposed to without. Therefore, careful selection of tile geometry is required in order to optimise performance. The optimal single shot protection is still achieved by a 250 mm monolithic tile. A three-layered 250 mm tile set shows considerable improvement with the inclusion of cohesive interlayers. However, there is little incentive to pursue this design as it has lower ballistic protection against a single impact with minimal potential for improved multi-hit performance (unless the cohesive interlayer acts to confine the fragmented ceramic) compared to the monolithic ceramic.

The tile sets with the greatest performance will now be subjected to multiple impacts to determine multi-hit capability. The tile sets to be taken forward into this study are the (0,0,0) 20 mm square tile set, the (-0.2,0,0) 20 mm square tile set and the (0,0.1,0.5) 30 x 60 mm tile set to represent a range of tile geometries that have shown to reduce the residual velocity of the projectile to below

300 m s^{-1}. In all cases, the models will include cohesive interlayers. In addition, the 250 mm square monolithic and three-layered designs will also be impacted.

CHAPTER 7 – MULTI-HIT CAPABILITY

7.1 INTRODUCTION

The low fracture toughness of ceramics greatly inhibits their capacity for protection against multiple impacts due to the large damage zone created from a single impact [66,111]. For most ceramics, the post-impact dwell period prior to ceramic failure and projectile penetration is a dominant factor in the ballistic performance of the armour. This is especially true for high hardness armour-piercing rounds, which intact ceramic can fracture and further reduce penetrative performance even if the ceramic is overmatched [90]. For fractured ceramic material, this dwell period does not exist, and penetration occurs immediately. Armour designs, such as that described in this work, constructed from tile arrays may inhibit the damage zone from an initial impact and therefore provide greater multi-hit capability. This is eminently desirable for combatants as they are at risk of multiple ballistic strikes due to modern weapon systems with high rates of fire or the limitations during ongoing operations preventing the replacement of personal protection after an isolated single impact.

National Institute of Justice standards suggest a maximum spread of shots for multiple impact testing of 100 mm and a minimum distance between shots of 50 mm [23]. The impact locations for the tiled armour in this section are chosen to fit within this criterion while striking as close to the centre of a surface tile as possible to give results representing the optimal ballistic performance for each armour system. The armour is impacted by three simplified models of the 7.62 mm AP M2 round at 875 m s^{-1}. As in chapters 4, 5 and 6, all armours cover a minimum area of 250 mm x 250 mm and are 7.5 mm in total thickness. They are backed by a 20 mm thick 250 mm x 250 mm polycarbonate backing layer that acts as an inertial mass constraint with a 0.001 mm gap between armour and backing.

There are 9 tile sets taken forward from work in previous chapters for simulation against multiple impacts. There are three baseline tile systems of a 250 mm square monolithic ceramic, a three-layered 250 mm square tile system and that same three-layered system with cohesive elements between layers. Further to this there are three mosaic tile geometries which are tested both with and without cohesive interlayers. These are the (0,0,0) 20 mm square tile set, the (-0.2,0,0) 20 mm square tile set and the (0,0.1,0.5) 30 x 60 mm tile set. These represent the tile geometries that showed optimal ballistic performance in single impact tests and represent different aspects of the nacre-inspired interlocking design.

7.2 MULTI-HIT BASELINE

7.2.1 Monolithic Multi-hit Performance

A baseline for multi-hit performance is first established against a 250 mm square, 7.5 mm thick monolithic ceramic target. The impact locations for this model are equidistant along the circumference of a 100 mm diameter circle (Figure 7-1). All projectiles are given an initial nodal velocity (*INITIAL_VELOCITY) of 875 m s^{-1} and the time interval between impacts is controlled by varying the starting point of the projectile relative to the target surface.

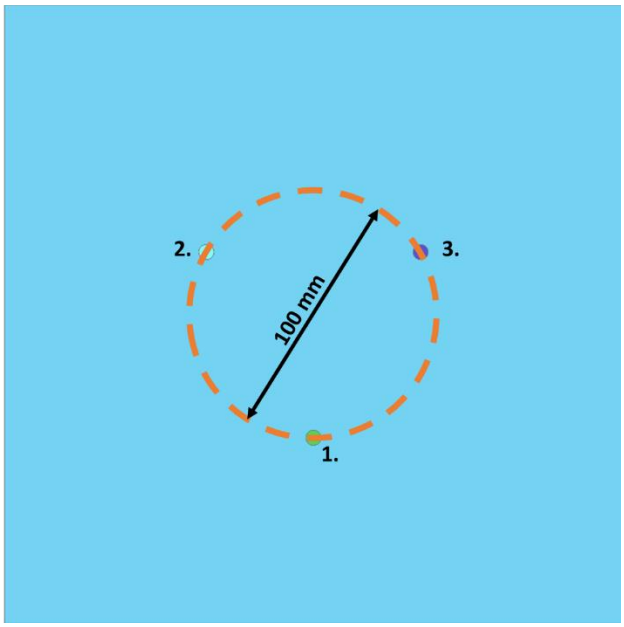

Figure 7-1: The three impact locations with order of impact numbered for a multi-hit test on a monolithic 250 mm ceramic target.

As in previous models, contact is implemented using two contact definitions, both LS-DYNA *AUTOMATIC_SURFACE_TO_SURFACE, between the backing and the ceramic, and between the projectiles and the target. The backing-ceramic contact uses segment-coating on the upper surface of the backing while the ceramic uses a check for the entire part. The three projectiles are placed into a part set that is then flagged in the contact definition for the ceramic-projectile contact.

In experimental multi-hit testing, there may be several seconds or even minutes between shots, this allows for full dissipation of impact stresses between each successive shot. However, in order to model all three impacts within a single analysis and within a reasonable run-time, the time between impacts must be of a micro-second timescale. A test simulation was run that separated each impact by 11 μs. With each impact being separated by a maximum of 86.6 mm (Figure 7-1), this provides sufficient times for interactions travelling at the velocity of the projectile (875 m s^{-1})

to have passed the impact sites of subsequent projectiles at their time of impact but not necessarily to have reach an equilibrium state. Although initial stress waves travelling at a speed matching the projectile would pass secondary impact sites within ~10 μs, this preliminary test allowed for a check of the stress state of the PoI area. The dwell period for an impact on 7.5 mm of alumina is approximately 3 μs, so there is no temporal overlap for dwell between projectile impacts.

Observing the stress waves in this test model, it is apparent that the stress waves from the first impact are propagating through the PoI of the second projectile during the time of impact (Figure 7-2). This stress wave has a peak stress of ~400 MPa. This causes significant disruption to the impact behaviour which is unlikely to be replicated in a practical setting. Although this is an order of magnitude lower than the peak stress ahead of the projectile tip (~3.6 GPa), there will still be significant interaction between the first and second impacts. This does not accurately simulate the impact conditions of experimental multi-hit testing and the time interval between impacts should be increased. The residual velocities of the first, second and third impacts in this analysis are 212, 366.8 and 316 m s^{-1} respectively. The reflection of the shock wave from the nearest edge can also be seen to negatively interfere with the incident shockwave in this figure.

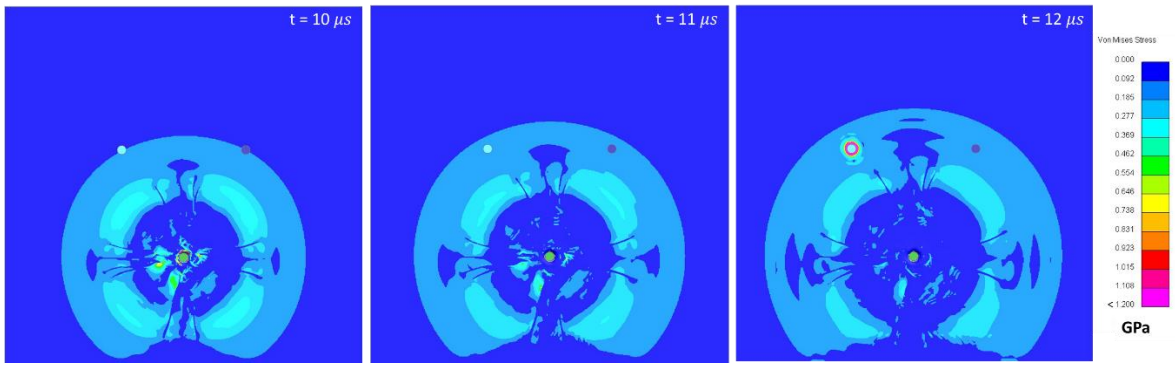

Figure 7-2: A contour plot showing the stress waves propagating from the first impact interfering with the PoI of the second impact in a 250 mm square ceramic target when the time interval between impacts is 11 μs. The peak stresses at the secondary PoI just prior to impact are between 200 and 450 MPa.

The time interval between impacts was then expanded to 20 μs to allow for greater time for the shockwave from the initial impact to dissipate. The increased time allows for both greater radial spread and greater absorption of the kinetic energy from the projectile by the ceramic. In this case, the stress waves from the first impact in the area around the secondary PoI are significantly reduced compared to their peaks after 11 μs, with peaks of around 130 MPa compared to 400 MPa at the earlier impact time (Figure 7-3). Whilst this stress environment is preferable, the results show that the time interval should still be further increased.

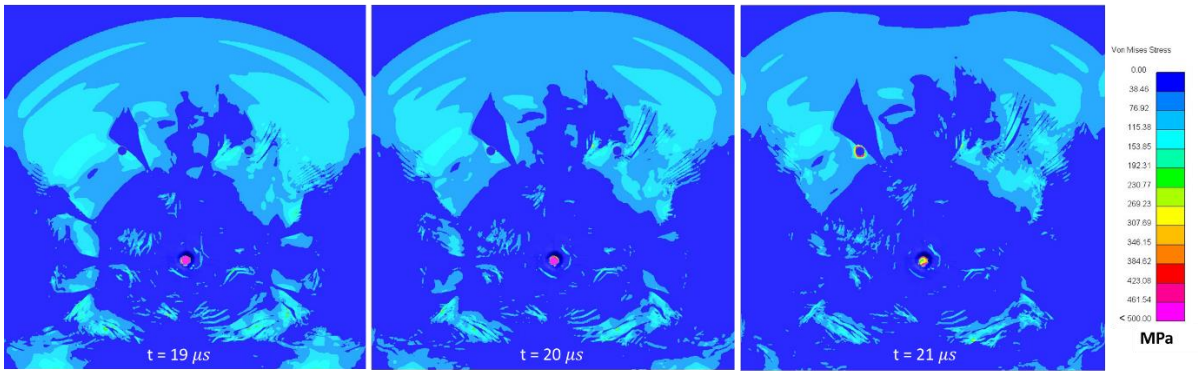

Figure 7-3: A contour plot showing the stress waves propagating from the first impact propagating through the area around the PoI for a secondary impact occurring 20 μs after the first. The peak stresses at the secondary PoI prior to impact are between 30 and 150 MPa.

As there is clear stress wave interference for the simulation with 20 μs intervals between impacts, three further simulations were run with impact time intervals of 30 μs, 50 μs and 70 μs. The time histories of the projectile velocities are shown in Figure 7-4. The time period over which deceleration of the first projectile occurs is ~40 μs. In this context, it is clearly apparent that 20 μs and 30 μs are too short a time interval between impacts as there is overlap between each impact event. In the simulations with impact time intervals of 50 μs and 70 μs, the second projectile is reduced to a lower velocity than that of the first projectile post-impact still occurs. Although this time delay ensures successive impacts are after the deceleration period of the previous impact, damage propagation is still occurring from the initial impact (Figure 7-5). This damage propagation does not reach a stable state until between 75 μs and 200 μs after impact.

A possible explanation for the higher performance of the ceramic against the second impact at 30-75 μs after the initial impact is that the projectile is impacting a ceramic that is not yet damaged but experienced high compressive stress as the impact shockwave passes the secondary PoI. As the shockwave is travelling perpendicular to the direction of impact, the compressive forces from the shockwave may be exerting a counter force resisting the impact due to the Poisson effect [127]. It may also be a result of the compressive force acting as a form of confinement to the ceramic material, which is known to improve ballistic performance [25]. It may also be non-physical anomalous behaviour within the model. No impacts in the literature could be found with a time interval of ≤ 50 μs to determine if this is non-physical behaviour for such rapid impacts or if there is a clear physical explanation. In any case, to characterise the multi-hit performance of these tiles it is necessary to eliminate this effect by increasing the time interval between impacts.

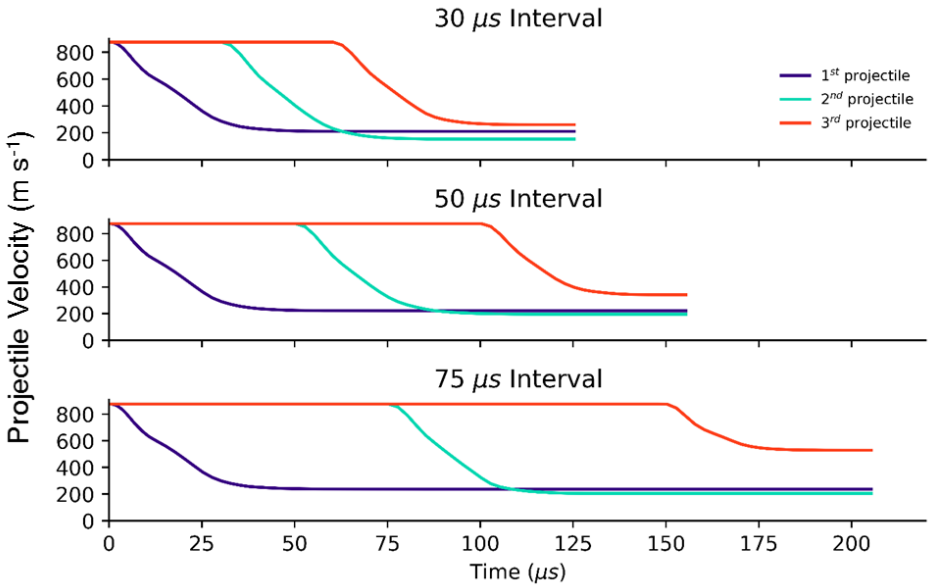

Figure 7-4: The projectile velocity of each projectile during simulations of three impacts with varying inter-impact time intervals.

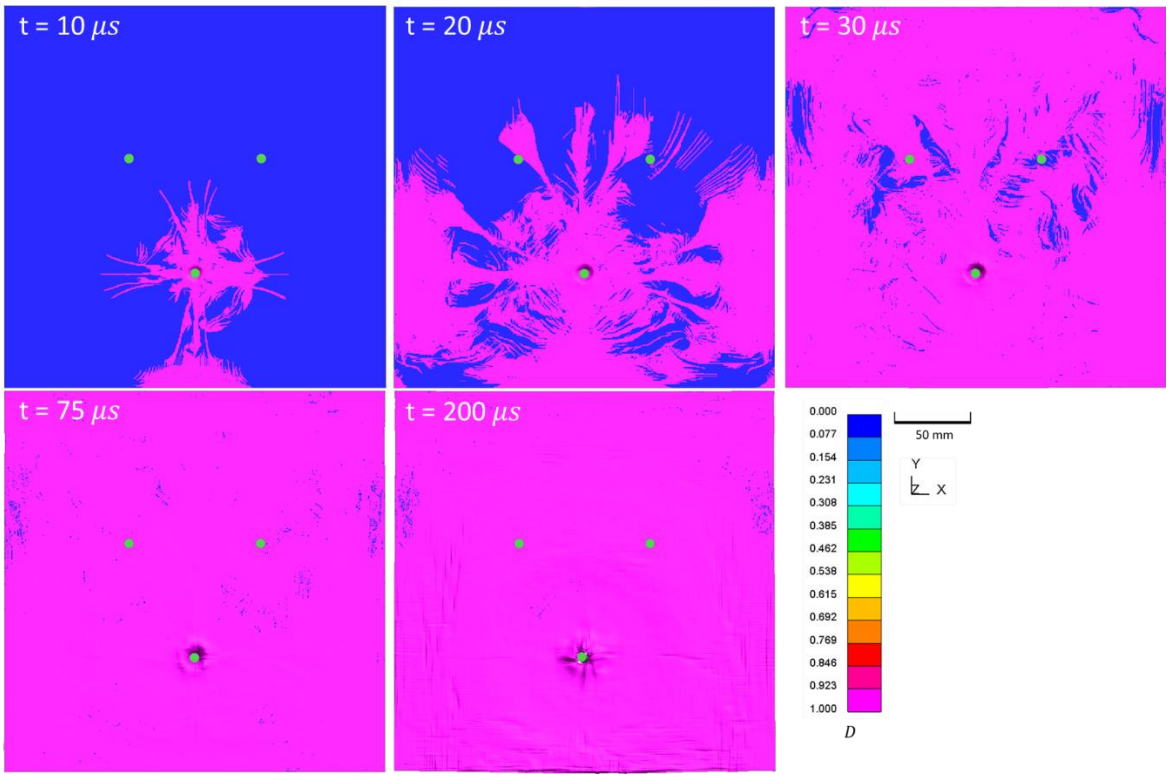

Figure 7-5: The damage state of the 250 mm square monolithic tile prior to the second impact. It can be seen that the development of damage reaches a stable state between 75 μs and 200 μs.

Some multi-hit simulations for vehicle armour used time intervals of up to 200 μs to minimise stress interference between successive impacts [128]. In line with this standard, the time interval was increased to 200 μs and the analyses re-run. This produced results much more in line with

what might be expected of a ceramic armour over multiple impacts, i.e. diminishing performance for successive impacts in close proximity (Figure 7-6) [2,93]. This increased time allows for dissipation of the stress waves induced by previous impacts and for the ceramic element forces to reach a state of approximate equilibrium, allowing for a simulation of multiple impacts that is more representative of "realistic" test conditions (Figure 7-7). There are still some latent stresses in the model that are not dissipated by the time of the next impact. These stresses are much lower than those observed in models of shorter time intervals (20 MPa vs 400 MPa) and are present over a much smaller volume of ceramic further away from the secondary impact zone. These stresses are therefore considered a reasonable compromise between shockwave dissipation and computation time. All multi-hit models within this section are therefore modelled with this time interval between impacts. The residual velocities for each successive projectile are 208.1 ms^{-1}, 654.4 ms^{-1} and 743.3 ms^{-1} in order. In terms of projectile deceleration, the performance of the monolithic armour against a second and third impact represent a 69% and 82% reduction in performance compared to the ballistic protection against the first impact.

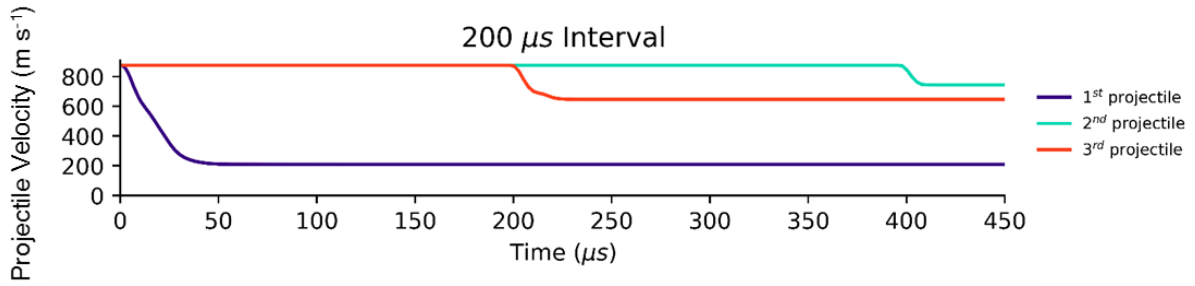

Figure 7-6: Projectile velocity over time for three impacts into a 7.5 mm thick alumina monolithic target separated by a time interval of 200 μs.

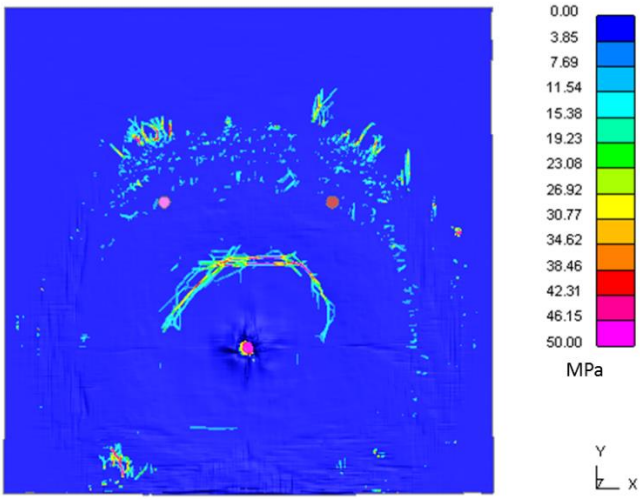

Figure 7-7: A top down view of the full monolithic ceramic target with projectiles indicated in pink. Latent stresses in the monolithic ceramic are still present at t = 190 μs immediately prior to the second impact. These are much lower than at shorter time intervals.

7.2.2 Three-Layered Multi-Hit Performance

A further tile geometry that is relevant before moving to mosaic structures is that of the same 7.5 mm thickness of ceramic as the above monolithic target but divided into 3 layers, with and without cohesive interlayers. This set up can provide information about the confining effect of the cohesive layer on comminuted material and the effect that has on multi-hit performance prior to moving on to nacre-based tiles. In Chapter 6, a three-layered 250 x 250 mm tile system with cohesive interlayers was shown to have higher ballistic performance than any armour made up of smaller tiles. However, the beneficial effects of cohesive elements were insufficient to compensate for the reduction in performance that comes from the introduction of interfaces into the through thickness of the monolithic armour (i.e. by division into layers) (Figure 4-9). For details of the material properties of the epoxy-based cohesive interlayer see Table 6-1. The impact locations of the three 7.62 mm projectiles on to this three-layered system are the same as for the monolithic system (Figure 7-1).

The reduction in performance between the first and second impact is more pronounced for a monolithic target compared to that of a three-layered system (Figure 7-8). Both with and without cohesive interlayers, the three-layered system underperforms the monolithic target against the first impact and outperforms against the second. Residual velocity for the third projectile impact is within 1% for both the monolithic and the three-layered armours. The introduction of layers inhibits damage propagation at the cost of ballistic performance, this leads to the reduced

performance against the first impact but relative improved performance against the second impact compared to a monolithic system. By the third impact, the total damage volume has increased to diminish this improvement and bring the performance of all tile systems in line as all models are in a fully damaged state. It was observed in Chapter 6 that the cohesive layer increases load transfer between layers, facilitating the propagation of the shockwave through the layers and resulting in a greater volume of damaged ceramic in the lower layers of tiled armours (Figure 6-8, Figure 6-10). As a result, the model with cohesive interlayers outperforms against a single shot but, due to the increase in damage sustained, performs worse against a second impact compared to the same three-layered system without cohesive. The cohesive does not act to significantly inhibit the displacement of the alumina tiles in this model, a behaviour which could have induced a form of confinement and therefore improved performance (Figure 7-9). This figure shows the underside of the top ceramic tile for models with and without cohesive interlayers, there is no significant difference between the resultant displacement for either model. This is likely because the impact shockwave travels radially outward uninhibited by lateral interfaces and the forces of the shockwave far exceed the yield stress of the cohesive (~1-4 GPa vs 60-90 MPa). The difference in performance between these two models is therefore due to greater load transfer between layers mediated by the cohesive interface rather than any confinement mechanism.

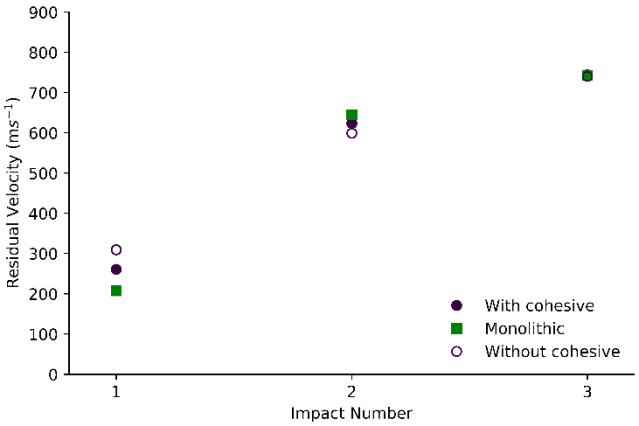

Figure 7-8: The multi-hit performance for three-layered 250 mm square tiles, with and without cohesive interlayers, in comparison to that of a monolithic target. Residual velocities for the third impact are near coincident.

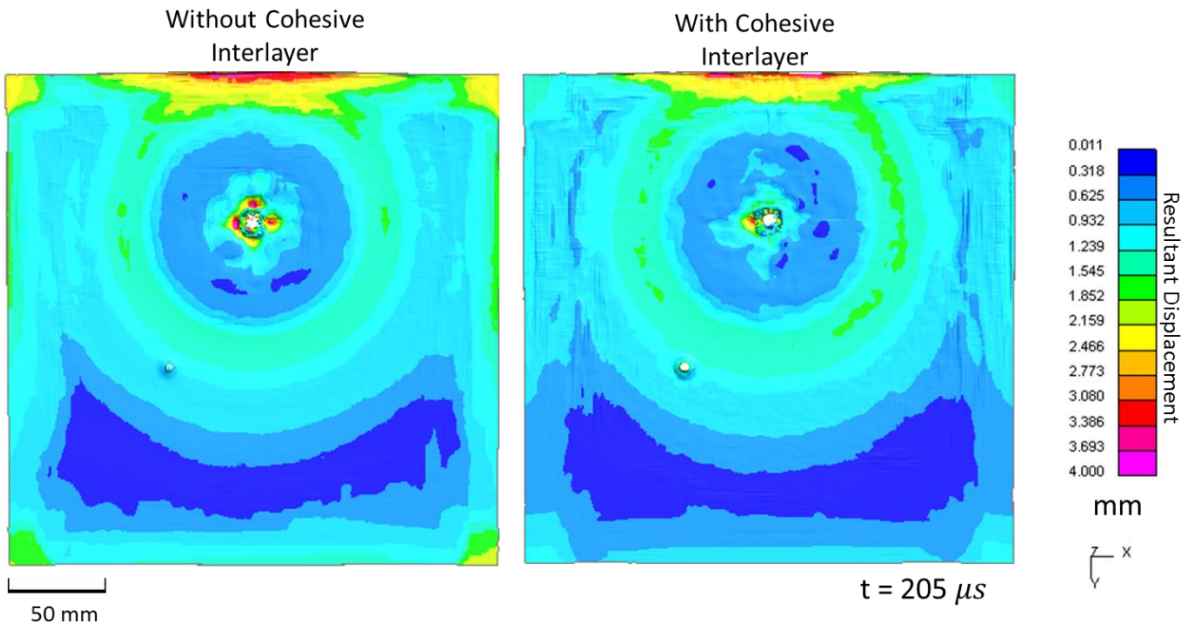

Figure 7-9: The resultant displacement on the underside of the top layer of ceramic for the three-layered 250 mm square tile sets, with and without cohesive interlayers, just after the second impact. The similarity suggests that the cohesive interlayer does not act as a confinement mechanism and that the difference in ballistic performance is therefore a result of the cohesive mediating greater load transfer between layers.

7.3 Multi-Hit Performance for Mosaic Tiles

The three tile sets chosen to represent the optimally performing nacre-inspired geometries are mosaics constructed from (0,0,0) 20 mm square tiles, (-0.2,0,0) 20 mm square tiles and (0,0.1,0.5) 30 x 60 mm square tiles (Figure 7-10). This covers the range of interlocking mechanisms proposed in Chapter 5 that have the potential to enhance the overall ballistic performance of a tiled system against multiple impacts. The amplitudes of A1, A2 and A3 in these models are relatively low compared to their overall size. Larger values of these parameters resulted in poor single shot ballistic performance and improvements were only notable for smaller values, with the exception of A1 for which large negative values showed significant improvements at the cost of impaired tile-edge performance (Chapters 5). These tile sets are impacted both with and without cohesive interlayers making a total of six mosaic tile targets that were measured for multi-hit capability.

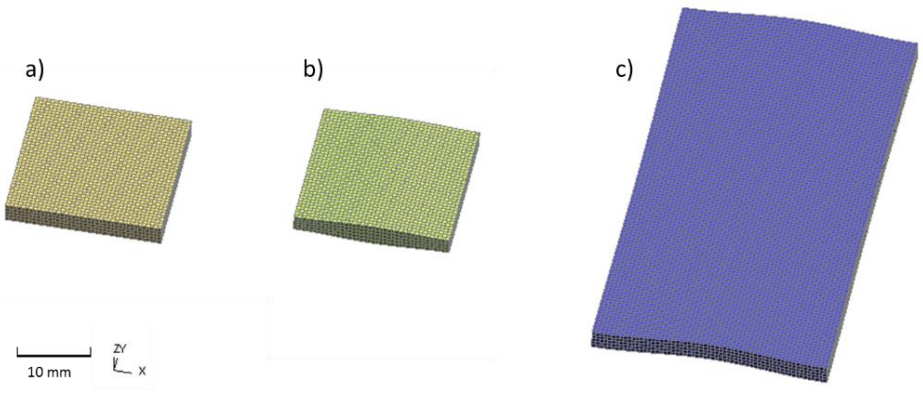

Figure 7-10: The three optimally performing tile geometries chosen for multi-hit testing: a) (0,0,0) 20 mm square tile, b) (-0.2,0,0) 20 mm square tile and c) (0,0.1,0.5) 30 x 60 mm square tile. Note that (b) represents a middle layer tile with A1 variation on the upper and lower surfaces.

The impact locations for these tests were chosen such that each projectile impacts the centre of a tile, all projectiles impact within a 100 mm diameter circle and all projectiles are maximally distant from each other within those limits (Figure 7-11). These criteria reduce the distance between projectiles from the distance between PoIs in the monolithic and three-layered 250 mm targets (86.6 mm). They are chosen to test the optimal performance of the mosaic tile systems as the reduction in performance at tile-edges is assumed to be greater than that for the small increase in proximity of each successive projectile impact (based on the information shown in Figure 5-8). The order of impacts in the 30 x 60 mm tile sets is chosen to avoid successive impacts on immediately adjacent tiles.

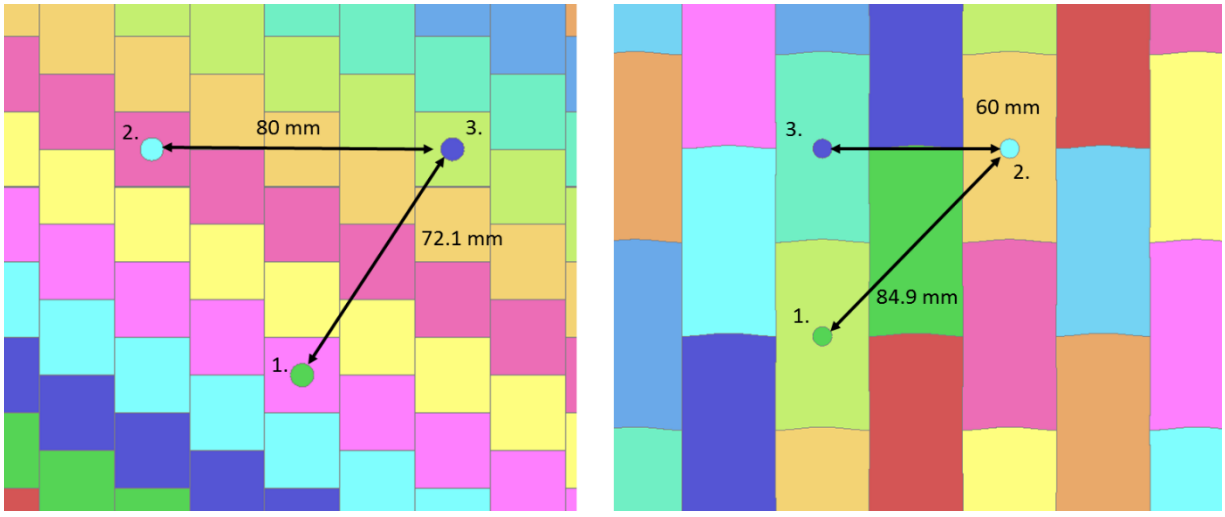

Figure 7-11: The impact locations for the projectiles for multi-hit modelling against (left) 20 mm square tiles and (right) 30 x 60 mm square tiles. The projectiles are numbered in order of impact.

The residual velocities for the multi-hit tests with 200 μs intervals between three successive impacts are shown in Figure 7-12. As shown previously, the ballistic performance of these nacre-inspired tiles is worse than that of the monolithic ceramic equivalent and both of the three-layered 250 mm square tile sets. All tile sets show significantly diminished performance after the first shot with a further drop in performance after a second impact. There are significant variations in single impact performance. The largest difference being between the monolithic ceramic and (0,0,0) 20 mm square tile sets; the monolithic ceramic decelerates the first projectile by a further 146 m s^{-1}. However, by the third impact, ballistic performance is comparable between all tile sets with all residual velocities being within a 35 m s^{-1} interval. This is likely because all elements in the ceramic volume have reached a fully damaged state (D=1) and there is therefore zero or minimal effect of tile interfaces that remain present only due to the mesh-based nature of FE simulation (Figure 7-5).

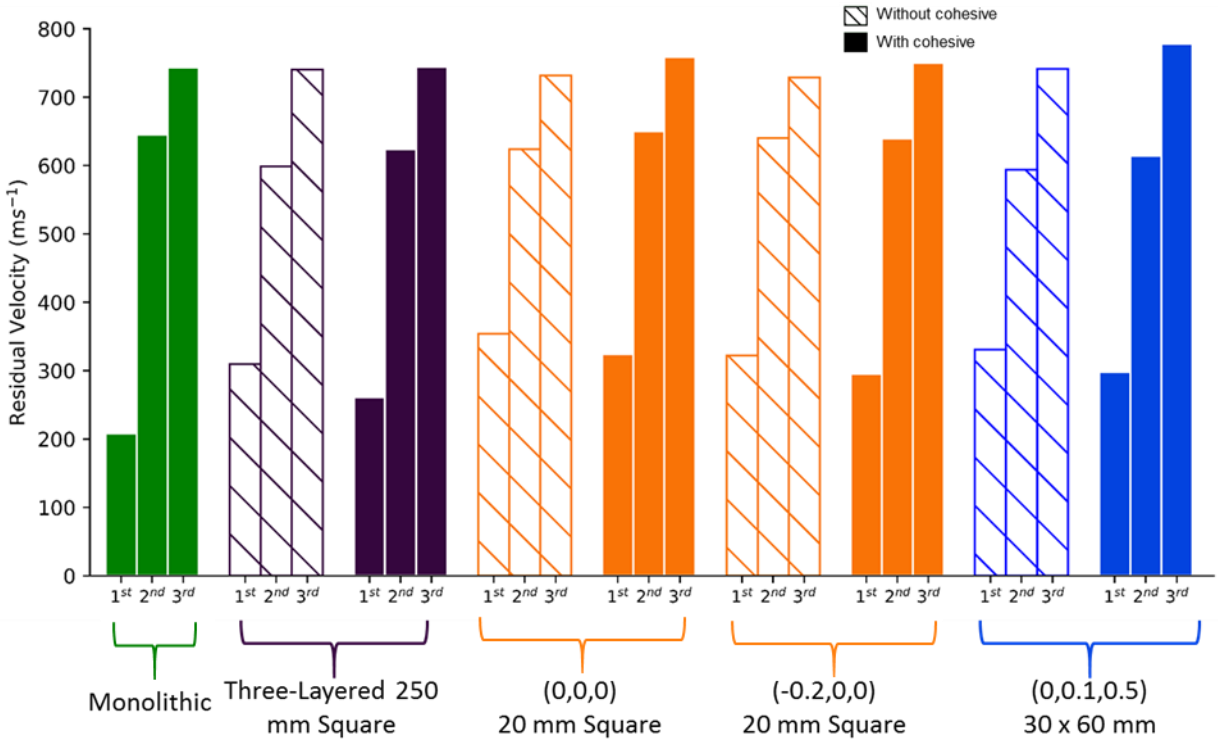

Figure 7-12: Residual velocities for the 1st, 2nd and 3rd projectiles in multi-hit tests of a range of alumina targets.

In terms of multi-hit capability, the optimally performing mosaic tile is the (0,0.1,0.5) 30 x 60 mm tile without cohesive interlayers. This tile set retains 52% and then 24% of its initial ballistic performance, characterised by percentage of deceleration of the first projectile, against a second and third projectile impact. This is greater than the multi-hit capability of the monolithic ceramic (34% and 20%). However, these values are primarily achieved due to a much poorer initial

performance relative to the monolithic ceramic, although with a further 50 m s -1 deceleration compared to the monolithic ceramic for the second projectile and 1.5 m s-1 lower residual velocity against a third impact. Therefore, this armour may be useful against rapid fire small arms but, in its current state and ignoring practical concerns around manufacture, this design would not be recommended for use in the field.

When using the JH-2 material model, once ceramic elements reach a fully damage state (D=1) the tensile strength goes to zero and the yield stress is limited to a maximum of S_{max}^{f}, which in the case of the alumina material properties used is half the intact strength (Table 3-6). These fully damaged elements remain in the model until a strain of 1.5 is reached, set by the parameter FS, at which point they are deleted. Despite significant deformation in the tile set after multi-hit testing, only the elements in the immediate vicinity of the PoIs reach the required element deletion criteria.

Although all tile sets perform very similarly against a third impact, there is a small increase in residual velocity for all of the mosaic tile systems with cohesive interlayers compared to the other systems (Figure 7-12). In the JH-2 model, fracture strength still has a pressure dependence and can be increased, up to the maximum of half of the intact stress, if subject to hydrostatic pressure. The greater load transfer between layers mediated by the cohesive interlayers leads to a marginal increase in the dissipation of the stress-waves over time. Therefore, it may be the case that greater residual stresses have marginally increased the performance of the damaged ceramic in those models without cohesive interlayers.

Impacts against fractured ceramics cause significantly greater deformation around the PoI while those against intact ceramic create considerable smaller holes in the target (Figure 7-13). This shows the more fluid-like behaviour of a comminuted ceramic is captured by the JH-2 model. The conforming of the ceramic around the square polycarbonate backing that is visible in these figures is not representative of physical ceramic behaviour. Experimentally many targets are completely reduced to debris and this may be a limitation of the model approximated this behaviour [129].

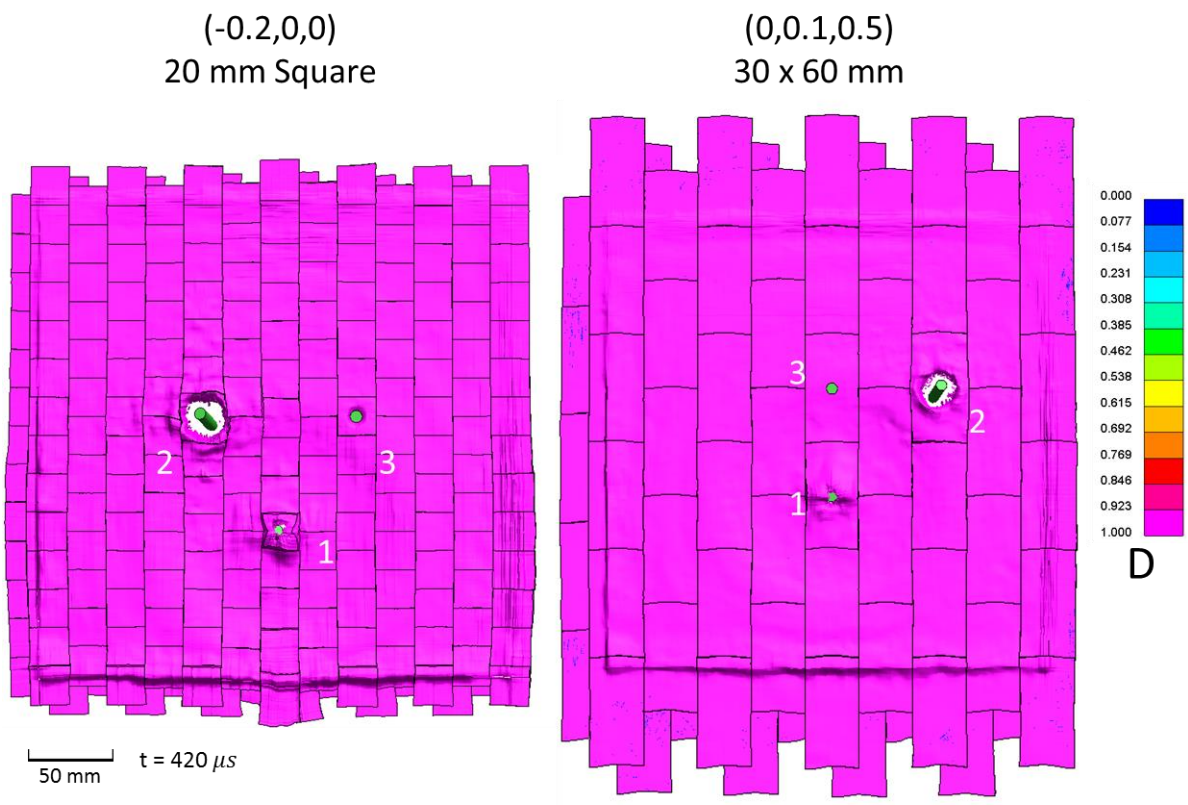

Figure 7-13: The relative sizes of the first and second impact sites show the difference in ballistic response of damaged and undamaged ceramic (the impact hole from the 3rd projectile has not had time to deform at this time-stamp). Damage propagation continues until the volume of ceramic is in a fully damaged state.

Alumina tiles 50 x 50 mm in size and 14 mm thick have been shown to disintegrate completely under ballistic impact, this can be mitigated with appropriate confinement to improve the integrity of the post-impact ceramic comminute [129]. However, larger alumina tiles such as a monolithic ceramic body armour insert do not disintegrate, although cracks may propagate to the tile boundary [66]. The propagation of the damage zone to the full volume of the ceramic from a single impact does not match experimental data, despite good matches with the data in terms of single impact ballistic performance (Figure 7-14) (Chapter 3). Much of this damage propagation occurs post-impact and the damage state observed at $<20\mu s$ post-impact shows crack propagation in line with that which would be expected experimentally for monolithic ceramic armours (Figure 3-15). This implies that the Johnson-Holmquist 2 model performs well against single impacts but tends to over-predict the total damage volume as the simulation continues to run after impact. This is in part due to the low fracture toughness of the ceramic in conjunction with boundary conditions that ensure that shockwaves in the material are reflected and not dissipated to the surrounding environment, other than initial transfer of energy to the backing material. The shockwave energy

will therefore be reflected within the ceramic material and be absorbed via greater accumulation of damage and element deformation. Adding a component to the model to confine the ceramic and act as a "shockwave sink" for the dissipation of this energy may reduce this propensity for damage volume over-prediction. The polycarbonate backing in the model partly fulfils this function but is insufficient without a change in boundary conditions to ensure sustained contact throughout the simulation.

The predictions of this material model closely match experimental data for residual velocity and the immediate post-impact damage state (<20 μs), however residual state prediction is poor when the model is allowed to run. There are therefore limitations to the accuracy of simulations that require accurate residual stress and damage states, such as multi-hit simulations and further validation work or further development of the ceramic material model is required. Given that successful modelling of multiple impacts against other materials using other material models, such as modelling of a glass-polycarbonate laminate using the Johnson-Cook model, has been achieved with good accuracy, accurate multi-hit modelling of alumina is achievable with further work [128].

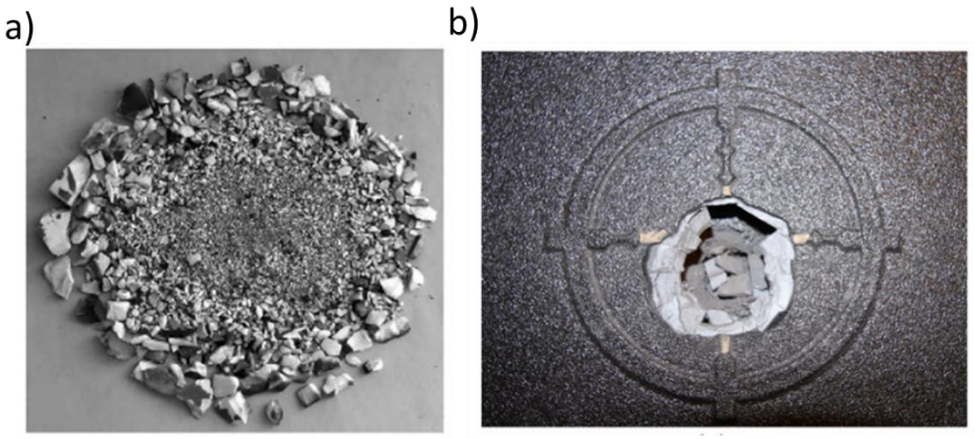

Figure 7-14: A comparison of the post-impact state of a) a 50 x 50 mm alumina tile and b) a full size alumina chest plate (the imprint of the circular target is ~50 mm in diameter).

7.4 SUMMARY

Compared to a monolithic ceramic armour, mosaic tile armours provide marginal multi-hit improvements against a second impactor at the cost of single shot ballistic performance with the (0,0.1,0.5) 30 x 60 mm tile set without cohesive interlayers outperforming the monolithic armour against a second impact by 27%. However, a further third impact results in residual velocities that are independent of initial tile geometry, given a constant areal-density, with the exception of a small increase in residual velocity for tiles with cohesive interlayers.

At this point, it does not appear as if the micro- and nano-scale structures that provide nacre with its improved functional properties translate to the macroscale high-strain environment of ballistic impacts. As noted, there are some benefits to a tiled ceramic design in terms of multi-hit performance and, as interlocking occurs over the timescale of a ballistic event, dissipation of momentum. However, these do not outweigh the significantly compromised single impact performance. Designs predicated on nacre-inspired design principles may be of use in the design of multi-hit capable armours to protect against lower velocity small arms in which the strain-rate and kinetic energies are slightly closer to the environment in which nacre exhibits its enhanced functional properties.

There are limitations to the predictive ability of the Johnson-Holmquist 2 model as a result of a tendency to over-predict damage volume. Several reasons for this over-prediction have been postulated, chiefly among them is the lack of any major mechanism to dissipate the shockwave into the environment over time as would occur in any physical set-up. The development of a model that mitigates this issue, either through changes to the ceramic material model or through changes to the boundary conditions of the ceramic, would allow for more reliable conclusions to be drawn from FE simulations about the multi-hit capability of novel armour designs.

CHAPTER 8 – CONCLUSION

The goal of this thesis was to explore the ballistic potential for a nacre-inspired biomimetic body armour. The characteristics of nacre that were of primary interest in this design are topological interlocking and the inclusion of a ductile cohesive interlayer matrix. These features give nacre remarkable fracture toughness against impacts by sea debris. This thesis explores whether these micro- and nano-scaled features could be scaled up and incorporated into the design of a ballistic armour capable of achieving both good single shot ballistic protection and multi-hit capability.

This question was explored through the use of finite element analysis and the initial stages of this work focussed on creating, verifying and validating a ballistic impact model of an alumina ceramic target, backed by polycarbonate and impacted by a simplified model of a 7.62 mm AP M2 round at 875 m s^{-1}. This model was validated against depth of penetration data provided by DSTL for a range of thicknesses of alumina. A novel nacre-inspired tile geometry was then proposed and developed in stages, starting at tile size, then developing an optimised shape for interlocking and finally including cohesive interlayers.

The specific novel aspects of this work involve numerical analyses of high-velocity impacts on a nacre-inspired armour, where previously the literature has focussed on quasi-static and low-velocity testing [9,75,82,85,125]. This work also features a novel tile geometry based on the functional architecture of nacre. Several aspects of basic tiled armour designs that have been known in industry as heuristics but have not been reported in the literature, namely tile size effects on ballistic performance, have also been explored; the lack of scientific support for these known practical concerns have been discussed by James and Crouch [2,11]. Finally, this work looks into the multi-hit capability of nacre-inspired armour, an understudied aspect of their performance given that this is the most promising aspect of tiled armour design.

8.1 SUMMARY OF KEY FINDINGS

- Topological interlocking does occur over the timescale of a high-velocity ballistic event (~30-60μs). This is made clear in the models including cohesive layers as the failure of those interlayer elements provides a visual reference for this interlocking (Figure 6-15). This shows that a nacre-inspired design may have a place in the design of ballistic armour as suggested by prior low-velocity and quasi-static testing in the literature [9,75,82,85,125]..
- The ballistic performance of a 7.5 mm monolithic ceramic armour far outweighs the performance of that of three 2.5 mm layers against an 875 ms^{-1} 7.62 mm AP M2 round in

terms of residual velocity (209.6 ms^{-1} vs 329.2 ms^{-1}). The large reduction in performance due to the introduction of through thickness interlayers requires significant improvements to be found in other characterisations of performance to justify a change in design, this has been noted in the literature [2,43,75].

- The reduction in performance is attenuated by the introduction of a cohesive layer to allow for greater impedance matching and therefore a reduction of (tensile) stress waves reflections at interlayer boundaries, lowering the residual velocity result for the three-layered system to 261.6 ms^{-1}.
- The optimal performance against a single shot for any nacre-inspired tiled system within the design space outlined in Chapter 4 was for that of a (-0.2,0,0) 20 mm square tile (see Chapter 4 for naming conventions) exhibiting a residual velocity of 295.9 ms^{-1}. This suggests that the benefits of a tiled system are only likely to be found in specific multi-hit scenarios.
- Characterisation of multi-hit capability shows that tiled armours can achieve greater performance against a second impactor compared to a monolithic armour. The (-0.2,0,0) 20 mm square tile offered the best second shot performance, achieving a residual velocity 27% higher than that of the monolithic ceramic. However, all tested armour systems, including a monolithic ceramic, performed similarly poorly against a third impactor, exhibiting ~20% of the reduction in velocity of the intact monolithic ceramic against a single impact.
- There are significant limitations in the Johnson-Holmquist 2 model [67,130]. Most significantly is the over-prediction of damage volume due to an insufficient built in mechanism for energy dissipation. This severely limits the reliability of the multi-hit performance study as the second and third impactors strike a ceramic that is likely over-damaged relative to a physical experiment. The model is still useful for single shot characterisation as this over-damaging behaviour occurs after an initial penetration event..
- These results strongly suggest that it is not an applicable design philosophy for protection against an armour piercing, high velocity projectile due to the reduction in performance against a single shot due to the inclusion of through-thickness interfaces and the subsequent shortening of the initial dwell period.

8.2 FUTURE WORK

Further work is required to overcome the limitations of the Johnson Holmquist 2 model discussed at the end of Chapter 7. This would involve a focus on developing appropriate boundary conditions to mitigate the over-prediction of damage accumulation through the ceramic volume of the armour designs. It may also be of interest to perform lower velocity impact testing or drop-tower simulations to observe the in-situ interlocking. Further development of the cohesive interlayers would include cohesive elements between the lateral surfaces of the tiles. This may act to increase the confinement of the tiles (and therefore ceramic yield stress) as well as increase the interlocking between tiles with curved lateral surfaces.

In this work, all layers of tiles were of the same thickness. There is some evidence in the literature to suggest that thicker surface layers may optimise ballistic performance. Having shown the key features of a nacre-inspired design are functional in an armour, changes in the layer thickness could be used to enhance ballistic performance for a fixed areal-density.

There are several further topologically interlocking tile geometries that were not studied in this work (Figure 8-1). A "shuriken" based tile and a hexagonal "wavy" tile based on work by Knipprath [75] were both prototyped and 3D printed alongside tile arrays of the design proposed in Chapter 5. These were intended to be infused with an epoxy or rubber matrix and tested in a drop tower for the presence of topological interlocking under low energy impacts (compared to high velocity ballistic impacts). This work could be continued and tested similarly to the work described by Mirkhalath [85].

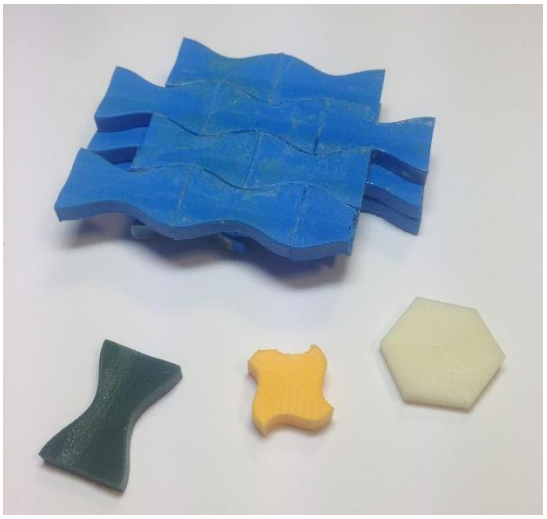

Figure 8-1: Several 3D printed prototypes of tile designs featuring (top) a tile array similar to that proposed in Chapter 5, (lower left) a single tile of the same design, (centre) a "shuriken" based tile with sinusoidal sides and (lower right) a hexagonal "wavy" tile based on work by Knipprath [75].

There are many uses of edge chamfers in the design of tank armours [2]. This has proven to be an effective method of disrupting the destructive effect of shockwave reflections from lateral tile surfaces. Provisional FE simulations featuring tiles with edge chamfers were halted due to excessive hourglassing causing non-physical, heavily mesh dependant ballistic responses with insufficient time for these issues to be overcome. However, LS-DYNA and several other available commercial solvers offer several anti-hourglassing options with their software that, with appropriate fine-tuning, may allow for shapes with severe chamfers to be explored in depth for application to body armours.

Although millimetre scale tiles were explored in this work, there may be some benefit in exploring sub-millimetre micro- and nano-metre scale features. One such feature is the use of nanoasperites, small sacrificial columns of calcified material that bridge the gap between tiles that reinforce the interlocking structure and, when loaded sufficiently, break to absorb further energy.

BIBLIOGRAPHY

[1] Hallam D 2015 *Understanding the Deformation of Ceramic Materials at High Strain Rates* (University of Surrey)

[2] James B 2006 Practical Issues in Ceramic Armour Design *Progress in Ceramic Armor* (The American Ceramic Society) pp 23–34

[3] Wen Y, Xu C, Wang S and Batra R C 2015 Analysis of behind the armor ballistic trauma *J. Mech. Behav. Biomed. Mater.* **45** 11–21

[4] Ji B and Gao H 2004 Mechanical properties of nanostructure of biological materials *J. Mech. Phys. Solids* **52** 1963–90

[5] Wang C, Huang Y, Zan Q, Guo H and Cai S 2000 Biomimetic structure design — a possible approach to change the brittleness of ceramics in nature *Mater. Sci. Eng. C* **11** 9–12

[6] Oaki Y, Kotachi a., Miura T and Imai H 2006 Bridged Nanocrystals in Biominerals and Their Biomimetics: Classical Yet Modern Crystal Growth on the Nanoscale *Adv. Funct. Mater.* **16** 1633–9

[7] Katti K S and Katti D R 2006 Why is nacre so tough and strong? *Mater. Sci. Eng. C* **26** 1317–24

[8] Richter B I, Kellner S, Menzel H, Behrens P, Denkena B, Ostermeier S and Hurschler C 2011 Mechanical characterization of nacre as an ideal-model for innovative new endoprosthesis materials. *Arch. Orthop. Trauma Surg.* **131** 191–6

[9] Flores-Johnson E a., Shen L, Guiamatsia I and Nguyen G D 2014 Numerical investigation of the impact behaviour of bioinspired nacre-like aluminium composite plates *Compos. Sci. Technol.* **96** 13–22

[10] Laible R C and Barron E 1980 *History of Armour, Ballistic Materials and Penetration Mechanics* ed R . Laible (New York, NY: Elsevier)

[11] Crouch I G 2016 *The Science of Armour Materials* (Woodhead Publishing)

[12] Ortiz C and Boyce M C 2008 Bioinspired Structural Materials 1053–4

[13] Munch E, Launey M E, Alsem D H, Saiz E, Tomsia a P and Ritchie R O 2008 Tough, bio-inspired hybrid materials. *Science* **322** 1516–20

[14] Meyers M a, Chen P-Y, Lopez M I, Seki Y and Lin A Y M 2011 Biological materials: a materials science approach. *J. Mech. Behav. Biomed. Mater.* **4** 626–57

[15] Bertram J E A and Gosline J M 1986 Fracture toughness design in horse hoof keratin *J. Exp. Biol.* **125** 29–47

[16] Fleck N A, Deshpande V S and Ashby M F 2010 Micro-architecture materials: past, present and future *Proc. R. Soc. A* **466** 2495–516

[17] Mayer G 2011 New toughening concepts for ceramic composites from rigid natural materials. *J. Mech. Behav. Biomed. Mater.* **4** 670–81

[18] Ma Z-D, Wang H, Cui Y, Rose D, Socks A and Ostberg D 2006 *Designing An Innovative*

Composite Armor System For Affordable Ballistic Protection (Ann Arbor)

[19] Skaggs S R 2003 A Brief History of Ceramic Armor Development *Ceram. Eng. Sci. Proc.* **24** 337–49

[20] Gooch Jr. W A 2011 Overview of the Development of Ceramic Armour *Advances in Ceramic Armour VII* (Wiley) pp 195–213

[21] Ong C W, Boey C W, Hixson R S and Sinibaldi J O 2011 Advanced layered personnel armor *Int. J. Impact Eng.* **38** 369–83

[22] Cronin D S, Bui K, Kaufmann C, Mcintosh G and Berstad T 2003 Implementation and Validation of the Johnson-Holmquist Ceramic Material Model in LS-Dyna *4th Euopean LS-DYNA Users Conference* pp 47–60

[23] Mukasey M B, Sedgwick J L and Hagy D W 2008 NIJ Standard-0101.06: Ballistic Resistance of Body Armor

[24] Hazell P J, Roberson C J and Moutinho M 2008 The design of mosaic armour: The influence of tile size on ballistic performance *Mater. Des.* **29** 1497–503

[25] Shockey D, Marchand A H, Skaggs S R, Cort G E, Burkett M W and Parker R 1990 Failure phenomenology of confined ceramic targets and impacting rods *Int. J. Impact Eng.* **9** 263–75

[26] Anon http://www.coorstek.com/resource-library/8510-1364_ceramic_properties_mp.pdf

[27] Crouch I G, Appleby-Thomas G and Hazell P J 2015 A study of the penetration behaviour of mild-steel-cored ammunition against boron carbide ceramic armours *Int. J. Impact Eng.* **80** 203–11

[28] Liu W, Chen Z, Cheng X, Wang Y, Amankwa A R and Xu J 2016 Design and ballistic penetration of the ceramic composite armor *Compos. Part B Eng.* **84** 33–40

[29] Woodward R L, O'Donnel R G, Baxter B J, Nicol B and Pattie S D 1989 Energy absorption in the failure of ceramic composite armours *Mater. Forum*

[30] Hallam D, Heaton A, James B, Smith P and Yeomans J 2015 The correlation of indentation behaviour with ballistic performance for spark plasma sintered armour ceramics *J. Eur. Ceram. Soc.* **35** 2243–52

[31] David N V., Gao X-L and Zheng J Q 2009 Ballistic Resistant Body Armor: Contemporary and Prospective Materials and Related Protection Mechanisms *Appl. Mech. Rev.* **62** 050802

[32] Rozenberg Z and Yeshurun Y 1988 The Relation Between Ballistic Efficiency and Compressive Strength of Ceramic Tiles *Int. J. Impact Eng.* **7** 357–62

[33] Lundberg P and Lundberg B 2005 Transition between interface defeat and penetration for tungsten projectiles and four silicon carbide materials *Int. J. Impact Eng.* **31** 781–92

[34] Gooch Jr. W A 2006 An overview of ceramic armor applications *Progress in Ceramic Armor* (The American Ceramic Society) pp 3–21

[35] Compton B G, Gamble E A and Zok F W 2013 Failure initiation during impact of metal spheres onto ceramic targets *Int. Impact Eng.* **55** 11–23

[36] Jung W-K, Lee H-S, Jung J-W, Ahn S-H, Lee W-I, Kim H-J and Kwon J-W 2007 Penetration mechanisms of ceramic composite armor made of alumina-GFRP *Int. J. Precis. Eng. Manuf.*

[37] Evans A G and Wilshaw T R 1976 Quasi-static solid particle damage in brittle solids-I. Observations analysis and implications *Acta Metall.* **24** 939–56

[38] LaSalvia J, Normandia M J, Millller H T and Mackenzie D E 2005 Sphere impact induced damage in ceramics: I. Armor-grade SiC and TiB2 *Advances in Ceramic Armor: 29th International Conference on Advanced Ceramics and Composites*

[39] LaSalvia J, McCuiston R C, Fanchini G, Mackenzie D E, McCauley J W, Chhowalla M and Miller H T 2007 Shear Localization in a Sphere-Impacted Armor Grade Boron Carbide *Proc. of the 23 rd Int. Symposium on Ballistics.*

[40] Roesler F C 1956 Brittle fractures near equilibruim *Proc. Phys. Soc. Sect. B* **69** 981–92

[41] Savio S G, Senthil P, Singh V, Ghoshal P, Madhu V and Gogia A 2015 An experimental study on the projectile defeat mechanism of hard steel projectile against boron carbide tiles *Int. J. Impact Eng.*

[42] Wilkins M L 1978 Mechanics of penetration and perforation *Int. J. Eng. Sci.* **16** 793–807

[43] McCauley J W, Crowson A, Gooch W A, Rajendran A M, Bless S J, Logan K, Normandia M and Wax S 2012 *Ceramic armour materials by design* (John Wiley & Sons)

[44] Sherman D 2000 Impact failure mechanisms in alumina tiles on finite thickness support and the effect of confinement *Int. J. Impact Eng.* **24** 313–28

[45] Davis R N, Neely a. M and Jones S E 2004 Mass loss and blunting during high-speed penetration *Proc. Inst. Mech. Eng. Part C J. Mech. Eng. Sci.* **218** 1053–62

[46] Flinders M, Ray D, Anderson A and Cutler R A 2005 High-toughness silicon carbide as armor *J. Am. Ceram. Soc.* **88** 2217–26

[47] McCuiston R, LaSalvia J, McCauley J and Mayo W 2008 The possible roles of stochiometry, mictrostructure, and defects on the mechanical behaviour of boron carbide *Advances in Ceramic Armour IV* (Wiley) pp 153–62

[48] Chen M, McCauley J W and Hemker K J 2003 Shock-Induced Localized Amorphization in Boron Carbide *Science (80-.).* **299** 1563–6

[49] Anderson Jr C and Royal-Timmons S 1997 BALLISTIC PERFORMANCE OF CONFINED 99.5%-A1203 CERAMIC TILES *Int. J. Eng.* **19** 703–13

[50] Heard H C and Cline C F 1980 Mechanical behaviour of polycrystalline BeO, Al2O3 and AlN at high pressure *J. Mater. Sci.* **15** 1889–97

[51] Lankford J 2005 The Role of Dynamic Material Properties in the Performance of Ceramic Armor *Int. J. Appl. Ceram. Technol.* **1** 205–10

[52] Lundberg P 2004 *Interface Defeat and Penetration: Two Modes of Interaction between Metallic Projectiles and Ceramic Targets* (Uppsala University)

[53] Field J E 1999 ELSI conference: Invited lecture liquid impact: Theory, experiment, applications *Wear* **233–235** 1–12

[54] Tate A 1969 Further results in the theory of long rod penetration *J. Mech. Phys. Solids* **17** 141–50

[55] Forrestal M J, Børvik T and Warren T L 2010 Perforation of 7075-T651 Aluminum Armor Plates with 7.62 mm APM2 Bullets *Exp. Mech.* **50** 1245–51

[56] Bass C R, Salzar R S, Lucas S R, Donnellan L, Folk B and Corporation A 2006 Injury Risk in Behind Armor Blunt Thoracic Trauma **12** 429–42

[57] López-Puente J, Arias a., Zaera R and Navarro C 2005 The effect of the thickness of the adhesive layer on the ballistic limit of ceramic/metal armours. An experimental and numerical study *Int. J. Impact Eng.* **32** 321–36

[58] Trogé A, O'Leary R L, Hayward G, Pethrick R a and Mullholland A J 2010 Properties of photocured epoxy resin materials for application in piezoelectric ultrasonic transducer matching layers. *J. Acoust. Soc. Am.* **128** 2704–14

[59] Crouch I G 2014 Effects of cladding ceramic and its influence on ballistic performance *International Symposium on Ballistics*

[60] Ben-Dor G, Dubinsky A and Elperin T 2018 Optimization of ballistic properties of layered ceramic armor with a ductile back plate *Mech. Based Des. Struct. Mach.* **46** 18–22

[61] Ben-Dor G, Dubinsky A and Elperin T 2014 Analytical engineering models of high speed normal impact by hard projectiles on metal shields *Cent. Eur. J. Eng.* **3** 349–73

[62] Mahdi S and Gillespie J W 2004 Finite element analysis of tile-reinforced composite structural armor subjected to bending loads *Compos. Part B Eng.* **35** 57–71

[63] Johnson G R and Holmquist T J 1994 An improved computational constitutive model for brittle materials *American Institute of Physics* p 309

[64] Mcintosh G 1998 The Johnson-Holmquist Ceramic Model as used in LS-DYNA2D

[65] Gupta N K, Iqbal M A and Sekhon G S 2006 Effect of projectile nose shape, impact velocity and target thickness on deformation behavior of aluminum plates *Int. J. Solids Struct.*

[66] Krishnan K, Sockalingam S, Bansal S and Rajan S D 2010 Numerical simulation of ceramic composite armor subjected to ballistic impact *Compos. Part B Eng.* **41** 583–93

[67] Rahbek D B, Simons J W, Johnsen B B, Kobayashi T and Shockey D A 2017 Effect of composite covering on ballistic fracture damage development in ceramic plates *Int. J. Impact Eng.* **99** 58–68

[68] Barthelat F, Tang H, Zavattieri P, Li C and Espinosa H 2007 On the mechanics of mother-of-pearl: A key feature in the material hierarchical structure *J. Mech. Phys. Solids* **55** 306–37

[69] Signetti S and Pugno N M 2014 Evidence of optimal interfaces in bio-inspired ceramic-composite panels for superior ballistic protection *J. Eur. Ceram. Soc.* **34** 2823–31

[70] Barthelat F 2010 Nacre from mollusk shells: a model for high-performance structural materials. *Bioinspir. Biomim.* **5** 035001

[71] Fratzl P, Kolednik O, Fischer F D and Dean M N 2015 The mechanics of tessellations – bioinspired strategies for fracture resistance *Chem. Soc. Rev.*

[72] Salinas C and Kisailus D 2013 Fracture mitigation strategies in gastropod shells *Jom* **65**

473–80

[73] Barber A H, Lu D, Pugno N M and Barber A H 2015 Extreme strength observed in limpet teeth 0–5

[74] Bouville F, Maire E, Meille S, Moortèle B Van De and Stevenson A J 2014 Strong, tough and stiff bioinspired ceramics from brittle constituents *Nat. Mater.* 1–7

[75] Knipprath C, Bond I P and Trask R S 2012 Biologically inspired crack delocalization in a high strain-rate environment *J. R. Soc. Interface* **9** 665–76

[76] Wei H, Ma N, Shi F, Wang Z, Zhang X, December R V, Re V, Recei M and February V 2007 Artificial Nacre by Alternating Preparation of Layer-by-Layer Polymer Films and CaCO 3 Strata 1974–8

[77] Zhang Y, Yao H, Ortiz C, Xu J and Dao M 2012 Bio-inspired interfacial strengthening strategy through geometrically interlocking designs. *J. Mech. Behav. Biomed. Mater.* **15** 70–7

[78] Norris C J, Meadway G J, O'Sullivan M J, Bond I P and Trask R S 2011 Self-Healing Fibre Reinforced Composites via a Bioinspired Vasculature *Adv. Funct. Mater.* **21** 3624–33

[79] Rossiter J, Yap B and Conn A 2012 Biomimetic chromatophores for camouflage and soft active surfaces *Bioinspiration and Biomimetics* **7**

[80] Djumas L, Simon G P, Estrin Y and Molotnikov A 2017 Deformation mechanics of non-planar topologically interlocked assemblies with structural hierarchy and varying geometry *Sci. Rep.* **7** 1–11

[81] Brandt K, Wolff M F H, Salikov V, Heinrich S and Schneider G a 2013 A novel method for a multi-level hierarchical composite with brick-and-mortar structure. *Sci. Rep.* **3** 2322

[82] Barthelat F and Espinosa H D 2007 An Experimental Investigation of Deformation and Fracture of Nacre–Mother of Pearl *Exp. Mech.* **47** 311–24

[83] Mayer G 2006 New classes of tough composite materials—Lessons from natural rigid biological systems *Mater. Sci. Eng. C* **26** 1261–8

[84] Knipprath C and Trask R S 2011 *Biologically Inspired Next Generation Outer Body Armour (BINGO)*

[85] Mirkhalaf M, Sunesara A, Ashrafi B and Barthelat F 2018 Toughness by segmentation: Fabrication, testing and micromechanics of architectured ceramic panels for impact applications *Int. J. Solids Struct.* **0** 1–14

[86] Siegmund T, Barthelat F, Cipra R, Habtour E and Riddick J 2016 Manufacture and Mechanics of Topologically Interlocked Material Assemblies *Appl. Mech. Rev.* **68** 040803

[87] Autruffe A, Pelloux F, Brugger C, Duval P, Bréchet Y and Fivel M 2007 Indentation behaviour of interlocked structures made of ice: Influence of the friction coefficient *Adv. Eng. Mater.* **9** 664–6

[88] Ashby M 2011 Hybrid materials to expand the boundaries of material-property space *J. Am. Ceram. Soc.* **94**

[89] Dyskin A V., Pasternak E and Estrin Y 2012 Mortarless structures based on topological interlocking *Front. Struct. Civ. Eng.* **6** 188–97

[90] Kaufmann C, Cronin D, Worswick M, Pageau G and Beth A 2003 Influence of material properties on the ballistic performance of ceramics for personal body armour *Shock Vib.* **10** 51–8

[91] Feli S and Asgari M R 2011 Finite element simulation of ceramic/composite armor under ballistic impact *Compos. Part B Eng.* **42** 771–80

[92] Mitra E, Hazell P J and Ashraf M 2015 A discrete element model to predict the pressure-density relationship of blocky and angular ceramic particles under uniaxial compression *J. Mater. Sci.*

[93] Harris A J, Vaughan B, Yeomans J A, Smith P A and Burnage S T 2014 Surface preparation of alumina for improved adhesive bond strength in armour applications *Advanced Ceramics and Composites*

[94] Zhitnyuk S V., Makarov N a. and Guseva T V. 2014 New Silicon Carbide Based Ceramic Armor Materials *Glas. Ceram.* **71** 6–9

[95] LSTC 2013 *LS-DYNA Keyword User's Manual Volume I*

[96] Lundberg P, Renstrom R and Lundberg B 2000 Impact of metallic projectiles on ceramic targets: transition between interface defeat and penetration *Int. J. Impact Eng.* **24** 259–75

[97] Dean J, Dunleavy C S, Brown P M and Clyne T W 2009 Energy absorption during projectile perforation of thin steel plates and the kinetic energy of ejected fragments *Int. J. Impact Eng.* **36** 1250–8

[98] Dwivedi A, Bradley J and Casem D 2012 Mechanical Response of Polycarbonate with Strength Model Fits

[99] Anon 2013 LS-DYNA Aerospace Working Group Modeling Guidelines Document Version 13-1

[100] Richmond O, Spitzig W A and Sober R J 1976 The effect of hydrostatic pressure on the deformation behavior of maraging and HY-80 steels and its implications for plasticity theory *Metall. Trans. A* **7** 1703–10

[101] Gama B a. and Gillespie J W 2011 Finite element modeling of impact, damage evolution and penetration of thick-section composites *Int. J. Impact Eng.* **38** 181–97

[102] Kılıç N and Ekici B 2013 Ballistic resistance of high hardness armor steels against 7 . 62mm armor piercing ammunition Ballistic resistance of high hardness armor steels against 7 . 62 mm armor piercing ammunition

[103] Moynihan, Thomas J.; Chou, Shun-Chin; Mihalcin A L 2000 Application of depth-of-penetration test methodology to characterize ceramics for personnel protection 31

[104] Kenner V H 1977 The propagation of compressive and tensile waves in a fluid column *Int. J. Mech. Sci.* **20** 373–83

[105] Lundberg P, Westerling L and Lundberg B 1996 Influence of scale on the penetraton of tungsten rods into steel-backed alumina targets *Int. J. Impact Eng.* **18** 403–16

[106] Nicholas T and Rajendran A M 1992 Mechanical behaviour at high strain rates *Comput. Mech. Assoc.* 140

[107] Weiss A, Vizel A and Durban D 2013 An experimental investigation of deep penetration

into polycarbonate targets *27th International Symposium on Ballistics* pp 1241–51

[108] Tonge A L and Ramesh K T 2016 Multi-scale defect interactions in high-rate brittle material failure. Part I: Model formulation and application to ALON *J. Mech. Phys. Solids* **86** 117–49

[109] National V and Promulgated S 1981 Technology Assessment Program NIJ Standard for Ballistic Helmets National Institute of Justice

[110] Rashid T, Aleem M A, Akbar S, Rauf A and Shuaib M 2016 Numerical simulation of armor capability of AI2O3 and SiC armor tiles *IOP Conf. Ser. Mater. Sci. Eng.* **146**

[111] Bless S J and Jurick D L 1998 Design for Multi-Hit Capability *Int. J. Impact Eng.* **21** 905–8

[112] Rahbek D B and Johnsen B B 2015 *Dynamic behaviour of ceramic armour systems*

[113] Lin A Y-M, Chen P-Y and Meyers M A 2008 The growth of nacre in the abalone shell. *Acta Biomater.* **4** 131–8

[114] Bertoldi K, Bigoni D and Drugan W J 2008 Nacre: An orthotropic and bimodular elastic material *Compos. Sci. Technol.* **68** 1363–75

[115] Trask R 2013 *Modelling and Simulation of Topological Interlocking, Hierarchical Architecture and Functional Grading Nature Materials for Improved Armour*

[116] Dashkovskiy S, Suhr B, Tushtev K and Grathwohl G 2007 Nacre properties in the elastic range: Influence of matrix incompressibility *Comput. Mater. Sci.* **41** 96–106

[117] Tang H, Barthelat F and Espinosa H 2007 An elasto-viscoplastic interface model for investigating the constitutive behavior of nacre *J. Mech. Phys. Solids* **55** 1410–38

[118] Stempflé P and Brendlé M 2006 Tribological behaviour of nacre—Influence of the environment on the elementary wear processes *Tribol. Int.* **39** 1485–96

[119] Tushtev K, Murck M and Grathwohl G 2008 On the nature of the stiffness of nacre *Mater. Sci. Eng. C* **28** 1164–72

[120] Graf T, Hauge A and Andrade F 2013 Adhesive modelling with LS-DYNA: Recent developments and future work *LS-Dyna Forum*

[121] Jiang W-G, Hallett S R, Green B G and Wisnom M R 2007 A concise interface constitutive law for analysis of delamination and splitting in composite materials and its application to scaled notched tensile specimens *Int. J. Numer. Methods Eng.* **69** 1982–95

[122] Harper P W and Hallett S R 2008 Cohesive zone length in numerical simulations of composite delamination *Eng. Fract. Mech.* **75** 4774–92

[123] Gordon J E 1978 *Structures (or why things don't fall down)* (Penguin Science)

[124] Harris A J J, Vaughan B, Yeomans J A, Smith P A and Burnage S T 2013 Surface preparation of silicon carbide for improved adhesive bond strength in armour applications *J. Eur. Ceram. Soc.* **33** 2925–34

[125] Narducci F and Pinho S T 2018 Interaction between nacre-like CFRP mesolayers and long-fibre interlayers *Compos. Struct.* **200** 921–8

[126] Chintapalli R K, Breton S, Dastjerdi A K and Barthelat F 2014 Strain rate hardening: A hidden but critical mechanism for biological composites? *Acta Biomater.* **10** 5064–73

[127] Tipler P A and Mosca G 2008 *Physics For Scientists And Engineers* ed C Marshall (New York: W. H. Freeman and Company)

[128] Grujicic M, Pandurangan B and Coutris N 2012 A Computational Investigation of the Multi-Hit Ballistic-Protection Performance of Laminated Transparent-armor Systems *J. Mater. Eng. an* **21** 837–48

[129] Madhu V, Ramanjaneyulu K, Balakrishna Bhat T and Gupta N K 2005 An experimental study of penetration resistance of ceramic armour subjected to projectile impact *Int. J. Impact Eng.* **32** 337–50

[130] Bürger D, Rocha de Faria A, de Almeida S F M, de Melo F C L and Donadon M V. 2012 Ballistic impact simulation of an armour-piercing projectile on hybrid ceramic/fiber reinforced composite armours *Int. J. Impact Eng.* **43** 63–77